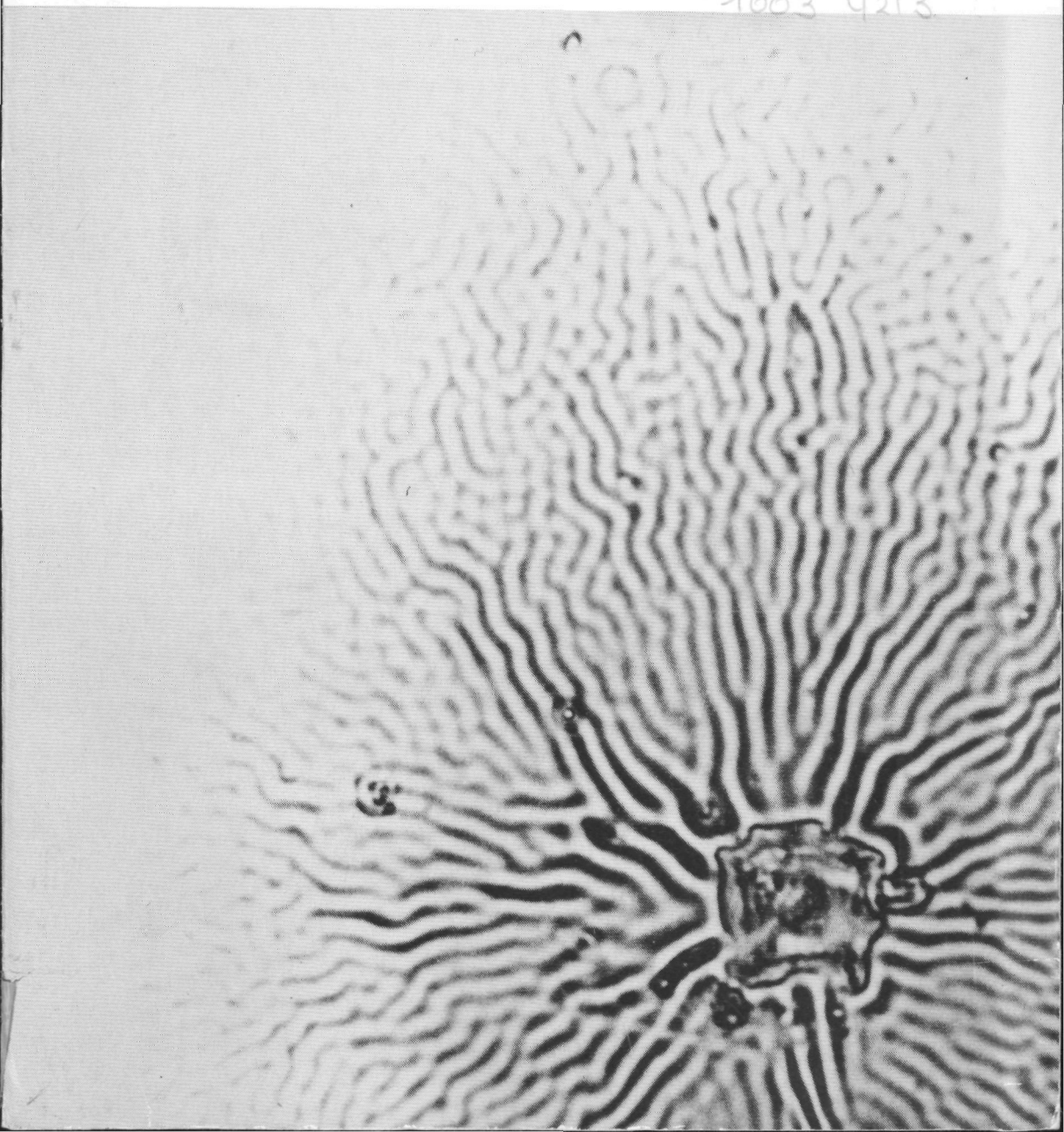


SOME PROPERTIES OF PHOTOTHERMOPLASTIC RECORDING MATERIALS

Andrianto Handoyo

1603 4213



SOME PROPERTIES OF
PHOTOTHERMOPLASTIC RECORDING MATERIALS



C10045
32089

P1603
4213

BIBLIOTHEEK TU Delft

P 1603 4213



C

453208

SOME PROPERTIES OF PHOTOTHERMOPLASTIC RECORDING MATERIALS

**Proefschrift ter verkrijging van
de graad van doctor in de
technische wetenschappen
aan de Technische Hogeschool Delft,
op gezag van de rector magnificus
prof. dr. ir. F. J. Kievits,
voor een commissie aangewezen
door het college van dekanen
te verdedigen op
woensdag 12 december 1979
te 14.00 uur door**

Andrianto Handoyo

**natuurkundig ingenieur
geboren te Malang, Indonesië**



Dit proefschrift is goedgekeurd door
de promotor: Prof. Dr. Ir. H. J. Frankena

ERRATA

p. 20, 4th line from below : ... to be employed ...

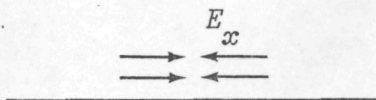
p. 31, 16th line from below : ... because the electric potential ...

p. 46, 7th line from above : $\text{sinc}(d/\lambda_y) = \sin(\pi d/\lambda_y) / (\pi d/\lambda_y)$

p. 48, 11th line from above : $\lambda_y \rightarrow \infty$

13th line from above : $\lambda_x = 2\pi/k_x$

p. 56, Fig. 3.11



p. 105, 7th line from above : ... and according to our ...

p. 112, 5th line from below : ... with a length of 8 cm ...

p. 127, Eq. (5.1)

$$: V_0 = (V_s - V_s') \left(\frac{R_{hp}}{R_{hp} + R_a} - \frac{R_b}{R_b + R_c} \right)$$

p. 159, Fig. 6.23

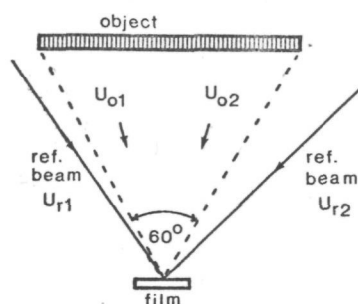
: the combination of these photographs has been mounted upside down. The upper photograph should be inverted and becomes Fig. 6.23.b; similarly, the lower photograph must be turned upside down to become Fig. 6.23.a.

p. 160, 5th line from above : $|U_0|^2 \cdot U_r^* U_0$

Fig. 6.24

: the whole drawing under Fig. 6.24.a has been shifted horizontally. The point p_1 should be located under the bright point seen approximately in the centre of Fig. 6.24.a.

p. 165, Fig. 6.31



p. 172, Eq. (B-1)

$$: \times \cos kx_m \} = -A_{1m} \sinh kh.$$

CONTENTS

I.	INTRODUCTION	1
II.	PHOTOTHERMOPLASTIC FILM AND RECORDING PROCESS	5
II.1.	Film construction	5
	II.1.1. <i>The substrate</i>	6
	II.1.2. <i>The conductive layer</i>	7
	II.1.3. <i>The photoconductive layer</i>	8
	II.1.4. <i>The thermoplastic layer</i>	9
II.2.	The recording process	11
	II.2.1. <i>The charging stage</i>	11
	II.2.2. <i>The exposure</i>	12
	II.2.3. <i>The development</i>	14
	II.2.4. <i>Readout, reusability, frost deformation, and bandpass response</i>	15
II.3.	Several variations of the film construction	19
	II.3.1. <i>Film for electron beam recording</i>	19
	II.3.2. <i>Film with a single photoconductive-thermoplastic layer</i>	20
	II.3.3. <i>Reflective film</i>	22
	II.3.4. <i>Other variations in the film construction</i>	24
II.4.	Several variations of the charging system	26
	II.4.1. <i>The use of a grid</i>	27
	II.4.2. <i>Parallel plane charging</i>	27
II.5.	Several variations of the recording process	29
	II.5.1. <i>The sequential method</i>	30
	II.5.2. <i>The simultaneous method</i>	31
	II.5.3. <i>The SLA and PLA methods</i>	32
III.	FACTORS THAT INFLUENCE THE PERFORMANCE OF PHOTOTHERMOPLASTIC FILMS	37
III.1.	Charging stage	37
	III.1.1. <i>The effects of the surface potential</i>	37
	III.1.2. <i>Factors that determine the surface potential</i>	38
	III.1.3. <i>Potential distribution</i>	42

III.2.	The exposure	43
III.2.1.	<i>The intensity pattern within the photoconductive layer</i>	43
III.2.2.	<i>A model for the relation between the absorbed intensity and the potential in the photoconductive layer</i>	48
III.2.3.	<i>Potential distribution</i>	53
III.3.	Recharging	57
III.4.	Development	60
III.5.	Readout	64
III.5.1.	<i>Diffraction efficiency</i>	64
III.5.2.	<i>Signal-to-noise ratio</i>	65
III.5.3.	<i>Nonlinearity</i>	66
III.5.3.1.	<i>Nonlinearity of the recording process</i>	66
III.5.3.2.	<i>Intrinsic nonlinearity of a phase material</i>	67
III.5.3.3.	<i>Effects of the nonlinearity</i>	67
III.5.4.	<i>Some measurements of the signal-to-noise ratio and the linearity</i>	70
III.6.	Reusability	76
III.6.1.	<i>Fatigue of the thermoplastic material</i>	76
III.6.2.	<i>Residual image</i>	77
III.6.3.	<i>Contamination of the thermoplastic surface</i>	78
III.7.	The role of the thermoplastic thickness	80
IV.	QUASISTATIC THEORY OF FROST DEFORMATION IN THERMOPLASTIC FILMS	85
IV.1.	Introduction	85
IV.2.	Theory	87
IV.2.1.	<i>Equilibrium condition</i>	87
IV.2.2.	<i>Surface tension</i>	89
IV.2.3.	<i>The pressure due to the electric field</i>	90
IV.3.	Potential distributions	91
IV.3.1.	<i>Equipotential model</i>	93
IV.3.2.	<i>Nonequipotential model</i>	94
IV.4.	Relation between λ and a	96
IV.4.1.	<i>Equipotential model</i>	96
IV.4.2.	<i>Nonequipotential model</i>	98

IV.5.	Discussion	102
	IV.5.1. <i>The frost wavelength and the optimal wavelength in thermoplastic recordings</i>	102
	IV.5.2. <i>On the phase separation phenomenon</i>	103
V.	A CAMERA SYSTEM FOR THE RECORDING PROCESS	107
V.1.	The camera	108
	V.1.1. <i>Film transport mechanism</i>	108
	V.1.2. <i>High-voltage distributor</i>	111
	V.1.3. <i>The heat plate</i>	112
	V.1.4. <i>The charger unit</i>	113
V.2.	The shutter	117
V.3.	The high-voltage supply	118
V.4.	The electronic control	119
	V.4.1. <i>Time duration</i>	119
	V.4.2. <i>Transport instructions</i>	120
	V.4.3. <i>Execution of a few recording modes</i>	121
	V.4.4. <i>Temperature control</i>	122
VI.	SOME EXPERIMENTS WITH THE FILM AND THE CAMERA SYSTEM	131
VI.1.	The effects of the development time	131
	VI.1.1. <i>Development energy</i>	131
	VI.1.2. <i>Development temperature</i>	133
	VI.1.3. <i>Diffraction efficiency</i>	134
VI.2.	Recording method with two heating stages	135
	VI.2.1. <i>The principle</i>	135
	VI.2.2. <i>Leakage current measurements</i>	136
	VI.2.3. <i>The results from the method</i>	139
VI.3.	Spatial wavelength of frost deformation	142
	VI.3.1. <i>Optical arrangements for the measurements</i>	142
	VI.3.2. <i>Moiré pattern</i>	147
	VI.3.3. <i>Measurement results</i>	151
VI.4.	On the band-pass response of the film	155
VI.5.	Taking holograms from an extended object with the band-limited film	162
APPENDIX A:	CONCISE DERIVATION OF THE POTENTIAL DISTRIBUTION IN THE FILM AFTER THE EXPOSURE	169

APPENDIX B: DETERMINATION OF THE NUMBER OF SUBAREAS M IN THE DERIVATION OF THE POTENTIAL DISTRIBUTION	172
REFERENCES	173
CONCISE LIST OF SYMBOLS	178
SUMMARY	181
SAMENVATTING	183
LEVENSBERICHT	187

I. INTRODUCTION

Usually, an optical recording medium requires a certain process to transform the recorded information into a form that is suitable for readout. For instance, the process needed for silver halide materials consists mainly of chemical development and fixation. In some applications, the need exists to perform such a process inside the recording configuration, within a time that should be as short as possible. Three examples of these applications are mentioned here:

1. *Optical memories*¹: these are systems for information storage in which very fast information retrieval from any part of the recording can occur. In case of updating, removal from the set-up and slowness of the recording process can be unwanted.
2. *Optical information processing*: this includes various optical methods e.g. for restoring blurred images², for signal detection by complex spatial filtering³, or for other applications based on the mathematical operations of optical information⁴.
3. *Holographic interferometry*⁵: a method in which microscopic deformations, translations or vibrations of an object can be investigated and measured without mechanical contacts.

In the two first-mentioned applications, the requirement of a fast process is more severe than in the third; this in relation with the feasibility investigated in many laboratories to construct computers partially having light as the information carrier⁶. The "optical computing" is attractive due to its potentials of parallel processing of large data sets, acting very rapidly.

The conventional silver halide emulsions are less appropriate for this purpose, since the development and fixation processes as a rule require at least a few minutes. These wet chemical processes, which usually can not be accomplished in the recording set-up, still have another serious disadvantage. The film position in the set-up after development is often so critical, that

accurate repositioning (often within parts of the optical wavelength) of the film in its original state, if possible, always requires much troublesome labour.

In the past two decades, this limited potentiality of conventional photographic materials has brought many investigators to explore the possibilities of new types of materials. These researches have involved the media mentioned in Table I.1 (for comparison, unbleached silver halide material is also listed).

Table I.1. Some typical properties of several recording media⁷⁻⁹

	Diffraction efficiency (%)	Exposure energy (mJ/cm ²)	Spatial frequency (lp/mm)	Erase- and reusability
Silver-halide materials	5	10 ⁻⁴	500...10000	no
Photopolymers	85	10	200 - 1500 (bandpass)	no
Electro-optic materials	60	10 ³	1000	yes
Photo- thermoplastics	15	10 ⁻¹	400 - 1000 (bandpass)	yes
Photochromic materials	1	10 ² - 10 ³	1000...10000	yes
Magneto-optic materials	0.01	10 - 10 ²	1500	yes

In this table, the mentioned diffraction efficiency (defined as the intensity ratio between the 1st order reconstructed beam and the reconstruction beam of a sine grating) is the maximal obtainable value. The exposure energy is the value needed to achieve this maximal diffraction efficiency. The spatial frequency is the highest value below which the medium can be used.

It is seen that photothermoplastic materials offer certain advantages above the others. The photothermoplastics have the combination of the following properties:

1. A considerable low value of the required exposure energy
2. A rather high diffraction efficiency

3. The recorded information (if desired) can be erased, after which the material is reusable for the next recording.

Experiments with a thermoplastic film for information storage have been performed¹⁰ as early as 1959. Nevertheless, the investigations to develop this material into a useful medium for the aforementioned applications have still not come to an end. Various efforts are going on to acquire a broader view over all its properties, a lot of which have not been clearly understood.

In this context, a study is presented in this thesis concerning the characteristics of photothermoplastic films. The emphasis is placed upon the properties which are related to the holographic applications of the film.

We remark that various names have been given to these films, such as thermoplastic devices, photoplastics, photothermoplastic films, and photoconductor-thermoplastic materials. We use the name thermoplastic film in general, including the case when no light sensitive layer exists within the film, and photothermoplastic film if such a layer (a photoconductor) is present.

To obtain a general view of the material's behaviour, this study commences (in Chapter II) with descriptions of the film construction and the required recording stages. Subsequently, the descriptions are extended in Chapter III by considerations on some parameters that influence the performance of the material. In Chapter IV a theory, formulated for a special type of deformation in thermoplastic films, is developed (another version of this theory has been previously published¹¹).

To enable us to carry out the experiments with the available film we have built a camera system for accomplishing the recording process and the related handling steps (such as the film transport). The principles, various units involved and some of the performances of this system are described in Chapter V.

Finally, in Chapter VI, we present some experiments which are performed with our film and the camera system.

II. PHOTOTHERMOPLASTIC FILM AND RECORDING PROCESS

II.1. Film construction

Photothermoplastic film is an optical recording material that consists of several layers, each having its own function in the process of storing optical information (see Fig. 2.1).

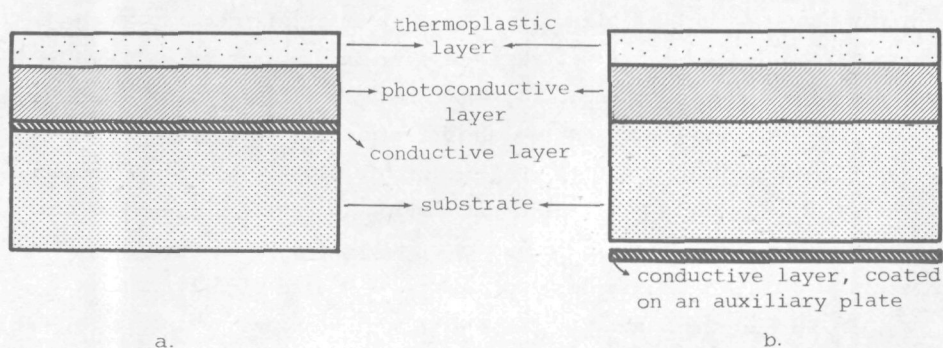


Fig. 2.1. Cross-sections of photothermoplastic film: a. The type commonly considered in literature; b. The type used in our experiments.

Basically, during recording and readout we can distinguish the following stages. First, the film is charged, causing an electric field within it. The photoconductive sheet is, with regard to its conductivity, sensitive to incident light such that illumination can induce a charge transfer through it. Hence, by exposing the film to the light distribution which is to be recorded, the photoconductive layer will locally conduct according to the incident light intensity and thus modify the electric field. After this, the thermoplastic layer is softened, e.g. by heating up, such that the electric field can deform it, resulting in a thickness variation. Since the field is related to the incident light distribution, the information is stored in the form of this thickness variation. Finally, the film can be illuminated by a readout light beam. The

phase of this beam will be changed according to the thickness variation of the film, which in turn corresponds to the recorded information. Thus, the information can be retrieved from the phase variation in this beam.

If desired, the thermoplastic sheet can afterwards be softened again. In the absence of the electric field, the surface tension of the thermoplastic material will equalize the thickness of this layer. The stored information is thus erased, and the film can be utilized again for the next recording.

Apart from several variations in the film construction encountered in literature, these processes are realized with configurations as depicted in Fig. 2.1. In the following account we shall consider each of the layers, their sizes, and some requirements imposed by the film usage.

II.1.1. The substrate

The substrate can be a glass plate or a plastic foil usually having a thickness of about 2 mm or 50 μm , respectively. It is meant to support the layers needed for the light recording processes. If a glass plate substrate is used, it also provides sufficient mechanical rigidity, which is a common requirement in holography. A film with a flexible plastic substrate, however, often needs an additional rigid plate upon which it can rest during recording and readout. Such a plate can be a permanent component of the handling system¹², such as in the system used in our experiments (see also Fig. 2.1.b).

With regard to the available films with a glass plate as substrate, the total area of the film useful for information recording varies^{13,14} from $1 \times 1 \text{ cm}^2$ to about $5 \times 5 \text{ cm}^2$. However, for application in optical memories, a large frame area can be divided into many subframes which can record information separately; the size of such a subframe can be as small as¹⁵ $1 \times 1 \text{ cm}^2$. On the other hand, some of the films with a flexible substrate have the form of a long wound film. For instance, Lee *et al.*¹⁶ have developed a photothermoplastic material with a width of 12.5 mm and operated with the aid of a modified magnetic tape recording mechanism. Another example is the film we used in our experiments, which has a width of 35 mm and is delivered¹⁷ in a roll containing 30 m long material.

If the film is used for transmission holography, the substrate needs to be transparent and of appropriate optical quality, comparable to the backing glass plate of a silver halide holographic plate. On the other hand, there are techniques in which the exposure and the readout are performed from the thermoplastic side of the film, while the readout signal is obtained from reflection

on the thermoplastic surface¹⁸ or on the conductive layer¹⁹. In these cases, the transparency requirement of the substrate can be dropped.

For development (i.e. softening) of the film, several methods are at our disposal: heating as well as chemical methods. If film heating is used, and if a fast but accurate readout is a necessity, e.g. for real-time measurements in holographic interferometry, it may be required that the substrate has a very low thermal expansion coefficient. For this purpose, ceramic material can be used for the substrate²⁰.

II.1.2. The conductive layer

Upon the substrate (of the film type shown in Fig. 2.1.a), or upon the additional glass plate (Fig. 2.1.b), an electrically conductive material, e.g.^{13,16,21,22} Au, NiCr, AuCr, InO, or ZnO, is vacuum coated or sputtered.

It functions as the ground electrode in the charging system, and in most cases also as an electric resistor by which the film can be heated if an electric current passes through it. For this resistive heating, the surface resistance of the layer should have a value between 10 and 100 ohm²³ (here, surface resistance is defined as the electric resistance per unit area of the layer, measured between two opposite sides of this unit area). Values in this range are favourable, since for a given development time, a higher resistance (to be obtained with a thinner layer) would need a power source with an impractically high voltage, especially if the film area is large. On the other hand, a very low resistance means a thick conductive material, reducing the film transparency considerably, which is disadvantageous in transmission holography.

Gold and tin oxide are among the materials which can nicely satisfy these considerations. For a thin coating, hence a high transparency, their surface resistance is relatively low. In fact, 70-80 ohm is about the maximal surface resistance of a gold layer above which the sheet is too thin to be stable (due to its tendency to form microscopic, unconnected islands). Examples of applicable values are a thickness of about 10 nm, producing a surface resistance of a little less than 10 ohm and an intensity transmission factor for light of 50-60% for the gold coating¹⁶, or a ZnO sheet with a surface resistance of 12 ohm, yielding an intensity transmission factor of about 77%²². For comparison, a NiCr layer has 10-100 Kohm surface resistance and 70-80% transmission factor¹⁶.

The coatings with a high surface resistance (e.g. 10 Kohm) are still useful

if the conductive material is only intended for the ground electrode in the charging system, because the electric resistance encountered by the charging current is mainly due to the thermoplastic and photoconductive layers, so that the voltage drop in the conductive coating is relatively unimportant. For instance, the specific resistivity of Staybelite Ester 10 thermoplastic material lies in the order of 10^{15} ohm-cm at its development temperature²⁴.

II.1.3. *The photoconductive layer*

Upon the conductive layer (Fig. 2.1.a) or upon the substrate (Fig. 2.1.b), a photoconductive material is deposited. Its purpose is to transform the light distribution to be recorded into a conductivity variation, which in its turn leads to an electric field variation.

A general requirement of this layer is a low dark decay, i.e. the resistivity of a charged but unexposed material should be sufficiently high to prevent a considerable decrease in the electric field and to prevent a random charge distribution buildup at the thermoplastic-photoconductive interface, both of which are disadvantageous if some time delay exists between charging and exposure. Furthermore, the softening of the thermoplastic sheet during the development should not also soften the photoconductive material; this to prevent the undesirable dispersing of the layers.

One of the most widely used materials, among other things due to its panchromatic spectral sensitivity and low scattering noise²⁵, is an organic photoconductor, poly-n-vinylcarbazole (PVK), sensitized with 2,4,7-trinitro-9-fluorenone (TNF). Schaffert²⁶ has investigated this material extensively. The molar ratio of PVK and TNF in the mixture determines several properties of this material, e.g. the mobility of the charge carriers²⁷. In fact, the photosensitivity of the photoconductor is a function of the mole fraction of TNF, reaching its maximum value²⁶ at a mole ratio of 1:1 for negative charging and 1:0.8 (PVK:TNF) for positive charging. (A common method used to define the photosensitivity is to consider the exposure energy needed to reduce the potential difference across the material to one half its initial value). This sensitivity is also dependent of the electric field strength. Its value for a photoconductor with a mole ratio PVK:TNF 8:1, initially charged to achieve a field strength of 1.1×10^8 V/m, is equal²¹ to $5 \mu\text{J}/\text{cm}^2$.

Another usable photoconductive compound is PVK sensitized with Brilliant Green dye, which yields a maximal response in red light²⁸, while a composition of PVK and 2,4,5,7-tetranitrofluorenone can be applied for exposures in the

near infra-red²⁹.

The thickness of the photoconductive layer uses to be about 2 μm . This value lies approximately midway between the values resulting from two competing considerations. On one hand, a thick photoconductor of, say, several tens of a μm would be desirable in view of the then attainable photosensitivity, resulting from the greater part of the incident light that will be absorbed by such a thick material. Moreover, as we shall see in Sec. III.2, during exposure, a thick photoconductive layer generates a higher modulation in the electric potential distribution on the film surface than a thin sheet will do. On the other hand, a thick absorbing photoconductor will seriously reduce the film transparency, while it also appears²³ that the thickness of this layer has a contribution in limiting the high spatial frequency response of the film.

The photoconductive layer can be coated by first dissolving the compound in an appropriate solvent; for PVK-TNF it is e.g. tetrahydrofuran. Then the film substrate, (already provided with the conductive layer, if it is the type shown in Fig. 2.1.a) is dipped in this solution and subsequently pulled out at a uniform speed between 8×10^{-4} and 42×10^{-4} m/s (5-25 cm/min). The thickness of the coating is determined by this speed and also by the density, viscosity, surface tension and vapour pressure of the solution²³. After this dip and pull-out process the layer must be dried in a contamination-free environment.

II.1.4. The thermoplastic layer

With a similar technique a thermoplastic material is coated upon the photoconductive layer. This material is meant to be deformed under the influence of the electric field if it is brought into a softened state. In almost all cases the softening of the thermoplastic layer is achieved by heating it to a development temperature θ_d that lies around the glass transition temperature θ_g of the material. The glass transition temperature is an inherent property of amorphous thermoplastic polymers (which have been universally used for photo-thermoplastic films). It is actually in the centre of a certain temperature range within which the material undergoes the transition from a glass-like substance (rigid and often brittle) to a rubber-like one (soft and flexible). Various methods are useful to determine this glass transition temperature, e.g. detecting a change in the slope of the specific volume curve (or its reciprocal, density) vs. temperature³⁰.

Usually, the material used for the layer has a θ_g between 55°C and 90°C. It should be well above room temperature to prevent rapid degradation of the

recorded deformation. However, a not too high θ_g is desirable, in view of the time and the energy needed to heat the film during development or erasing.

Many investigators employed Staybelite Ester 10, a derivative of a natural resin³¹, which can be softened^{32, 33} at $\theta_d = 55^\circ\text{C}$ and dissolved e.g. in naphta, hexane or petroleum ether. Some other materials already used for photothermoplastic recording include polystyrene plasticized with butyl benzyl phtalate ($\theta_d \approx 70^\circ\text{C}$)³⁴, Piccopale H-2 ($\theta_d \approx 90^\circ\text{C}$)²⁸ and styrene-octyl-decyl-methacrylate ($\theta_d \approx 70^\circ\text{C}$)³⁵.

If the film is to be utilized repeatedly, attention must be paid to the possible degradation of the thermoplastic material after many successive record-erase cycles. The degradation, which can be observed as a decrease in both the diffraction efficiency and the signal-to-noise ratio, is caused by the heating cycles, and ion bombardment as well as ozone attack during the charging stages. Two types of deterioration mechanism can be distinguished²³. The first one is cross linking of polymer chains which tends to increase θ_g and the viscosity; the second one is scission of polymer chains, which lowers θ_g and the viscosity of the material.

Several possibilities have been investigated to improve the reusability of the film. One of these involves thermoplastic materials having an appropriate composition, in which those two deterioration types to some degree can compensate each other. For instance, in styrene-methacrylate copolymers, the cross-linking characteristics of the styrene compete with the scission tendencies of the methacrylates. Among many varieties of this material, Anderson *et al.*³⁶ have obtained very good results from octyl-decyl methacrylates.

Reich *et al.*³⁷ have reported that the noise level in a photothermoplastic hologram depends on the composition of the used polymer. In particular, multi-component polymers, e.g. plasticized polymers or polydispersed polymers, tend to produce a high level of noise during readout. In order to obtain a hologram with a high signal-to-noise ratio, they have used polystyrene with a sharply defined molecular weight distribution for the monocomponent thermoplastic layer; indeed, the noise level thus obtained was considerably lower than that from holograms with multicomponent material under the same conditions. The possible mechanism of this phenomenon will be discussed in Chapter IV.

The thickness of the thermoplastic layer has a value about $0.5 \mu\text{m}$. The thickness of this layer determines various properties of the film, such as the value of the spatial wavelength where the film has a maximal response. We shall consider this again in Chapter III.

II.2. The recording process

Several variations have been reported in literature concerning the technique of registering optical information with photothermoplastic films. In this section we consider one of these methods, viz. one which is suitable for our film. This method consists of successive stages of charging, exposure and development. Some other versions of the recording processes will be contemplated in Sec. II.5.

II.2.1. The charging stage

With the conductive layer connected to ground, the film is charged such that the surface of the thermoplastic layer acquires a fairly homogeneous potential, and hence an approximately homogeneous surface charge density, see Fig. 2.2.

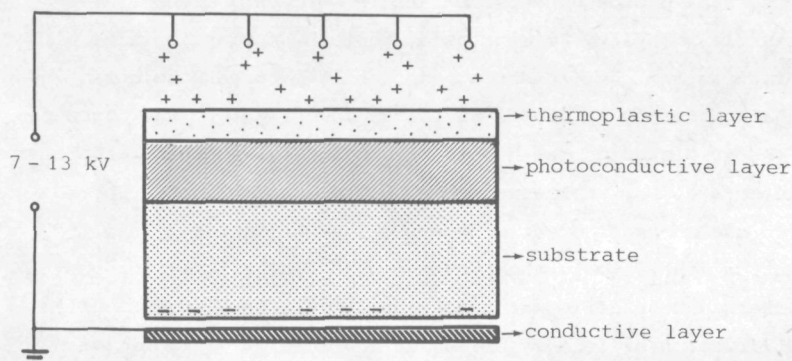


Fig. 2.2. The charging stage.

The charging process can be carried out with a corona device, which is held stationary facing the thermoplastic surface, or moved with a uniform speed parallel to it. In both cases, the distance to the film uses to be in the range 0.5 - 1 cm. This distance is determined by various factors such as the geometry of the corona electrode, the voltage given to it (usually between 7 and 13 kV) and the uniformity requirements of the charge distribution deposited at the film surface. For an example¹⁴, if only a single needle point is used to yield a substantially uniform charge distribution on a 4 cm² film area, the distance between the point and the film surface may not be less than 3 cm, so that the charges released by the electrode can cover that area without a noticeable selective charge accumulation in the central part. In its turn, this relatively

large distance requires a high value (15 kV) for the potential difference to be capable of producing a useful corona discharge.

The term "useful corona discharge" is related to the general practice, that to achieve the maximal response in the information recording, the photo-thermoplastic film is charged until the electric field within it approaches the breakdown field strength of the layers (in the order of hundreds of volts per μm). This is because the conductivity of the photoconductor depends, apart from its relation to the intensity of incident light, also on the field strength. Moreover, the deforming forces during the development are exercised by the electric field in the thermoplastic material, such that a strong electric field will cause a larger deformation. However, a film charged to a high potential, and thus capable of producing the maximal response, is also susceptible to frost deformation (to be described later in this section), which forms a noise source during readout.

Although in Fig. 2.2 the thermoplastic surface is charged with a positive voltage given to the corona electrode, a negative charging is in principle also applicable. However, some photoconductive materials work only appropriately with a certain electric polarity. For instance, photothermoplastic films with PVK - Brilliant Green as the photoconductor can hardly produce a hologram when charged with a negative corona^{2,8}. According to the investigator, the cause can be attributed to charge migration (with selective polarity) at the thermoplastic photoconductive interface. For another example, Saito *et al.*^{3,8} have reported that in relation to the charges injected from the conductive layer into the PVK-TNF photoconductor (the film is the type shown in Fig. 2.1.a), the positive and the negative charges have different injection depths, such that the film yields a higher diffraction efficiency if the corona polarity is positive.

II.2.2. The exposure

After the charging stage, the film is exposed to the light distribution which is to be recorded, see Fig. 2.3, e.g. in holography the interference pattern between the reference and the object beams.

Then, the electric conductivity of the photoconductive sheet will change according to the intensity of the fraction of the incident light that is absorbed by this layer. Actually, this conductivity change takes the form of the release of free charge carriers (holes, electrons) by the photoconductive molecules which are excited by the absorbed photon. These charge carriers are then able to make the material conductive, because they will move in the direction of the electric field lines. Their mobility in PVK-TNF appears to be

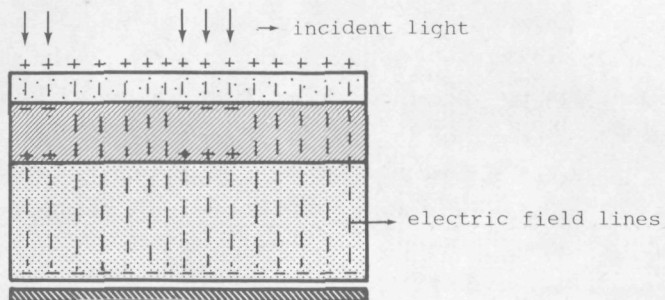


Fig. 2.3. The charged film is exposed to the light distribution to be recorded.

dependent of the electric field strength²⁷.

At places with a high light intensity, many negative charges will move toward the thermoplastic material and accumulate at the thermoplastic-photoconductive interface (the charge carriers can not penetrate the insulating thermoplastic material). Since now these charges become close to the positive charges deposited on the thermoplastic surface, the electric potential at this surface decreases locally. If we neglect a possible leakage current, the charge density at this surface can be assumed to be unaltered, so that the field strength normal to the surface within the thermoplastic layer (being proportional to the surface charge density) remains homogeneous in first approximation. (In Chapter III, we shall see from the solution of Laplace's equation that this field strength has a small variation along the surface).

On the other hand, we now obtain an electric field in the tangential direction between parts of the thermoplastic surface that have different potentials. The field lines are pointing from parts with a higher potential, hence which had a low exposure intensity, to places where the incident light intensity was high.

In the film type used in our experiments (Fig. 2.1.b), the positive charges in the photoconductor, which were released by photoexcitation in pair with negative charges, accumulate at the interface with the insulating substrate, while in the type shown in Fig. 2.1.a these positive charges recombine with electrons from the conductive layer. In both cases, the field strength within the photoconductor, at parts that have been exposed to a high light intensity, is reduced to a low value, making the material locally less sensitive to exposure. This saturating effect determines the maximal useful

exposure range of the film.

It should be noted that for the PVK-TNF photoconductor, which is widely employed in photothermoplastic films, the charge carriers are not range limited^{2,6}. This means that the number of negative charges arriving at the photoconductive - thermoplastic interface (or positive charges arriving at the opposite photoconductive interface) is equal to the number released by photo-excitation within the layer, because PVK-TNF material has no traps which can seize part of the charge carriers on their trip between the point of excitation and the interface.

II.2.3. The development

Next, in the development stage, the thermoplastic material is brought into its soft state to enable the existing electric forces to deform it.

Generally, this softening process is performed by heating the film to the development temperature θ_d ; but the use of a gas that can soften the thermoplastic material chemically is also possible. In this latter case, there will be no problem of thermal deformation of the substrate; the development time, however, tends to be considerable longer than in the heating method.

The heating development can be accomplished in various ways, such as by passing a direct or alternating current through the conductive layer, by capacitively coupling an RF field to the conductive coating so that the RF current flowing through it will heat the film^{1,3}, by bringing a hot plate to about 0.1 mm distance to the thermoplastic surface^{2,8}, or by focusing an infra-red beam at the material which enables one to develop selectively only a small area of the film, e.g. with 1 mm diameter^{3,9}.

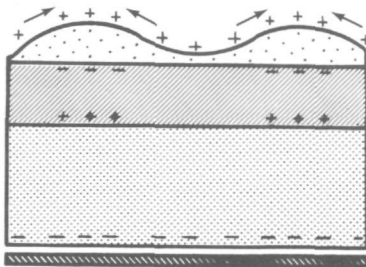


Fig. 2.4. The electric forces deform the softened thermoplastic layer.

Then, the charges at the thermoplastic surface can move along the electric field lines, exerting forces on the softened particles, and in this way deform the thermoplastic layer, see Fig. 2.4. It is primarily the tangential electric field mentioned in Sec. II.2.2 that plays a role in this deforming process. The layer is rippled, and becomes thicker at the parts with a lower electric potential, where the intensity of the incident light has been high.

At the same time, due to the elevated temperature of the film, the conductivity of the thermoplastic material increases. The positive charges at the surface begin to leak through the layer, as also do the negative charges from the photoconductive interface. They will recombine and reduce the electric field strength. The deforming forces are then less strong than at the beginning of the development. The surface tension of the thermoplastic material, on the other hand, tries to make the surface as flat as possible, thus opposing the deforming forces.

If the heat supply at this moment is removed, the temperature drops, the thermoplastic layer is brought back into its rigid state and the deformation is frozen. In this way the film is developed. Without employing wet chemical development and fixation, and without removing the film from its set up, the information is thus recorded as a thickness variation of the thermoplastic layer.

II.2.4. Readout, reusability, frost deformation, and bandpass response

The film is now ready for readout of the recorded information. In holography, the readout occurs by illuminating the film with the reconstruction beam. This light, propagating through the film, undergoes changes in its phase (a phase hologram), which are proportional to the local thickness of the thermoplastic layer. This phase change leads to a higher diffraction efficiency than a comparable amplitude change (produced by an amplitude hologram) would do. Theoretically, for a sinusoidal deformation, whose amplitude is considerably smaller than its spatial wavelength (such that the spatial variation of the incident angle due to the slope variation of the curved surface, is small and produces no significant differences in the reflection factor of that surface), and whose spatial wavelength is considerably longer than the wavelength of the illuminating beam (so that the hologram can be classified as a thin phase hologram⁴⁰), the diffraction efficiency can have a maximal value of 33.9%, while a (thin) amplitude hologram yields a maximal diffraction efficiency of 6.25%.

If the retrieval of the recorded information has been completed, and if it is desired to reuse the material, the thermoplastic layer can be again be softened by heat. Since at the elevated temperature the electric conductivity of the layers increases, the majority of the remaining charges will disappear due to motion, followed by recombination. The surface tension of the softened thermoplastic material can now straighten the corrugated surface, leading to a thermoplastic layer of approximately homogeneous thickness. In this manner the information, recorded as a thickness variation, is erased, whereafter the film is again usable. This erase and reuse possibility is one of the advantages offered by photothermoplastic films. (As we have seen in Sec. II.1.4 and shall consider again in Chapter III, however, some problems may limit the useful number of the record-erase-reuse cycles).

Besides the deformation described above, which reflects the recorded information, another type of deformation can be encountered if the material is directly softened after the charging stage, without the exposure in between. This particular deformation can be described as follows.

The homogeneous charge density at the thermoplastic surface lowers the value of the surface tension, because these charges, being of the same sign, repel each other, reducing the mechanical attraction among surface particles. If the charge density is sufficiently high, the surface tension will vanish, or will even acquire a negative sign. A positive surface tension always tries to make the surface of a material as small as possible. A negative value of this tension means an instability, the surface parts will be pushed apart. Microscopic noiselike irregularities at the surface, e.g. scratches, dust, tiny variations of the layer thickness etc. will grow in amplitude under the influence of such a negative tension.

The surface corrugation resulting from this is called frost deformation. (Another mechanism for the frost formation has been suggested by Reich *et al.*³⁷; this will be discussed in Chapter IV). The frost deformation shows a quasi random bubble pattern, see Fig. 2.5. The distance between two adjacent peaks of the bubbles tends to a preferred value, i.e. the predominant spatial wavelength.

It has been found empirically that this predominant wavelength shows a certain proportionality with the thickness of the thermoplastic layer, the proportionality factor being somewhere between unity and four. To explain the behaviour of the frost deformation, including its relation with the layer thickness, theoretical approaches have been established by several investigators. Budd⁴¹, e.g., has proposed a theory leading to a factor 2 for

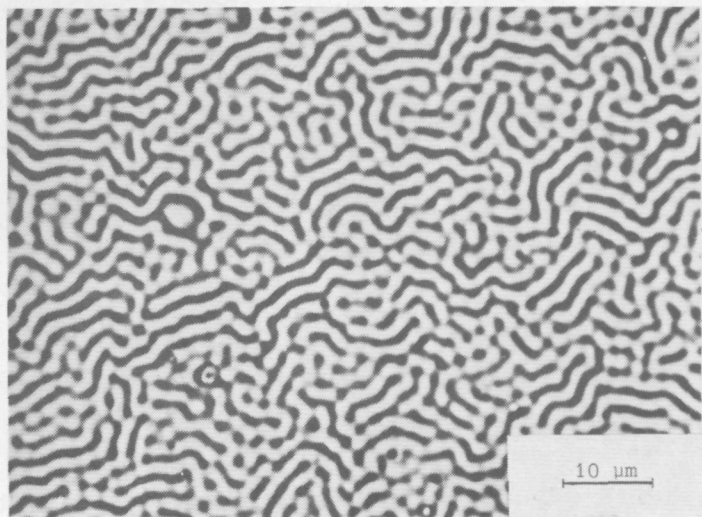


Fig. 2.5. Photomicrograph of frost deformation. The thickness of the thermoplastic layer is $0.5 \mu\text{m}$.

the predominant wavelength-thickness ratio, while Killat²⁴, revising Budd's theory, concluded that this ratio ought to approach the value 4. We propose a different theory for the frost deformation¹¹, which will be presented in detail in Chapter IV.

If a light distribution is recorded on a photothermoplastic film, the resulting deformation will be maximal at a certain value of the spatial wavelength. This optimal value, which has been found to depend on parameters describing the recording method, lies in the vicinity of the predominant wavelength. The amplitude of the thickness variation decreases then as the spatial wavelength goes higher or lower than that optimal value. In this way, a photothermoplastic film has a bandpass response. An example of this bandpass characteristic can be seen in Fig. 2.6, which shows the spatial frequency response of our film. If in recording a hologram a maximal response is required, the mean angle between the reference and the object beams has to be chosen such that it yields the optimal spatial frequency in the interference pattern at the film plane. Moreover, if some vignetting in the readout is to be avoided, the extent of the object must be such that the resulted variation of the spatial frequency of the interference pattern is well within the film's bandwidth.

Generally, the frost deformation, appears upon development of a film that has been charged previously to obtain a high charge density but is still unexposed. It can also be encountered, however, on a film that has been charged

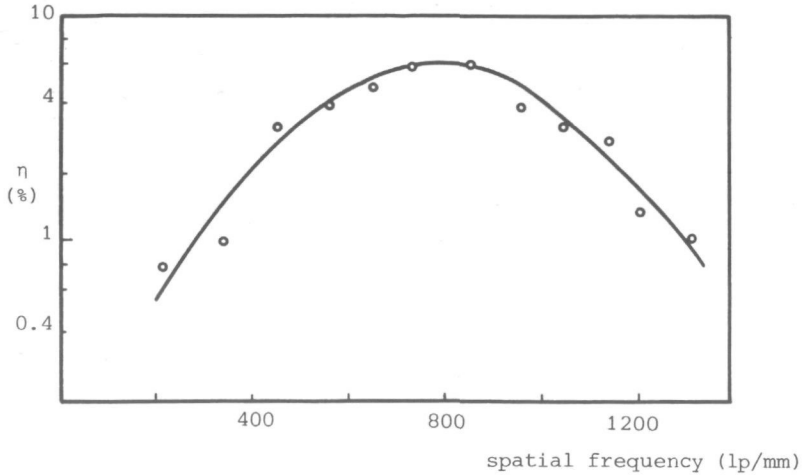


Fig. 2.6. Diffraction efficiency η obtained from our film as a function of the spatial frequency (see Sec. III.5.4 for the recording parameters).

as well as illuminated. Then, two mechanisms can be considered. First, if the film has been exposed to light with a spatially homogeneous intensity, the charges at the thermoplastic surface remain to have a practically smooth distribution, so that the repelling tangential electric forces are still equally distributed in every direction, which is similar to the condition in an unexposed film, resulting in the frost bubbles. The second mechanism refers to small deformations, produced by spatially varying electric forces that are related to the light distribution to be recorded, early in the development stage. These small deformations can become the nuclei of frost bubbles (as are also scratches or dust at the surface). The growth of these frost bubbles in the subsequent stages of development will compete with the formation of the information related deformation. It depends amongst others on the intensity of the light distribution and on the recording method, whether the information related surface corrugation is finally significantly larger than the quasi random frost deformation. However, some traces of frost bubbles are generally still observable in a finished recording, forming a considerable source of noise during readout. Hence, frost deformation is significant for the signal-to-noise ratio in holographic reconstruction from a photothermoplastic film.

II.3. Several variations of the film construction

Since many investigators have prepared their own material, a lot of variations exist in the configuration, size and composition of the films and in the processes for information recording. In this section we shall consider the main varieties of film construction.

II.3.1. Film for electron beam recording

This film, which is actually the predecessor¹⁰ of the photothermoplastic films known today, consists of only a substrate, a conductive sheet and a thermoplastic layer; no photoconductor is included. It is not intended for the direct recording of light distributions, but for a registration in which a scanning electron beam (modulated by the information) is employed.

In the experiments of Glenn¹⁰, the writing process is performed while the film is being transported, the electron beam scanning perpendicularly to the film motion. In this way, a charge pattern is deposited upon the thermoplastic surface (see Fig. 2.7). Several modulation techniques, including beam current, or focus modulation, can be applied to relate this surface charge density to the signal. Subsequently, the thermoplastic material is heated to its development temperature, e.g. by passing the film along a pair electrodes coupling an RF electric field capacitively to the conductive layer. Then, the electrostatic forces between the surface charges and the opposite charges at the conductive sheet will deform the softened thermoplastic layer.

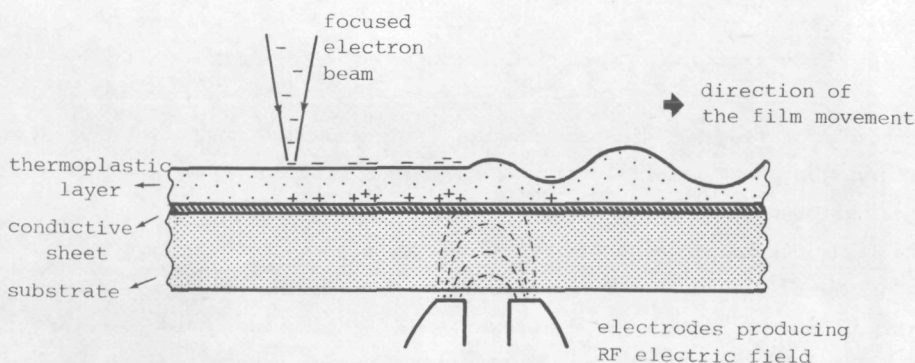


Fig. 2.7. Electron beam recording.

If the film is moved further on and has passed the RF field, it is cooled

below its development temperature and the deformation will be frozen. Then, one obtains a thickness variation, related to the information which has modulated the electron beam. The readout can be accomplished with visible light.

Although on this film information can be recorded with a corona device with a modulated voltage operating in air, the results have proved to be more reproducing and the procedure faster for a recording process using an electron gun in a vacuum environment¹⁰.

The thickness of this film varies^{10,42} from about 5 μm to 25 μm . In spite of its incapability for direct registration of a light distribution, this material forms a promising tool for the coupling between electronic and optical systems, where the signal is to be translated in a form suitable for readout with visible light. For instance, when such a system includes a high-resolution electron optics, it can be suitable for producing computer generated holograms. More than one decade after the first experiments, investigation on applications of this film has been continued⁴²⁻⁴⁸. Part of the research includes display of images from electron microscopes⁴², storage and projection of TV images⁴³, recording a hologram at one place on a vidicon and simultaneously reconstructing it at another place with the thermoplastic film (the signal being electronically transported)⁴⁴, and synthetic aperture radar data processing^{45,46}.

This film has an advantage above the usual photothermoplastic type we have discussed in Sec. II.1. It is the absence of the absorbing photoconductive material which, in transmission readout systems, diminishes the light efficiency. For instance, a 2 μm thick PVK-TNF photoconductor with molar ratio 1:1 absorbed²⁶ 50% of the incident light intensity at 500 nm wavelength, thus reducing the readout efficiency by a factor of two.

II.3.2. Film with a single photoconductive-thermoplastic layer

Instead of having two separate thermoplastic and photoconductive layers, in this film variant both materials are combined in a single medium, see Fig. 2.8. This type has been named photoplastic film by Gaynor and Aftergut⁴⁹.

The layer can be prepared either by synthesis of photoconductive thermoplastic polymers^{49,50} such as by incorporating a photosensitive dye, or by dispersion of photoconductor particles which will inject the charge carriers they generate into the thermoplastic. If a photoconductive particle or dye is to be employed in a thermoplastic polymer, the materials must be chosen such that they are compatible, if degradation due to chemical interaction is to be avoided. An example of a usable composition is plasticized polystyrene as the thermoplastic, with tetracyanoethylene (TCNE)-pyrene as the dye⁵¹, or with very

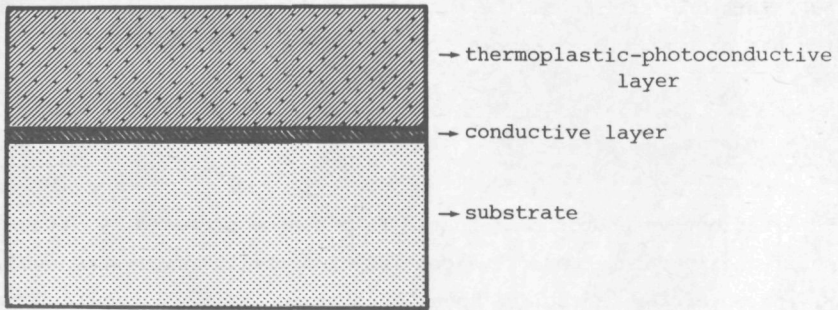


Fig. 2.8. Photoplastic film: the thermoplastic and the photoconductive materials are incorporated in a single layer.

fine copper-doped cadmium sulphide particles (having an average size of tenths of a μm) as the dispersed photoconductor⁵².

In order to prevent undesired influences on some thermoplastic properties, the concentration of the dye or the particles in the polymer should be not too high. An example of impairing effects of impurities in a polymer is the lowering of the material's softening temperature⁵³. In photothermoplastic films this can mean a rapid degradation at room temperature of the acquired deformation.

The permitted low photoconductor concentration (e.g. CdS concentration as low as 1% by weight has been used⁵²) means in turn that the layer must be relatively thick (between⁴⁹⁻⁵² 12 and 75 μm) to be capable of absorbing a fraction of the incident light necessary to yield a not too low recording sensitivity. In Sec. II.2.3, however, we have briefly seen that the spatial frequency for the maximal response is inversely proportional to the thickness of the deformable thermoplastic layer. Hence, the use of films with a thick single layer of photoconductive thermoplastic is mainly confined to recording at low spatial frequencies.

These restrictions tend to make this film construction less attractive for holographic applications than the configuration with separate layers. Ost and Moraw⁵⁴, however, have succeeded to record holograms using the mixed layer type; with a layer thickness of 2 μm a maximal diffraction efficiency of about 29% has been reported, while the exposure energy was in the order of 10 $\mu\text{J}/\text{cm}^2$, comparable to the value of the separate layers type. Unfortunately, the material

composition of the layer has not been specified. The diffraction efficiency of the hologram decreased from 20% to 4% within 20 days (at room temperature, 21°C). This degradation may be caused by the impairing effects in the polymer which has been mentioned before.

II.3.3. Reflective film

A reflective photothermoplastic film can be prepared by either depositing a sufficiently thick conductive coating upon the thermoplastic surface^{18,55}, or applying a thicker conductive layer than is normally used for the ground electrode in the charging system and the heating resistor¹⁹. In both cases, readout is achieved with the readout beam incident from the thermoplastic side of the film and subsequently reflected by the conductive material. With such a reflective film, one can obtain a higher efficiency than in the transmission readout from a conventional photothermoplastic film having the same deformation.

We consider the first type of reflective film (with the coated thermoplastic surface). To record an optical information on this film, exposure can better be performed with light incident from the substrate side of the film, since the reflective coating will not admit light sufficiently. As before, the spatial wavelength of the resulting deformation is supposed to be significantly larger than both its amplitude and the wavelength of the reconstruction wave. Assuming further that the reconstruction beam is practically perpendicular to the film plane, this beam after reflection at the deformed surface will have undergone a spatial phase change, maximally equal to $4\pi\alpha_p/\Lambda_0$, where Λ_0 is the vacuum wavelength of the readout light (the wavelength in air is considered to be equal to this) and α_p the deformation amplitude, see Fig. 2.9.

On the other hand, for the same value α_p , the maximal phase change in the transmission mode is given by $2\pi\alpha_p(n_1 - 1)/\Lambda_0$, where n_1 is the index of refraction of the thermoplastic material.

The diffraction efficiency η , in its turn, is related to the phase variation in the readout beam. For a sinusoidal phase change, obtained from a sinusoidal deformed surface satisfying the aforementioned conditions, η is equal to $J_1^2(\phi)$, where J_1 is the first order Bessel function^{23,56} and ϕ the amplitude of the phase change. Of course, we must take into account the amplitude reflection factor of the conductive coating.

However, to have an impression about the improvement in η , let us assume that the ideal reflection factors of 100% (coated film) and 0% (transmissive film) are attained. Further, let α_p/Λ_0 be less than 0.064, such that the Bessel

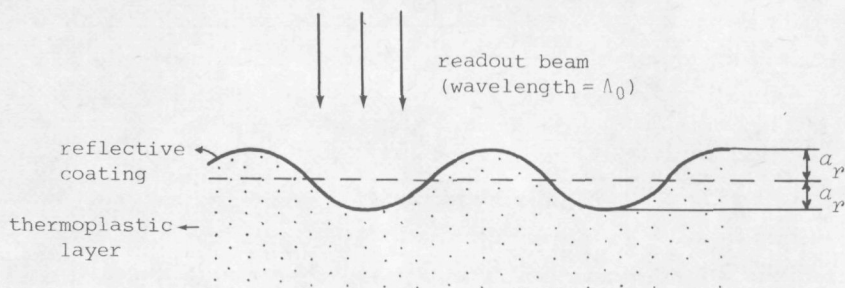


Fig. 2.9. Readout from a deformed film having a reflective coating on its upper surface.

function is approximately in its linear range [i.e. $J_1(\phi) \approx \phi/2$ within an accuracy of 8.5%]. Then, the ratio of diffraction efficiencies between the coated and the transmissive film under these conditions is equal to $\{[4\pi a_p/\lambda_0]/[2\pi a_p(n_1-1)/\lambda_0]\}^2 = 11.1$ if we insert^{19,55} a value of $n_1 = 1.6$.

In reality, the reflection factor can be made fairly high, but never close to 100%. This is because the reflection factor of the coating depends on its thickness, which in turn is limited by the allowed mechanical resistance against the deformation of the thermoplastic layer. With an indium coating, a thickness of more than 100 nm induces a noticeable resistance to deformation⁵⁵. In this respect, a 30 nm thick indium layer is more acceptable, yielding an intensity reflection factor of about 70%.

In such a coated reflective film one may incorporate a highly absorbing photoconductive material, since it will not hamper the reflective readout. The coating can also be utilized to charge the film directly without the use of a corona device. The voltage required is then significantly lower, since no electrical discharge in air needs to be produced; the film is charged simply by connecting the conductive coating upon the thermoplastic layer and the ground electrode to the output of a DC voltage source.

In this charging technique, to assure a continuous electrical conductivity throughout the sheet, the coating on the thermoplastic surface should not be too thin, because a material coated on the deformable layer appears to be extra liable to form an island structure. For an indium coating⁵⁵, the electrical continuity is assured if the thickness is higher than 500 nm (of course, this impairs the deformability of the thermoplastic), while for a gold coating¹⁸ the

value is about 200 nm. Using such a gold layer, holographic recordings have been made by Friesem *et al.*¹⁸, who found that the coated film was more difficult to operate than the usual, corona-charged films. It was more susceptible to electrical breakdown, which was attributed to dust particles under the gold coating.

II.3.4. Other variations in the film construction

Two different variations in the film configuration were suggested by Lee *et al.*⁵⁷, and by Killat and Terrell⁵⁸, respectively, but unlike the versions already discussed in Sections II.3.1 - II.3.3, these variations have not been mentioned by other investigators.

The first variation⁵⁷ is the introduction of an electrically insulating polymer layer between the photoconductive and the thermoplastic layers, see Fig. 2.10. The thickness of this interlayer has not been specified but was very small compared to the thickness of the photoconductor.

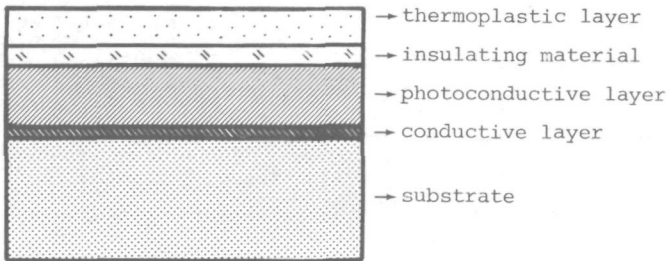


Fig. 2.10. Introduction of an insulating material between the thermoplastic and the photoconductive layers.

Generally, in a charged photothermoplastic film, a slight leakage current flows through the thermoplastic layer; the leaked charges recombine with opposite charges (which exist at the thermoplastic-photoconductive interface after exposure) or flow further through the photoconductor. This charge decay increases considerably when the thermoplastic material is softened during the development stage, due to the significant increase of the conductivity around the glass transition temperature θ_g .

In the modified film shown in Fig. 2.10, the leakage current is reduced by

the large resistance of the insulating interlayer. The greater number of retained charges produce stronger deformation forces during development, resulting in a diffraction efficiency η (9 - 11%) which is higher than that of a film without the insulating layer (6%). Furthermore, when the time interval between exposure and development is extended to 3 minutes, η from this modified film has approximately not diminished, while η from the usual film decreases to about 3.5%.

One of the requirements for the insulating layer is a glass transition temperature θ_g that lies substantially higher than θ_g of the thermoplastic; this to assure that the resistivity of the interlayer is always higher than that of the thermoplastic material (in view of the significant decrease of the resistivity around θ_g). Moreover, a higher θ_g of the interlayer will prevent mixing with the thermoplastic material; such a mixing is especially undesirable if the film is to be reused many times.

Another requirement of the interlayer is related to the small number of leaking charges that would have penetrated the thermoplastic but can not pass through the insulating layer. In the record-erase-reuse application, the gradual accumulation of these charges at the interface of the thermoplastic-insulating layers will influence the recording processes unfavourably. Therefore, they should be eliminated or neutralized after some reuse cycles. Lee *et al.*⁵⁷ have applied for the interlayer a material which is photoconducting at a light wavelength differing from the wavelength for the exposure. Then, the interlayer can be made conductive any time by illuminating the film with appropriate light, such that the trapped charges can flow away. The material used was undoped PVK (poly-n-vinylcarbazole without any sensitizer) which also satisfied the first requirement (a higher θ_g than the thermoplastic material).

The second⁵⁸ variation in the film construction involves two additive layers, i.e. a transparent conductor and a photoconductor with a low resistivity, which are placed between the original photoconductive layer and the substrate, see Fig. 2.11. The extra photoconductor is from Cu-doped cadmium sulphide with a thickness of about 4 μm .

This film is meant for application as an optical memory; it must be capable of recording a large number of tiny holograms independently. In the film usage, the two conductive layers are connected to a low voltage source. Upon illumination with the interference pattern to be recorded, an electric field variation is produced within the "original" photoconductor in the usual way. In the same time, however, the conductivity of the extra photoconductor increases, resulting in a photocurrent that is high enough to soften the

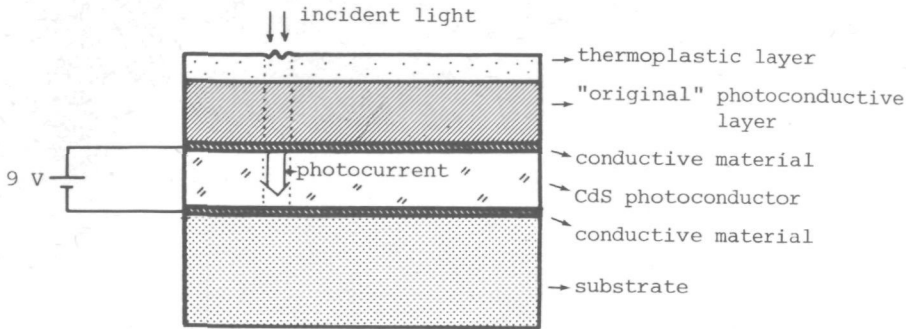


Fig. 2.11. Introduction of a CdS photoconductor and another conductive layer to enable local development to take place.

thermoplastic material locally. The development stage is thus locally combined with the exposure and many holograms can be recorded on this film separately and independently.

Using two converging waves, Killat and Terrell⁵⁸ have succeeded to record holograms with diameter as small as about 10 μm on this film.

II.4. Several variations of the charging system

In general, two problems turn up with the use of a corona device consisting of one or more thin wires or an array of small-radius points. The first is the difficulty to control the value of the acquired surface potential. This potential depends on many factors, such as: the conductivity of the layers in the film, the speed of the charger if it is swept along the film, and the geometry of the corona electrodes. It is desirable to have some control over this surface potential, since a very high potential as well as a very low potential are disadvantageous for the film performance (see Sec. III.1).

The second problem refers to the efforts of generating a potential as homogeneous as possible over the thermoplastic surface. This is because any potential variation will result in variation in the exposure sensitivity (the sensitivity of the photoconductor depends on the electric field strength within it) and variation in the electric forces during deformation, yielding a hologram with an uneven diffraction efficiency over its area.

To overcome these problems, modifications of the charging system have been suggested by several investigators.

II.4.1. The use of a grid

In a set up for optical memories using photothermoplastic film, Stewart *et al.*¹⁵ have placed a grid between the corona wire and the film at a distance of about 25 μm from the surface of the thermoplastic layer (see Fig. 2.12).

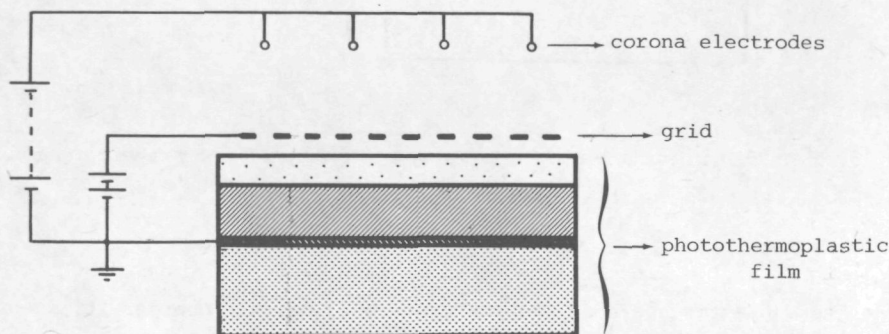


Fig. 2.12. The use of a grid in the charging system.

The grid has the form of a metal plate with apertures of .1 mm square each. The holographic optical memories are situated in film sections facing these apertures. During charging, an electric potential is given to the grid, equal to the desired value of the surface potential. Then, any possible charge excess at the surface will result in a potential higher than the preadjusted value, so that this charge excess will flow to the grid, reducing the surface potential until finally it is approximate equal to the grid potential. Since the surface of the film is thus compelled to obtain a potential not higher than the preadjusted value, this configuration, besides having a limiting effect, also improves the uniformity of the deposited charge distribution.

Using this technique, Stewart *et al.*¹⁵ have attained a reproducible maximal potential at the surface, which was practically independent of the parameters of the corona electrode.

II.4.2. Parallel plane charging

Instead of using wires or points, a transparent conductive material coated on a glass plate can be employed to charge the film through a corona discharge (see Fig. 2.13).

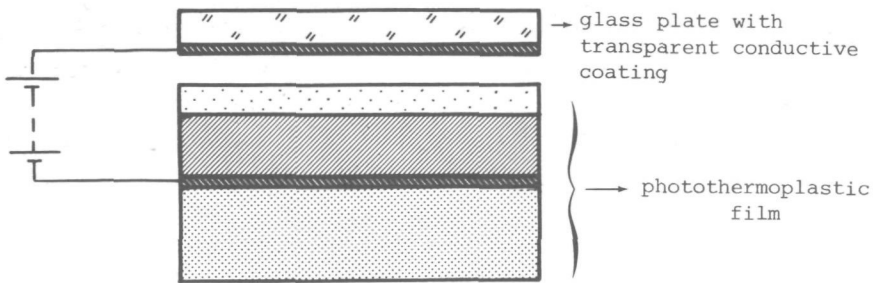


Fig. 2.13. Parallel plane charging: a transparent conductive material coated on a glass plate is employed to charge the film.

Colburn *et al.*^{25,35} have placed such a glass plate at a distance 50 to 150 μm from the thermoplastic surface. The voltage needed on this charger is, due to the close distance, considerably lower than for a wire or point device, i.e. 700 - 900 V instead of 7 - 13 kV (generally, a wire or point corona device should not be operated from too close a distance to the film surface, in order to minimize the influence of the geometry and the size of the small-radius electrode on the distribution of the deposited charges, cf. Sec. II.2.1). This parallel plane charging yields a good uniformity of the surface potential; for a film area of $38 \times 38 \text{ mm}^2$, it produces a surface potential with a less than 5% variation over a central part of $30 \times 30 \text{ mm}^2$.

Moreover, as compared to corona devices that must be swept along the film, the charging process with this system is faster (about 1 ms). Apart from these advantages, some attention has to be paid to several latent problems. For instance, the width of the gap between the coated surface of the glass plate and the thermoplastic surface should be precisely the same over the whole film area. Otherwise, electric breakdown can easily occur at places where this gap is smaller. The gap must also be free of dust, since a breakdown will be stimulated by the presence of dust particles. If such an electric breakdown does occur, the whole film becomes permanently unusable, the breakdown path within the layers will short-circuit the ions, released by the charger, to the ground electrode.

In the record-readout-erase and reuse application, a problem may arise due to the ozone gas generated by the corona discharge within the air gap. Usually, the coated glass plate is permanently fastened to the film to guarantee constant distance between them. The ozone, which is harmful for the thermo-

plastic material, will then accumulate in the gap and will seriously limit the number of the useful record-erase cycles. To solve this problem, Colburn *et al.*^{25,35} have performed the record-erase processes in an argon atmosphere. Then, 5000 record-erase cycles can be achieved, practically without decrease in the diffraction efficiency. It is the ultimate intention of these investigators to seal the gap between the glass plate and the film after filling it with a clean inert gas. Such a construction would assure a dust and ozone free gap and would protect the deformable thermoplastic material from mechanical damage, e.g. caused by handling or transport of the film.

II.5. Several variations of the recording process

The sequence of the recording stages described in Sec. II.2 (charge-expose-develop) can be schematically depicted in Fig. 2.14.

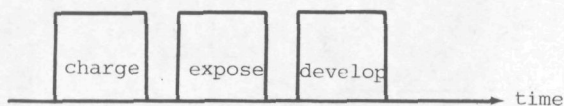


Fig. 2.14. Schematic representation of the charge-expose-develop recording method.

For charging the film, a stationary or a sweeping corona device can be used; in both cases this method is simple to operate. In the case of a sweeping corona device, only one movement of the corona device is entailed. Should the film be charged again after the exposure, such as in the method we shall describe in Sec. II.5.1, then an insufficiently smooth sweep mechanism may cause a minute displacement of the film after exposure, which will degrade the readout in e.g. the real time technique for holographic interferometry.

However, the method shown in Fig. 2.14 generally yields a relatively low diffraction efficiency⁵⁶. The reasons of this will be discussed in Sec. III.3. Now, we shall consider some alternative methods, usable for producing holograms with a higher diffraction efficiency. Note that for reasons which will be described in Chapter III, these methods are not appropriate for the film depicted in Fig. 2.1.b, but, they are useful with the film type shown in Fig. 2.1.a.

II.5.1. The sequential method

In this method, a recharge stage is introduced after exposure, see Fig. 2.15.

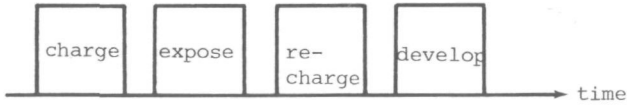


Fig. 2.15. The sequential method.

During the recharge step, the (positive) charges released by the corona device will flow to places with a lower electric potential, i.e. parts of the film where the incident light had a high intensity, compare Fig. 2.3 and Fig. 2.16. Such extra charges raise the electric potential at the parts, which had previously a low value, until the whole surface acquires an approximately uniform potential.

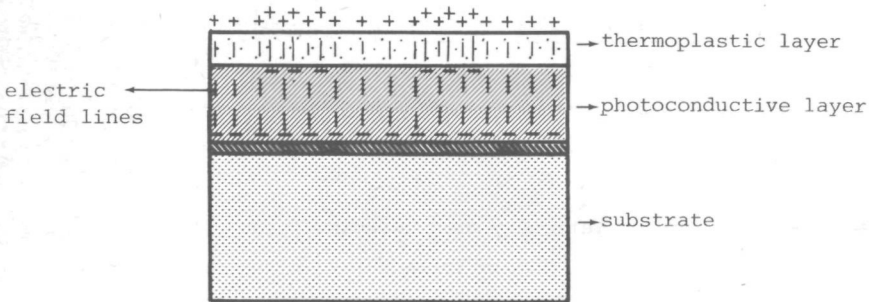


Fig. 2.16. The film after the recharge stage: the surface potential is homogeneous and a spatial variation in the normal electric field is produced within the thermoplastic layer.

The change in the surface charge density now produces a significant spatial variation of the normal electric field component within the thermoplastic layer. A stronger field corresponds to a higher surface charge density, hence to places where the exposure intensity was high. In the development stage, this stronger electric field will make the softened thermoplastic layer locally thinner. The resulting deformation is a reversal of the shape obtained from the charge-expose-develop method described in Sec. II.2, viz., the thermoplastic

layer is now thinner where the intensity was high and thicker where the exposure intensity was low.

II.5.2. The simultaneous method

In this method, the charging, exposure and development stages are started simultaneously, see Fig. 2.17. This technique requires a stationary corona device, working continuously during the recording processes without forming an obstruction to the exposure, e.g. the transparent parallel plane system described in Sec. II.4.2.

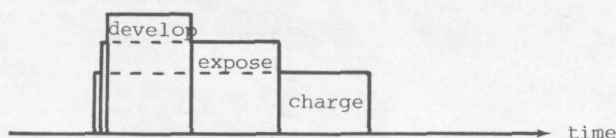


Fig. 2.17. The simultaneous method.

Compared to the sequential method, the simultaneous technique produces a hologram with a higher diffraction efficiency, and with a better signal to noise ratio. The increase in the diffraction efficiency is attributed to the following mechanism. During development, the charges released by the continuously working corona device will mainly flow to those surface parts where the softened thermoplastic layer begins to be thinner, because the electric ~~the~~ ^{erratum} there is decreasing. This potential decrease is caused partly by the closer distance between the positive and the negative charges due to the thinner layer, and partly by the local increase of the conductivity of the photoconductor due to the incident light, allowing more negative charges to accumulate at the thermoplastic-photoconductive interface, see Fig. 2.18.

These extra charges, the positive coming from the corona device and the negative from the photoconductor, enforce the deforming forces, which will further reduce the local thickness of the layer, inducing more charges to arrive at these parts, and so on. This amplifying effect continues after the heat supply for the development is stopped, as long as the thermoplastic material is still sufficiently soft to be deformed.

In this manner one can obtain a surface corrugation with a significantly large amplitude. Credelle and Spong¹³ could even achieve a 40% diffraction efficiency from their holographic grating. This efficiency is higher than the maximal value 33.9% predicted theoretically for a sinusoidal thin phase grating

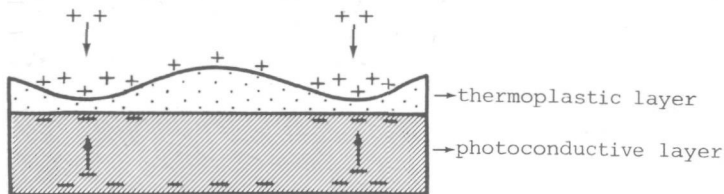


Fig. 2.18. The amplifying effect in the simultaneous method: the light distribution induces charges at the thermoplastic-photoconductive interface; these charges, together with the thinner thermoplastic layer, diminish the potential locally, causing more positive charges to come from the corona device; the stronger electric field makes the layer further thinner and so on.

(examination on the structure of the surface relief of the hologram indeed revealed a profile that was not sinusoidal).

The deforming forces in this technique can be so strong that at the valley of the deformation, the thermoplastic layer is torn, leaving the underlying photoconductor exposed to air. If this effect occurs, the film can not be reused, unless the thermoplastic material is completely removed (dissolved) and then coated again.

In some applications, the simultaneous method can be less suitable than the sequential mode of recording. For example, a film with a flexible substrate can experience some deformation during the heat development due to the thermal expansion of this non-rigid material, especially if it does not rest on an auxiliary rigid plate. Then, with the simultaneous technique, the incident light distribution in a later phase of the development will arrive at places slightly different from that in the beginning of the deformation, thus degrading the contrast of the stored interference pattern. With the sequential method, such a temporary thermal deformation does not offer a problem, because the development is separated from the exposure stage.

II.5.3. The SLA and PLA methods

Saito *et al.*⁵⁹ have proposed two modifications of the simultaneous method by including a homogeneous incoherent illumination (white light from a tungsten lamp was used) in the recording processes, see Fig. 2.19.

In the SLA (simultaneous light application) method, the white-light illumination is applied together with the exposure by the light distribution to

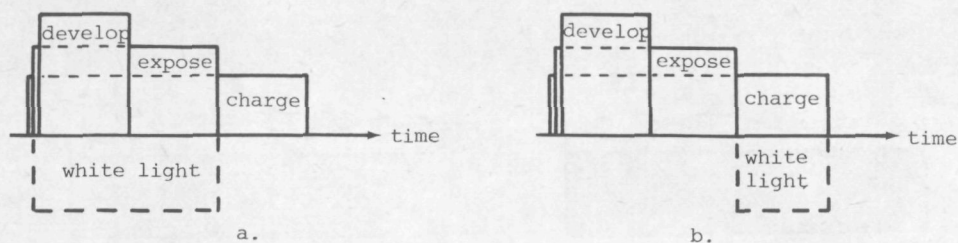


Fig. 2.19. a. The simultaneous light application (SLA) method; b. The post light application (PLA) method.

be recorded. Using this technique, the investigators have reported an improvement in the signal-to-noise ratio and an increase in the film sensitivity. In particular, a diffraction efficiency requiring $400 \mu\text{J}/\text{cm}^2$ in the conventional simultaneous method, took only $200 \mu\text{J}/\text{cm}^2$ with their technique.

This sensitivity increase can be attributed to the extra charges induced by the homogeneous illumination. The "task" of the information related light distribution (to produce charges in the photoconductor) is thus assisted by the white-light illumination, so that the needed exposure energy is reduced. As also has been shown experimentally by the investigators, the intensity of the homogeneous illumination must not be too high; otherwise, the resulting modulation of the total light pattern would be too low to yield a useful film response.

In the PLA (post light application) method, the white light illumination is introduced after the usual exposure is finished, but as long as the charging device is still working. As in the simultaneous method, the charging stage can be adjusted to continue as long as the thermoplastic material is still fairly soft. Then, during this cooling period an amplifying effect occurs just as described in Sec. II.5.2. Now, however, many more charges are presumably available at the thermoplastic-photoconductive interface (being not confined by the light distribution to be recorded), so that the deformation can be expected to be still larger than in the simultaneous method, see Fig. 2.20.

Besides a higher sensitivity and a considerable improvement in the signal-to noise ratio, the investigators have indeed reported a higher deffraction efficiency in this PLA method, and also an improvement in the reciprocity between the intensity and the exposure time (i.e., the multiplication of the exposure intensity and the exposure time, for a given exposure energy, is constant throughout a broader range of exposure times than in the simultaneous

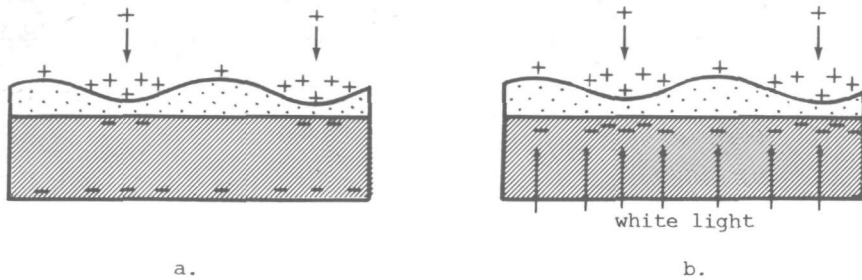


Fig. 2.20. The amplifying effect in the PLA method (b) is compared to that of the simultaneous method (a).

method).

This reciprocity improvement may be attributed to the amplifying effect as well, because if the amplitude at the onset of the deformation is small (due to a reciprocity failure), the amplifying effect will further enlarge the height of the surface relief until the mechanical conditions (surface tension, electric forces, viscosity) finally terminate the growth of the relief, these mechanical conditions being independent of the fact whether the reciprocity is fulfilled or not.

To summarize, we present in Table II.1 some reported results that have been obtained using the recording methods already considered. Note that these results can not simply be compared to each other (except the data mutually from Credelle and Spong¹³, from Colburn and Tompkins³⁵, and from Saito *et al.*⁵⁹, respectively) because they were obtained with different films having different characteristics.

Table II.1. Diffraction efficiencies achieved with the recording methods already described

Method	Diffraction efficiency (%)	Investigator/Comment
Charge-expose-develop	8.5	obtained with our film
	0.1 - 0.5	Colburn and Tompkins ³⁵ , as they reported: "a few tenths of a percent"
	2	Lo <i>et al.</i> ⁶⁰
Sequential	22	Credelle and Spong ¹³
	30	Bergen ²⁸
	13	Lin and Beauchamp ²²
Simultaneous	1	Colburn and Tompkins ³⁵
	40	Credelle and Spong ¹³
	18	Saito <i>et al.</i> ⁵⁹
SLA	16	Saito <i>et al.</i> ⁵⁹
PLA	25	Saito <i>et al.</i> ⁵⁹

III. FACTORS THAT INFLUENCE THE PERFORMANCE OF PHOTOTHERMOPLASTIC FILMS

In this chapter we consider some factors influencing the film performance; most of these factors are specifically related to one of the recording-readout stages used for our film.

III.1. Charging stage

III.1.1. The effects of the surface potential

Corona discharge has been universally employed to deposit charges upon the surface of photothermoplastic films. The deposited charges give rise to a surface potential, the value of which determines the following factors:

1. *Diffraction efficiency*: a higher surface potential ϕ_s yields a higher diffraction efficiency η . Firstly because (for a given exposure energy) the higher potential difference across the photoconductor induces a larger modulation in the electric field at the thermoplastic surface (which produces the deforming forces), see Sections III.2 and III.3. Secondly, because the amplitude of this electric field is also larger due to the higher ϕ_s . Apart from other factors considered later in this Section, ϕ_s is proportional to the voltage ϕ_c given to the corona electrode; in Fig. 3.1 one can see the relation between η and ϕ_c of our film.

2. *Frost deformation*: this deformation is induced by the change in the surface tension of the thermoplastic material due to the deposited charges. Cressman⁶¹ has considered a film without a photoconductive layer (cf. Fig. 2.7) and found a threshold voltage above which frost deformation will appear if the thermoplastic layer is softened by heat. This threshold voltage is expressed as

$$U_{th} = (2\tilde{\gamma}h/\epsilon_0\epsilon_{r1})^{1/2} \quad , \quad (3.1)$$

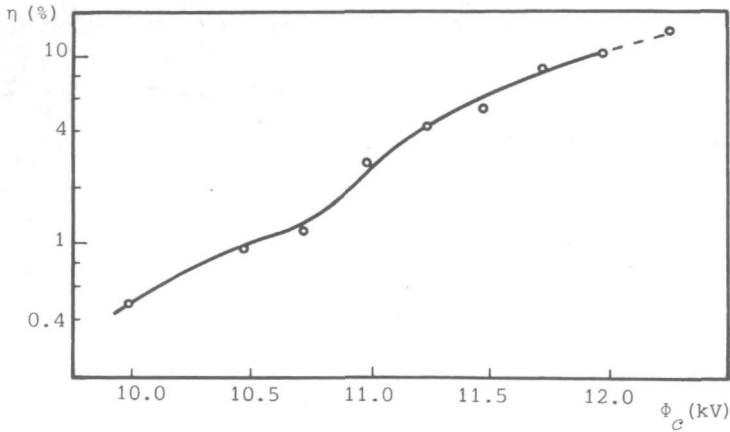


Fig. 3.1. Diffraction efficiency of a holographic grating made on our film as a function of the corona voltage; the broken line indicates that the result is not longer reproducible due to the electric breakdown.

where $\tilde{\gamma}$ is the value of the surface tension without the influence of charges, h is the thickness of the thermoplastic layer, ϵ_0 is the permittivity of vacuum (that of air assumed to be equal to it) and ϵ_{r1} the relative permittivity of the thermoplastic. Later, Matthies *et al.*⁶² have extended the investigation of U_{th} to various values of the development temperature as well as to two different modes of charging and heating. When frost deformation occurs, its amplitude appears to depend on the initial surface potential^{41, 63}.

Consequently, one will obtain some contribution from frost deformation in a holographic recording (except with the simultaneous method, see Sec. III.5) if a high potential has been given to the film surface, degrading the signal-to-noise ratio during readout, cf. Sec. II.2.4.

3. *Spatial frequency response*: the spatial frequency where the film yields a maximal response is primarily determined by the thickness of the thermoplastic layer and less significantly by Φ_s . A lower potential tends to result in a slightly lower optimal spatial frequency⁶⁰, as is shown in Fig. 3.2.

III.1.2. Factors that determine the surface potential

The attained value of Φ_s depends on the charging current, the movement speed of the corona device (when it moves over the film) and the leakage current through the film layers. In its turn, the charging current is determined by:

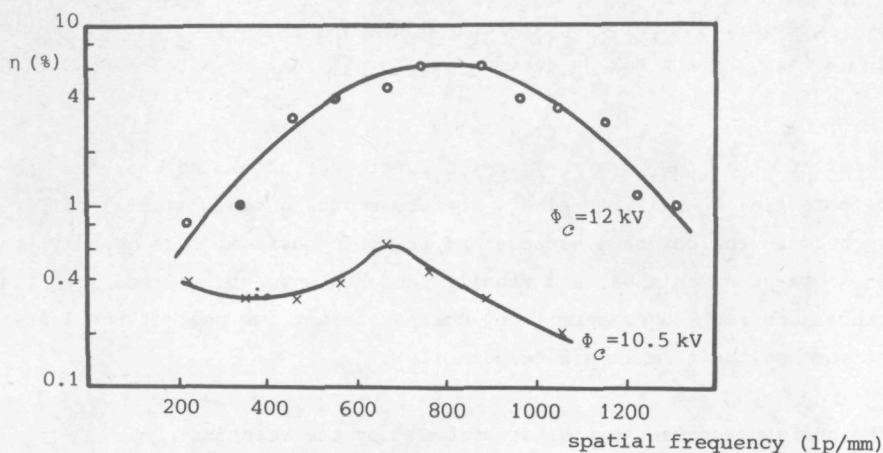


Fig. 3.2. Diffraction efficiency of our film as a function of the spatial frequency, for two values of corona voltage.

1. The voltage ϕ_c at the corona electrode and the corona onset voltage ϕ_o . The value of ϕ_o (the voltage upon which corona discharge begins to appear) depends on the configuration of the corona device [e.g. the radius of the electrode(s) and their distance to the film surface], the polarity of ϕ_c , as well as the pressure, temperature and humidity of the atmosphere⁶⁴. A greater difference between ϕ_c and ϕ_o yields a higher charging current. However, ϕ_c must not attain the value where an electric breakdown occurs between the corona electrode and the ground electrode, destructing the film in between. The breakdown potential depends on the same factors which determine the corona onset voltage ϕ_o ; e.g., a higher humidity appears to increase the breakdown potential⁶⁵.

2. The polarity of the corona voltage ϕ_c . The current from a wire electrode is greater if it has a negative voltage, instead of a positive one with the same magnitude^{64,66}. In many applications, however, the use of a positive corona polarity is preferred, since a negative corona leads to certain disadvantageous effects. One of those is the significant nonuniformity of the current along the length of the wire⁶⁶. This nonuniformity tends to yield a nonuniform potential at the surface but, moreover, the local current overshoot can approach a such high value that it leads to a local breakdown, while the average current might still be below a limit. We have tried to give a negative polarity to our corona unit, which consists of five thin Ni wires (50 μm diameter), extended parallel and equidistantly over a length of 10 cm at distances of 5 mm; the distance of the wires to the film surface is (2.7 ± 0.2) mm. We found that a breakdown already occurs at $\phi_c = -8$ kV, compared to a breakdown value of about 12 kV with

positive polarity. Another disadvantage of a negative corona is the relatively high luminosity of the corona glow⁶⁶, giving a slight unwanted exposure to the film.

3. *The potential at the film surface ϕ_s .* Due to the deposited charges, the surface potential ϕ_s will be raised, thereby reducing the potential difference $\phi_c - \phi_s$ between the corona electrode and the film surface. Consequently, the charging current diminishes, and finally vanishes when the lowered potential difference does not longer permit any corona current (we neglect the leakage current through the film layers temporarily).

The charging current can be described⁶⁴ by the relation:

$$i = \{1 - b_1 \exp[-b_2(\phi_c - \phi_o - b_3\phi_s)]\} [b_4(\phi_c - \phi_o) + b_5\phi_s](\phi_c - \phi_o - b_3\phi_s) \quad (3.2)$$

where $b_1, b_2, b_3, b_4,$ and b_5 denote factors which are constant for a given configuration of the corona device, polarity and atmospheric parameters; ϕ_o is the corona onset voltage when ϕ_s equals to zero.

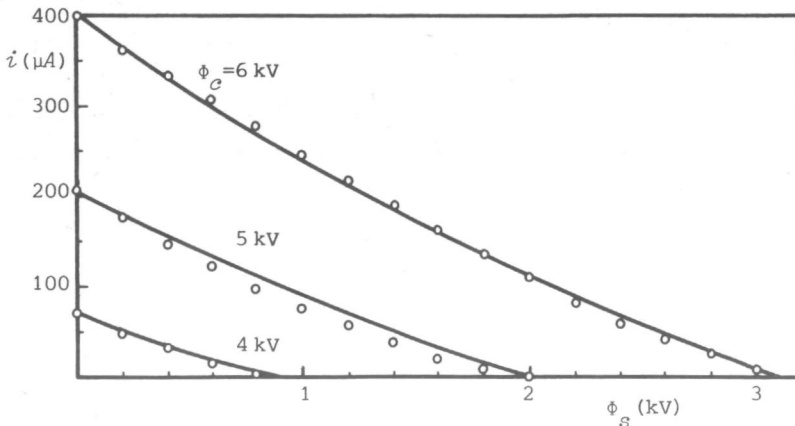


Fig. 3.3. Corona current as a function of the potential of a plate representing the film surface.

Fig. 3.3 shows an example of the $i - \phi_s$ relationship, corresponding to our corona unit. The current is measured over an $8 \times 4 \text{ cm}^2$ area at the film plane. The small circles represent the measurements, in which the film has been replaced by a metal plate connected to a variable voltage source; ϕ_s is then the voltage applied to this metal plate. The solid lines are results of calculations from Eq. (3.2) by inserting the values of respectively $b_1 = 0.503,$

$b_2 = 0.0626 \text{ kV}^{-1}$, $b_3 = 0.909$, $b_4 = 40.89 \text{ } \mu\text{A}/\text{kV}^2$, $b_5 = 21.62 \text{ } \mu\text{A}/\text{kV}^2$, and $\phi_0 = 3.18 \text{ kV}$. These values have first been obtained by applying Eq. (3.2) to the measured points at $\phi_s = 0$ and in the vicinity of $\phi_s = 2.9 \text{ kV}$.

The intersections of the curves with the ϕ_s axis indicate the maximally obtainable surface potential ϕ_s , for the case that no leakage current flows through the film. In reality, some leakage current always exists. An example of such a leakage current is shown in Fig. 3.4, where the current through our film is drawn as a function of ϕ_c . It is the steady state current measured several seconds after the corona onset, since the film sheet constitutes a capacitor which draws a larger current in the beginning of the charging.

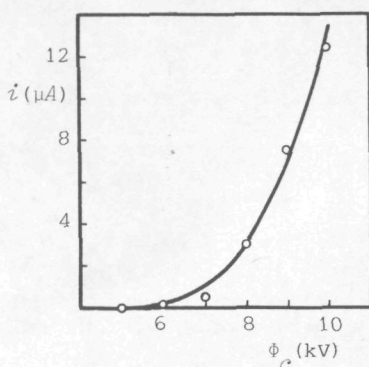


Fig. 3.4. The leakage current through our film, as a function of the voltage given to the corona wires.

Next, the current from Fig. 3.4 is depicted, now with ϕ_s along the abscissa, see the solid line in Fig. 3.5. To obtain this curve, we have applied Eq. (3.2) to the values of i and ϕ_c shown in Fig. 3.4, such that we obtain the corresponding values of the surface potential ϕ_s . In Fig. 3.5, the intersections of the leakage current curve (solid line) with the corona current curves (broken lines) indicate the maximal surface potentials in presence of a leakage current. At these points, the number of charges arriving at the film surface (transported in the corona current) is equal to the number of charges that leak away. This maximally obtainable ϕ_s is called the acceptance potential. Its value in Fig. 3.5 is 7.4 kV for $\phi_c = 10 \text{ kV}$.

We remark that when the corona voltage is removed, the charge supply to the film surface is terminated; the leakage current, however, still flows until ϕ_s drops to a value permitting no leakage current any more. This value of the potential acts as the initial surface potential for the subsequent exposure stage.

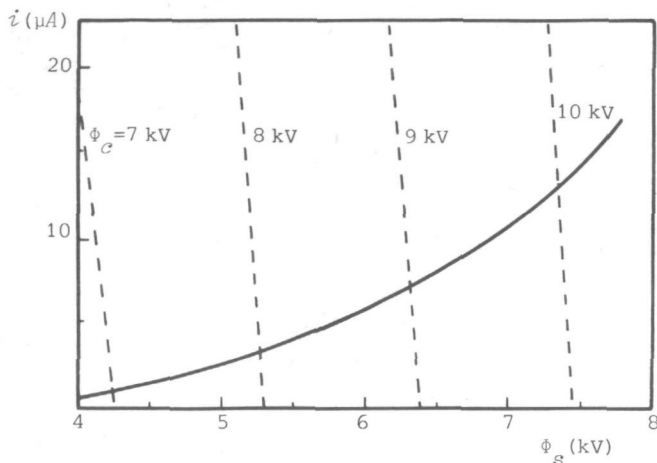


Fig. 3.5. The leakage current (solid line) and the corona current (broken lines) as a function of the surface potential.

III.1.3. Potential distribution

We suppose that, at the end of the charging stage, a uniform surface charge density σ is present at the thermoplastic surface. The (homogeneous) surface potential can then be written as

$$\Phi_s = \sigma(h+d+s)/\epsilon_1 \quad , \quad (3.3)$$

where h and d are the thickness of the thermoplastic and the photoconductive layers, respectively, while s is the thickness of the polyester substrate of our film; $\epsilon_1 = \epsilon_0\epsilon_{r1}$ is the permittivity of the materials composing the film, cf. Eq. (3.1) and Fig. 3.6. To simplify the derivation as well as the interpretation of the potential distribution in the following sections, we assume the permittivities of these materials to be the same. This assumption is reasonable since, in reality, the relative permittivity of the employed (by other authors) thermoplastic materials^{16,24,41,62} lies in the range 2.3 - 2.8, the value for the PVK : TNF photoconductor²⁶ with a molar ratio ranging from 1 : 0 to 1 : 1 lies between 2.6 and 3.2, while a polyester film⁶⁷ has a relative permittivity between 2.8 and 3.2.

We define a Cartesian coordinate system x, y, z , where the x,z -plane coincides with the thermoplastic surface, see Fig. 3.6. The potential at a point (x,y) within the film is then given by

$$\Phi = \sigma(h+d+s+y)/\epsilon_1, \quad -(h+d+s) < y < 0, \quad (3.4)$$

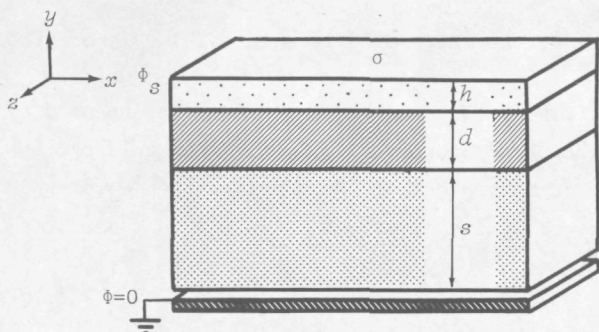


Fig. 3.6. The situation at the end of the charging stage, see Eqs. (3.3) and (3.4).

III.2. The exposure

III.2.1. The intensity pattern within the photoconductive layer

After the charging stage is finished, the film will be exposed to the object and the reference waves; we suppose both to have the form of plane waves, which are incident from the thermoplastic side of the film. Their propagation axes are parallel to the xy plane, making an angle θ'_0 and θ'_r , respectively, with the y axis, see Fig. 3.7.

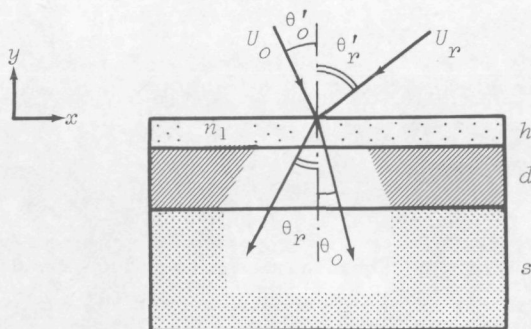


Fig. 3.7. The exposure: the object and the reference waves are incident at the film with at an incident angle of θ'_0 and θ'_r , respectively.

After refraction at the air-film interface, the angles of the propagation directions with the y axis are θ_0 and θ_r , which follow from

$$\begin{aligned} \sin\theta_o &= n_1 \sin\theta'_o, \\ \sin\theta_p &= n_1 \sin\theta'_p, \end{aligned} \quad (3.5)$$

where n_1 is the refractive index of the thermoplastic material (we ignore the absorption of this material).

Penetrating the photoconductive layer, the waves begin to be absorbed by this layer (the scattering by the photoconductor and by the thermoplastic is supposed to be sufficiently low to be neglected). We consider the (complex) index of refraction of the photoconductive layer as

$$n_{pc} = n_{re} - i n_{im} \quad (3.6)$$

where n_{re} is the real part of this refractive index, and n_{im} its imaginary part which describes the absorption.

Due to this complex refractive index, the propagation directions (the normals to the phase planes) of the reference and object waves within the photoconductor will be generally different from those in the thermoplastic layer. However, in this account we assume

$$\begin{aligned} n_{im} &\ll n_{re} \\ n_{re} &\approx n_1 \end{aligned} \quad (3.7)$$

such that (from Snell's law) the angles between the propagation directions in the photoconductor and the y axis are practically^{6,8} equal to θ_o and θ_p , for the object and the reference waves, respectively.

Then, the respective wave function of the waves within the photoconductive layer can be expressed as

$$\begin{aligned} U_o(x, y) &= |U_o| \exp \{ i\kappa [x \sin \theta_o - (h+y) \cos \theta_o] + \frac{1}{2} \alpha (h+y) / \cos \theta_o \} \\ U_p(x, y) &= |U_p| \exp \{ i\kappa [-x \sin \theta_p - (h+y) \cos \theta_p] + \frac{1}{2} \alpha (h+y) / \cos \theta_p \} \\ &\quad - (h+d) < y < -h, \end{aligned} \quad (3.8)$$

where $\Lambda_1 = 2\pi/\kappa$ is the wavelength of the light in the photoconductor and α is the (intensity) absorption coefficient of the photoconductor at the used wavelength. Note that the origin has been chosen such that the waves have zero phase at the point $(0, -h)$.

The superposition of the waves produces an intensity pattern within the photoconductive layer following

$$I = (U_o + U_r)(U_o + U_r) = |U_o|^2 \exp[\alpha(h+y)/\cos\theta_o] + |U_r|^2 \exp[\alpha(h+y)/\cos\theta_r] + 2|U_o||U_r|\exp[\alpha_\theta(h+y)] \cos[k_x x - k_y(h+y)] \quad (3.9)$$

where $\alpha_\theta = \frac{1}{2}\alpha[(1/\cos\theta_o) + (1/\cos\theta_r)]$. The parameters $\lambda_x = 2\pi/k_x$ and $\lambda_y = 2\pi/k_y$ are the spatial wavelengths of the intensity distribution in the x and the y directions, respectively, given by

$$\lambda_x = \Lambda_1/(\sin\theta_o + \sin\theta_r) \quad ,$$

$$\lambda_y = \Lambda_1/(\cos\theta_r - \cos\theta_o) \quad . \quad (3.10)$$

In the photoconductor, the negative charge-carriers generated by the illumination move along the electric field lines to accumulate on the interface at thermoplastic side, while the positive charges gather at the other side. The charge-carriers in an organic photoconductor such as PVK - TNF are not range limited²⁶. This means that if sufficient time is allowed, the number of charges arriving at one of the interfaces is equal to the number released by photo-excitation within the layer, since no charge trap exists which can seize part of the charge-carriers on their trip between the excitation point and the interface. This is still the case even if the trip involves parts of the layer that are completely unexposed²⁶.

Let the light intensity be such low that in the planes of maximal intensity (which are generally inclined with respect to the normal direction), the resulting conductivity is sufficiently small, keeping the electric field lines straight and parallel to the y axis during exposure. Then, the total charge gathered at $(x, -h)$ is simply proportional to the integral of the intensity distribution along the y axis from $(x, -h-d)$ to $(x, -h)$. A confusing question however, is which intensity distribution should be integrated.

Lee¹⁹ applied the integration to the intensity which is *incident* upon the considered field line, without taking into account the absorption coefficient α [hence, it involves Eq. (3.9) with $\alpha = 0$]. Another possibility is to integrate the intensity which is *absorbed* by all points on the field line. In our opinion, it is better to apply this latter approach, since it is actually the absorbed photon which gives rise to charge carrier generation⁶⁹. In the following account we shall see the distinction between the results of the integration from those cases.

Incident intensity distribution

To have an impression of Lee's approach, we briefly present here the

derivation. The charge at $(x, -h)$ is supposed to be proportional to the incident intensity, integrated along the line between $(x, -h-d)$ and $(x, -h)$, so that the distribution described by Eq. (3.9) must be integrated with respect to y . The integration yields (with $\alpha=0$)

$$I_{in} = \int_{-(h+d)}^{-h} I dy = d \{ |U_o|^2 + |U_p|^2 + 2|U_o||U_p| \text{sinc}(d/\lambda_y) \times \cos(k_x x + \frac{1}{2}k_y d) \} \quad (3.11)$$

in which $\text{sinc}(d/\lambda_y) = \text{sinc}(\pi d/\lambda_y) / (\pi d/\lambda_y)$. If we assume an equal intensity in the reference and object waves, the modulation of this integrated incident intensity is given by

$$m_I = \text{sinc}(d/\lambda_y) \quad (3.12)$$

which vanishes if d/λ_y equals to any integer or if it has a very large value.

Absorbed intensity distribution

We consider a subvolume $dx dy$ (having a unit length in the z direction) within the photoconductive layer, see Fig. 3.8.

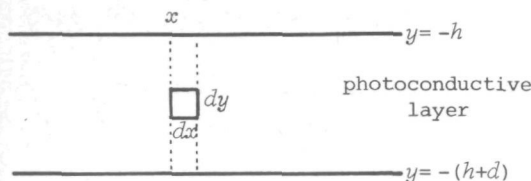


Fig. 3.8. On the derivation of the absorbed intensity.

The intensity absorbed by this subvolume is equal to

$$dI_{abs} = (\partial/\partial x + \partial/\partial y) [I - I^{(0)}] dx dy \quad (3.13)$$

where I denotes the intensity distribution in the photoconductor, described by Eq. (3.9), and $I^{(0)}$ this distribution for $\alpha=0$; we assume that no variation exists in the z direction. Eq. (3.13) is analogous to the expression for the heat dissipated by an electromagnetic wave in a unit volume within an absorbing medium⁷⁰, which is given by

$$Q_{dis} = -\vec{\nabla} \cdot \vec{P} \quad (3.14)$$

where \vec{P} is the Poynting vector. However, we have subtracted $I^{(0)}$ in Eq. (3.13),

because for the case $\alpha = 0$ a spatial variation is already present in the intensity due to the harmonic part of Eq. (3.9), while of course this variation for $\alpha = 0$ bears no relation to absorption. In Eq. (3.13) the change in I of a purely harmonic nature will be compensated by that from $I^{(0)}$, so that we obtain from $I - I^{(0)}$ the intensity change due to the absorption only.

The considered subvolume may be situated anywhere between $y = -\hbar$ and $y = -(h+d)$. If its upper side touches the interface $y = -\hbar$, one might expect the introduction of the reflection factor in Eq. (3.13). However, by inserting Eqs. (3.6), (3.7) in Fresnel's formulae for reflection⁶⁸, it will be found that the reflection is low enough to be neglected.

Then, inserting Eq. (3.9) into Eq. (3.13) we obtain

$$\begin{aligned}
 dI_{abs} = & \{ |U_o|^2 (\alpha/\cos\theta_o) \exp[\alpha(h+y)/\cos\theta_o] + |U_r|^2 (\alpha/\cos\theta_r) \times \\
 & \times \exp[\alpha(h+y)/\cos\theta_r] + 2|U_o||U_r|\alpha_\theta \exp[\alpha_\theta(h+y)] \} \times \\
 & \times \cos[k_x x - k_y(h+y)] + 2|U_o||U_r|(k_y - k_x) (\exp[\alpha_\theta(h+y)] - 1) \times \\
 & \times \sin[k_x x - k_y(h+y)] \} dx dy \quad . \quad (3.15)
 \end{aligned}$$

Integration of this expression yields

$$\begin{aligned}
 I_{abs} = \int_{y=-(h+d)}^{y=-\hbar} dI_{abs} = & \{ |U_o|^2 [1 - \exp(-\alpha d/\cos\theta_o)] + |U_r|^2 \times \\
 & \times [1 - \exp(-\alpha d/\cos\theta_r)] + 2|U_o||U_r|[1 - \exp(-\alpha_\theta d)] \cos(k_x x + k_y d) + \\
 & + 2|U_o||U_r| k_x d \operatorname{sinc}(d/\lambda_y) \sin(k_x x + k_y d) + 2|U_o||U_r| \times \\
 & \times [k_x/(\alpha_\theta^2 + k_y^2)] [\exp(-\alpha_\theta d) \{ \alpha_\theta \sin(k_x x + k_y d) + k_y \cos(k_x x + k_y d) \} + \\
 & - (\alpha_\theta \sin k_x x + k_y \cos k_x x)] \} dx \quad . \quad (3.16)
 \end{aligned}$$

We have assumed that the imaginary part of the refractive index (which depends on the absorption) is very small, cf. Eq. (3.7), and also that the absorption coefficient α is very small. Then, each exponential factor can be approximated by unity plus its argument. However, in Eq. (3.16) we do not simplify the denominator of the last term by $\alpha_\theta^2 + k_y^2 \approx k_y^2$, because we will allow the possible vanishing of k_y . Eq. (3.16) can then be written as

$$\begin{aligned}
 I_{abs} = & \{ |U_o|^2 (\alpha d / \cos \theta_o) + |U_r|^2 (\alpha d / \cos \theta_r) + 2 |U_o| |U_r| \alpha_\theta d \cos(k_x x + k_y d) + \\
 & + 2 |U_o| |U_r| k_x d \operatorname{sinc}(d/\lambda_y) \sin(k_x x + \frac{1}{2} k_y d) + 2 |U_o| |U_r| [k_x \alpha_\theta / (\alpha_\theta^2 + k_y^2)] \times \\
 & \times [\sin(k_x x + k_y d) - \sin k_x x] + 2 |U_o| |U_r| [k_x k_y / (\alpha_\theta^2 + k_y^2)] \times \\
 & \times [\cos(k_x x + k_y d) - \cos k_x x] - 2 |U_o| |U_r| [k_x \alpha_\theta^2 d / (\alpha_\theta^2 + k_y^2)] \times \\
 & \times [\sin(k_x x + k_y d) + (k_y / \alpha_\theta) \cos(k_x x + k_y d)] \} dx,
 \end{aligned}$$

which, after some mathematics, reduces to

$$\begin{aligned}
 I_{abs} = & \alpha d \{ |U_o|^2 (1/\cos \theta_o) + |U_r|^2 (1/\cos \theta_r) + |U_o| |U_r| [(1/\cos \theta_o) + (1/\cos \theta_r)] \times \\
 & \times [\cos(k_x x + k_y d) + (k_x/k_y) \sin \beta \operatorname{sinc}(d/\lambda_y) \sin(k_x x + \frac{1}{2} k_y d + \beta) + \\
 & - \sin(k_x x + k_y d + \beta)] \} dx, \quad (3.17)
 \end{aligned}$$

in which $\beta = \arctg(k_y/\alpha_\theta)$, hence $\sin \beta = k_y / (\alpha_\theta^2 + k_y^2)^{1/2}$. It can be seen that the second term between square brackets vanishes either if $\alpha_y \rightarrow \infty$ [the reference and object waves are symmetrical with respect to the y axis, cf. Eq. (3.8)], or if $\lambda_y \rightarrow 0$, both cases with a finite $\lambda = 2\pi/k$. In the first case, which in practice can easily be realized, Eq. (3.17) simplifies to

$$I_{abs} = (\alpha d / \cos \theta_o) (|U_o|^2 + |U_r|^2 + 2 |U_o| |U_r| \cos k_x x) dx. \quad (3.18)$$

Apart from a constant factor, the derivation of Lee, Eq. (3.12), leads to the same result if $\lambda_y \rightarrow \infty$. In our model, the charge generation due to the intensity distribution under general conditions, follows from Eq. (3.17). Whether this happens in reality, can only be verified by determining the charge generation in the photoconductive layer. No data concerning this are presently available.

III.2.2. A model for the relation between the absorbed intensity and the potential in the photoconductive layer

Commonly in considerations on photothermoplastic films, it has been assumed^{38,71} that after an holographic exposure, a sinusoidal charge distribution exists at the thermoplastic-photoconductive interface. To our knowledge, however, the transfer mechanism from the intensity to this charge

distribution has never been formulated.

Here, we propose a relation connecting the absorbed intensity distribution I_{abs} to the resulting potential difference $\Delta\phi_{pc}$ across the photoconductor. We begin with the representation of the photoconductive layer by an electric lumped circuit, see Fig. 3.9.

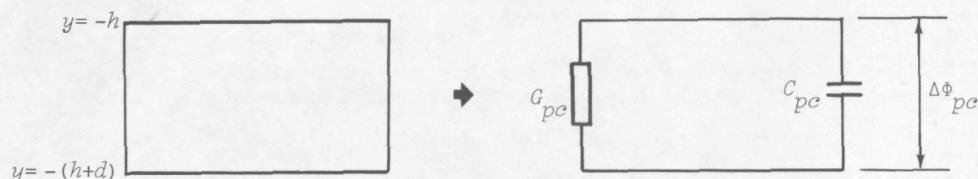


Fig. 3.9. Representation of the photoconductive layer by an electric lumped circuit.

There, the following equation applies:

$$C_{pc} [d(\Delta\phi_{pc})/dt] + G_{pc} \Delta\phi_{pc} = 0 \quad , \quad (3.19)$$

where C_{pc} is the capacitance and G_{pc} the conductance of the photoconductive sheet, both are taken per unit area in the xz plane; t indicates the time. The capacitance is supposed not to be affected by the absorbed light, such that the photoinduced current J_p is solely determined by the second term in Eq. (3.19):

$$J_p = G_{pc} \Delta\phi_{pc} \quad . \quad (3.20)$$

For a constant $\Delta\phi_{pc}$, the photocurrent J_p (corrected for the dark current) is linearly related to the incident intensity^{26, 58}. Since in the reported experiments use has been made of a homogeneous light distribution, the absorbed intensity is simply directly proportional to the incident intensity, cf. Eqs. (3.9) and (3.16) for e.g. $|U_0| = 0$. Then, we may write

$$J_p = c_1 I_{abs} \quad , \quad (3.21)$$

where c_1 is a proportionality factor whose value (for a given photoconductor) depends only on $\Delta\phi_{pc}$.

According to Fig. 4 by Schaffert²⁶, pertinent to a constant incident intensity, the photocurrent depends on the potential difference through a relation that he approximated as $(\Delta\phi_{pc})^{2.3}$. Upon careful examination of that

figure, however, we found that the relation can be better described by $(\Delta\phi_{pc})^{\bar{l}}$, with \bar{l} between 1.9 and 2.3. For our derivation, we simplify this relation by taking $\bar{l}=2$, a value which has been also found empirically by Killat and Terrell⁵⁸. To justify this exponent, the derivation result will later be compared with some published experimental results. At this stage we write

$$c_1 = c_2 (\Delta\phi_{pc})^2 \quad , \quad (3.22)$$

with c_1 a proportionality factor depending on the photoconductive material.

If I_{abs} as well as $\Delta\phi_{pc}$ have other (constant) values, we obtain from Eqs. (3.21) and (3.22) the relation:

$$J_p = c_2 I_{abs} (\Delta\phi_{pc})^2 \quad . \quad (3.23)$$

For other photoconductors, the value of c_2 will change according to the material composition and the material thickness. Comparing Eq. (3.23) to Eq. (3.20), the conductance G_{pc} can now be written as

$$G_{pc} = c_2 I_{abs} \Delta\phi_{pc} \quad , \quad (3.24)$$

cf. Stewart *et al.*¹⁵, where G_{pc} was supposed to depend only on the incident intensity.

We insert G_{pc} back into Eq. (3.19):

$$C_{pc} [d(\Delta\phi_{pc})/dt] + c_2 I_{abs} (\Delta\phi_{pc})^2 = 0 \quad . \quad (3.25)$$

Through the following step:

$$\int_{\Delta\phi_{pci}}^{\Delta\phi_{pc}} [C_{pc}/(\Delta\phi_{pc})^2] d(\Delta\phi_{pc}) + \int_0^{t_e} c_2 I_{abs} dt = 0 \quad , \quad (3.26)$$

with t_e denoting the exposure time, we find a solution to Eq. (3.25):

$$\Delta\phi_{pc} = \Delta\phi_{pci} / (1 + c\Delta\phi_{pci} E_{abs}) \quad , \quad (3.27)$$

where $\Delta\phi_{pci}$ is the initial (dark) potential difference across the photoconductor, $c = c_2/C_{pc}$, and $E_{abs} = I_{abs} t_e$ is the exposure energy. This is our proposal for the relation between the absorbed intensity distribution and the resulting potential change across the photoconductive layer.

We verify now Eq. (3.27) with the experimental results published by other authors. In Fig. 3.10.a, the circles indicate measurement results by Credelle and Spong¹³; the solid line is calculated from Eq. (3.27) in which a value of $c = 6.3 \times 10^{-4} (\text{V } \mu\text{J}/\text{cm}^2)^{-1}$ has been inserted. In Fig. 3.10.b, the experimental results of Bergen²⁸ are depicted by the small circles; the solid lines are our calculated results, in which $c = 4 \times 10^{-4} (\text{V } \mu\text{J}/\text{cm}^2)^{-1}$ is used for both lines. [Since the intensity in those experiments is homogeneous, E_{abs} is directly proportional to the incident exposure energy, the proportionality factor being included in c , so that E_{abs} in Eq. (3.27) can be read as the incident exposure]. It is seen that the agreement between experiments and our theoretical relation is very satisfactory.

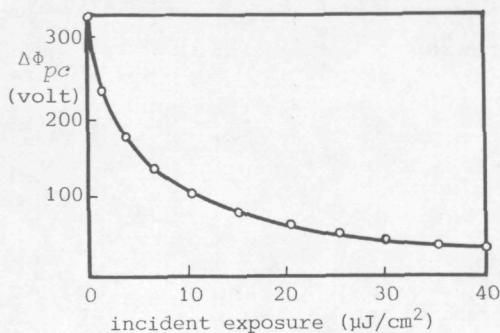


Fig. 3.10.a. Our calculation result from Eq. (3.27), the solid line, is compared to the experimental results (the circles) from Credelle and Spong¹³.

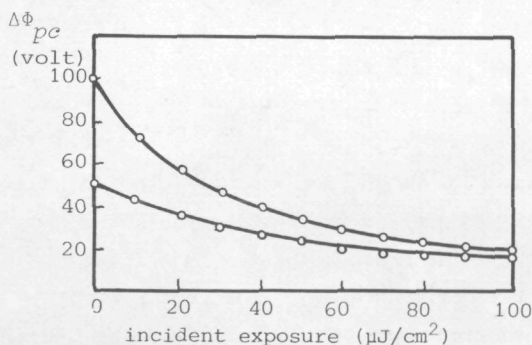


Fig. 3.10.b. Our calculation results, the solid lines, are compared to the measurement results from Bergen²⁸.

We remark, however, that this good agreement for a broad range of exposures is especially valid if the incident intensity is homogeneous. For a spatially varying intensity distribution, such as a set of inclined interference planes, either of the two conditions mentioned previously should be considered. In the first of these, the conductivity induced should be sufficiently low to keep the

electric field lines straight during exposure, and parallel to the y axis. Otherwise, we may not use the derivation starting from Eq. (3.19). This condition can be realized e.g. by a low $\Delta\phi_{pci}$ or a low E_{abs} , which is also a necessary condition for the linearity between exposure and potential [see the discussion around Eq. (3.28)].

The alternative condition is to have an absorption of the photoconductor such high that the absorbed intensity is similar to the intensity distribution at the thermoplastic-photoconductive interface, the inclined direction of the interference planes having an insignificant effect, cf. Eq. (3.18). This condition will be employed in the derivation of the potential distribution in Sec. III.2.3.

The relation between the absorbed intensity (or exposure energy) and the resulting potential difference is in general non-linear. For the first derivative of $\Delta\phi_{pc}$ to E_{abs} we have from Eq. (3.27):

$$d(\Delta\phi_{pc})/dE_{abs} = -c(\Delta\phi_{pci})^2/(1+c\Delta\phi_{pci}E_{abs})^2, \quad (3.28)$$

which is only a constant (hence a linear relation between exposure and potential) if the exposure or the initial potential difference is such low that in the denominator $c\Delta\phi_{pci}E_{abs}$ can be ignored with respect to unity. The latter requirement can be quite severe. For the case of Fig. 3.10.a, if we consider an inaccuracy of less than 10%, i.e. $c\Delta\phi_{pci}E_{abs}$ smaller than 0.1, the incident exposure energy may not exceed $0.5 \mu\text{J}/\text{cm}^2$. In Fig. 3.10.b, the same linearity is approximated when the incident exposure is less than $2.5 \mu\text{J}/\text{cm}^2$ for $\Delta\phi_{pci} = 100 \text{ V}$ and less than $5.0 \mu\text{J}/\text{cm}^2$ for $\Delta\phi_{pci} = 50 \text{ V}$.

A question which can induce discussion is whether a double exposure hologram on a photothermoplastic film produces in the readout the sum of the two recorded distributions faithfully. It has been suspected that after the first exposure, the decreased potential difference $\Delta\phi_{pc}$ would not permit any useful exposure afterwards, or that the two successively recorded latent images will interact electrically and thus degrade the readout³⁴.

To study this, we write the potential difference just after first exposure E_{abs1} as:

$$\Delta\phi_{pc1} = \Delta\phi_{pci}/(1+c\Delta\phi_{pci}E_{abs1}) \quad (3.29)$$

Then, the film is exposed to the light distribution E_{abs2} . The potential

difference after this second exposure is given by:

$$\begin{aligned} \Delta\phi_{pc2} &= \Delta\phi_{pc1} / (1 + c \Delta\phi_{pc1} E_{abs2}) = \frac{\Delta\phi_{pci} / (1 + c \Delta\phi_{pci} E_{abs1})}{1 + c E_{abs2} \Delta\phi_{pci} / (1 + c \Delta\phi_{pci} E_{abs1})} = \\ &= \Delta\phi_{pci} / [1 + c \Delta\phi_{pci} (E_{abs1} + E_{abs2})] \quad . \end{aligned} \quad (3.30)$$

Again, the resulting potential difference can be considered as a response of the sum of the two recorded distributions only if the total exposure or the initial potential difference is such low that the second term in the denominator is much smaller than unity.

III.2.3. Potential distribution

We assume the absorption in the photoconductor layer to be sufficiently high such that the absorbed intensity distribution is represented by Eq. (3.18). Then, apart from a constant phase factor, we can write

$$I_{abs} = I_0 (1 + m_I \cos k_x x) \quad , \quad (3.31)$$

where I_0 denotes the constant part and m_I the modulation of the absorbed intensity. The potential difference across the photoconductor at the end of the exposure is equal to

$$\Delta\phi_{pc} = \Delta\phi_{pci} / [1 + c \Delta\phi_{pci} E_0 (1 + m_I \cos k_x x)] \quad . \quad (3.32)$$

To derive the potential distribution in both the thermoplastic and photoconductive layer, we must solve the two dimensional Laplace's equation

$$(\partial^2/\partial x^2 + \partial^2/\partial y^2) \phi = 0 \quad , \quad (3.33)$$

with the following boundary conditions:

$$\phi_{su} = 0 \quad , \quad y = - (h+d+s) \quad , \quad (3.34.a)$$

$$\phi_{pc} = \phi_{su} \quad , \quad y = - (h+d) \quad , \quad (3.34.b)$$

$$\phi_{tp} = \phi_{pc} \quad , \quad y = -h \quad , \quad (3.34.c)$$

$$\phi_{air} = \phi_{tp} \quad , \quad y = 0 \quad , \quad (3.34.d)$$

$$\phi_{air} < \infty \quad , \quad y = Y_m \quad , \quad (3.34.e)$$

$$\left[-\frac{\partial \phi_{air}}{\partial y} \right] - \epsilon_1 \left[-\frac{\partial \phi_{tp}}{\partial y} \right] = \sigma \quad , \quad y = 0 \quad , \quad (3.34.f)$$

$$\epsilon_1 \left[-\frac{\partial \phi_{tp}}{\partial y} \right] - \epsilon_1 \left[-\frac{\partial \phi_{pc}}{\partial y} \right] = -\sigma_t (1 + m_\sigma \cos k_x x) \quad , \quad y = -h \quad , \quad (3.34.g)$$

$$\epsilon_1 \left[-\frac{\partial \phi_{pc}}{\partial y} \right] - \epsilon_1 \left[-\frac{\partial \phi_{su}}{\partial y} \right] = \sigma_t (1 + m_\sigma \cos k_x x) \quad , \quad y = -(h+d) \quad . \quad (3.34.h)$$

Here, ϕ_{su} , ϕ_{pc} , ϕ_{tp} , and ϕ_{air} are the potential in the substrate, photoconductor, thermoplastic layer, and air, respectively; Y_m is a limiting value in the order of $10/k_x$; σ_t denotes the photoinduced charge accumulated at the photoconductive interfaces, m_σ being its modulation.

To simplify the derivation, we have introduced σ_t and m_σ instead of the parameters used in Eq. (3.32) in the boundary conditions; in their turn σ_t and m_σ can be expressed in terms of the factors constituting Eq. (3.32).

Nevertheless, the derivation is lengthy. Here, we present only the result (see Appendix A for the concise derivation):

$$\begin{aligned} \phi_{pc} = & \frac{\sigma}{\epsilon_1} (h+d+s+y) - \frac{\sigma_t}{\epsilon_1} (h+d+y) - \frac{\sigma_t m_\sigma}{\epsilon_1 k_x} \frac{C \cos k_x x}{\sinh k_x (d+s) - \sinh k_x s} \times \\ & \times [(\sinh k_x h + \epsilon_1 \cosh k_x h) \sinh k_x (h+d+s+y) + \\ & + \sinh k_x s (\sinh k_x y - \epsilon_1 \cosh k_x y)] \quad , \end{aligned} \quad (3.35)$$

$$\phi_{tp} = \frac{\sigma}{\epsilon_1} (h+d+s+y) - \frac{\sigma_t}{\epsilon_1} d + \frac{\sigma_t m_\sigma}{\epsilon_1 k_x} C (\sinh k_x y - \epsilon_1 \cosh k_x y) \cos k_x x \quad , \quad (3.36)$$

$$\sigma_t = B \sigma / (1 + B) \quad , \quad (3.37)$$

$$m_\sigma = m_I k_x d / [A (1 + B + B m_I \cos k_x \xi_I)] \quad , \quad (3.38)$$

where

$$C = \frac{\sinh k_x (d+s) - \sinh k_x s}{\sinh k_x (h+d+s) + \epsilon_1 \cosh k_x (h+d+s)} \quad , \quad (3.39)$$

$$B = c \sigma E_0 / \epsilon_1 \quad , \quad (3.40)$$

$$\begin{aligned}
 A = & \{ (\sinh k_x h + \epsilon_1 \cosh k_x h) [\sinh k_x (d+s) - 2 \sinh k_x s] + \\
 & + \sinh k_x s [\sinh k_x (h+d) + \epsilon_1 \cosh k_x (h+d)] \} \times \\
 & \times [\sinh k_x (h+d+s) + \epsilon_1 \cosh k_x (h+d+s)]^{-1} .
 \end{aligned} \tag{3.41}$$

In our derivation, we have divided the film in L slices perpendicular to the x axis such that the denominator at the right-hand side of Eq. (3.38) within each slice can be regarded as a constant; ξ_l denotes the value of x at the left edge of slice l , $l=0, 1, 2, \dots, L-1$, see also Chapter IV for this technique.

It is seen from Eq. (3.38) that the charge distribution at the thermo-plastic-photoconductive interface is not a purely sinusoidal function of x (contrary to the assumption made by some authors^{38, 56}). In fact, for $m_I = 1$ (equal intensity of the reference and the object beams) and $\cos k_x \xi_l = 1$, the charge modulation is equal to $m_\sigma = k_x d / [A(1+2B)]$, while for $\cos k_x \xi_l = -1$ it is given by $m_\sigma = k_x d / A$.

Using these values, from Eq. (3.36) we obtain the modulation of the potential distribution at the surface, $y=0$:

$$m_{\phi_{tp}, y=0} = \frac{\sigma_t \epsilon_1 C d}{A(1+2B)[\sigma(h+d+s) - \sigma_t d]} \quad \text{for } \cos k_x x = 1 \quad , \tag{3.42.a}$$

$$m_{\phi_{tp}, y=0} = \frac{\sigma_t \epsilon_1 C d}{A[\sigma(h+d+s) - \sigma_t d]} \quad \text{for } \cos k_x x = -1 \quad . \tag{3.42.b}$$

Since the modulation at the maximum is not equal to that at the minimum, it is clear that the potential distribution is not purely sinusoidal.

To have an idea of the relation between these modulations and the thickness d , we first insert the values for our film: $h = 0.5 \mu\text{m}$, $d = 1 \mu\text{m}$, $s = 50 \mu\text{m}$ into Eqs. (3.39) and (3.41), choosing $k = 4.71 \mu\text{m}^{-1}$ which corresponds to the spatial frequency 750 lp/mm (cf. Fig. 3.2), and a value of 2.8 is inserted for ϵ_1 , cf. Sec. III.1.3. Next, we again insert the same figures, except that we put s equal to zero, so that the calculation applies for the film type of Fig. 2.1.a (no layer exists between the conductive coating and the photoconductor); the thickness $h = 0.5 \mu\text{m}$ and $d = 1 \mu\text{m}$ are then very near to those used by Lo *et al.*⁶⁰ For both $s = 50 \mu\text{m}$ and $s = 0$, the factors A and C turn out to be independent of d for $d > 0.8 \mu\text{m}$. Their values for A are 0.993 ($s = 50 \mu\text{m}$) and 0.502 ($s = 0$), respectively, and $C = 0.025$ for both $s = 50 \mu\text{m}$ and $s = 0$.

Consequently, the relation between the potential modulations [Eqs. (3.42.a.) and (3.42.b)] and d is primarily determined by $\sigma_t d / [\sigma(h+d+s) - \sigma_t d]$, which

can be readily seen to increase with an increase in d (such that d becomes more and more significant with respect to h and s). This larger potential modulation for a thicker photoconductor has been mentioned in Sec. II.1.3.

If we assume that the deformation is mainly caused by the electric forces at the thermoplastic surface, $y = 0$, we are interested in the electric field strengths E_x and E_y at this surface, in the x and the y direction, respectively, which follow from

$$E_x = \left[-\frac{\partial \phi_{tp}}{\partial x} \right]_{y=0} = -\sigma_t m_\sigma C \sin k_x x \quad , \quad (3.43)$$

$$E_y = \left[-\frac{\partial \phi_{tp}}{\partial y} \right]_{y=0} = -\frac{\sigma}{\epsilon_1} - \frac{\sigma_t}{\epsilon_1} m_\sigma C \cos k_x x \quad . \quad (3.44)$$

For $s = 0$ these equations are similar to those derived by Lee⁵⁶. The negative sign in the expression for E_y means that the field is pointing toward the film interior. In the expression for E_x , the negative sign denotes that the field is directed to the nearest maximum of the cosine function. This situation can be better examined in Fig. 3.11, where the electric fields at the surface are schematically depicted, together with the not purely sinusoidal distribution of the charge at the interface.

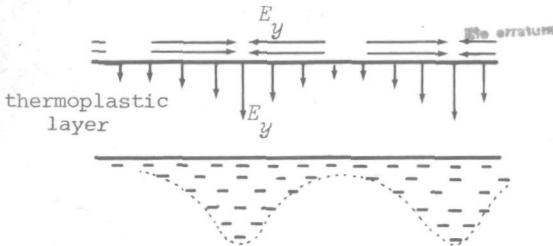


Fig. 3.11. Schematic representation of the electric fields at the thermoplastic surface and the not purely sinusoidal charge distribution at the interface.

It is seen that, when the thermoplastic material is softened directly after exposure (the method suitable for our film), E_x tends to ripple the layer such that it becomes thicker at the maxima of the cosine function, i.e. at places where the incident intensity was maximal. This deforming force resulting from E_x , however, is opposed to that from the harmonic part of E_y , which tries to make the layer thinner at those maxima. In general, the deforming force induced by E_x is stronger, because its amplitude is determined by $\sigma_t m_\sigma C$, while the amplitude of the harmonic part of E_y is given by $\sigma_t m_\sigma C / \epsilon_1$, with ϵ_1 equals to 2.8.

The oppsing effect of E_y is actually one of the reasons why the charge-expose-develop method tends to yield a lower diffraction efficiency, than the sequential method (under the same recording conditions) which will be considered in the next section.

III.3. Recharging

In the sequential mode of recording, the film is recharged to acquire a homogeneous surface potential after exposure. In Sec. II.5 we have mentioned that this method, as well as the simultaneous method, are not suitable for our film (which has a 50 μm thick substrate between the conductive coating and the photoconductor). However, to clarify the analysis, and especially the difference from the previous stage, we still include the substrate thickness s in the following considerations. The reasons for the unsuitability of our film, will be discussed at the latter part of this section.

We remark that at the end of the recharging stage, the thermoplastic surface ($y = 0$) acquires a uniform potential, given by

$$\phi'_s = D\sigma(h+d+s)/\epsilon_1 \quad , \quad (3.45)$$

in which D denotes the relative increase of the potential with respect to that before exposure, cf. Eq. (3.3) (if the surface is recharged to the same potential, D is equal to unity). We indicate the various functions for this case by a prime.

We can solve Laplace's equation by using the boundary conditions (3.34.a) - (3.34.e), (3.34.g), (3.34.h) and applying Eq. (3.45) instead of (3.34.f). We then obtain

$$\begin{aligned} \phi'_{pc} = & \frac{D\sigma}{\epsilon_1} (h+d+s+y) - \frac{\sigma_t}{\epsilon_1} \frac{(h+d+s)h + (h+s)y}{h+d+s} + \\ & - \frac{\sigma_t m_\sigma}{\epsilon_1 k_x} \frac{\cos k_x x}{\sinh k_x (h+d+s)} \times [\sinh k_x h \sinh k_x (h+d+s+y) + \\ & + \sinh k_x s \sinh k_x y] \quad , \quad (3.46) \end{aligned}$$

$$\begin{aligned} \Phi'_{tp} = & \frac{D\sigma}{\epsilon_1} (h+d+s+y) + \frac{\sigma_t}{\epsilon_1} \frac{d y}{h+d+s} + \\ & + \frac{\sigma_t m_\sigma}{\epsilon_1 k_x} \frac{[\sinh k_x (d+s) - \sinh k_x s] \sinh k_x y \cos k_x x}{\sinh k_x (h+d+s)}, \end{aligned} \quad (3.47)$$

where σ_t and m_σ are given by Eqs. (3.37) and (3.38).

The electric field strengths at the surface are given by

$$E'_x = 0, \quad (3.48)$$

$$\begin{aligned} E'_y = & -\frac{D\sigma}{\epsilon_1} - \frac{\sigma_t}{\epsilon_1} \frac{d}{h+d+s} - \frac{\sigma_t m_\sigma}{\epsilon_1} \times \\ & \times \frac{[\sinh k_x (d+s) - \sinh k_x s] \cos k_x x}{\sinh k_x (h+d+s)}. \end{aligned} \quad (3.49)$$

It is seen that the electric field is now entirely pointing toward the film interior. As compared to E_y (before recharging), Eq. (3.44), the amplitude of the harmonic part has now increased by a factor $[\sinh k_x (d+s) - \sinh k_x s] \times [C \sinh k_x (h+d+s)]^{-1}$, which is equal to 3.8 for both $s = 0$ and $s = 50 \mu\text{m}$ if we insert the same parameter values as before.

Hence, if we assume that the deformation is mainly caused by forces at the thermoplastic surface, the higher diffraction efficiency in the sequential method (as compared to that in the charge-expose-develop method) as observed by several authors^{16, 56, 72}, is attributed to the following causes:

1. In the charge-expose-develop method, the electric field has both components, the tangential and the normal to the surface, which lead to forces opposing each other. The tangential field will win, but the opposing effect has reduced the total deforming force. Such an opposing effect does not exist in the sequential method, because the tangential electric field at the surface vanishes.
2. The magnitude of the electric field responsible for deformation is larger than that in the charge-expose-develop method.

Our film is not suitable for the sequential (or the simultaneous) method. This is because in these techniques the thermoplastic surface (after or during exposure) must be charged to a uniform potential. As we shall show, this is a severe requirement.

First, for the factor B , see Eq. (3.40), we choose the value of 4 (for the case of a homogeneous intensity distribution, this value corresponds to the experimental result of Bergen²⁸ at $\Delta\phi_{pci} = 100$ V and $E_0 = 100 \mu\text{J}/\text{cm}^2$, see Fig. 3.10.b). We then insert this value, together with the previously calculated A and C , in Eqs. (3.37), (3.42.a), and (3.42.b). Thus, we obtain for the relative difference between the maximal and the minimal surface potential:

$$\begin{aligned} \frac{\delta\phi_{tp, y=0}}{\phi_{tp, y=0}} &= m_{\phi_{tp, y=0, \cos k_x x = 1}} + m_{\phi_{tp, y=0, \cos k_x x = -1}} = \quad (3.50) \\ &= .0012 \quad \text{for } s = 50 \mu\text{m}, \\ &= .18 \quad \text{for } s = 0. \end{aligned}$$

These differences should be compensated in the recharging stage (to obtain a homogeneous surface potential), such that the potential variation is transferred into a surface charge density variation. In practice, however, the potential homogeneity which can be deposited by a corona device is restricted within a few percents^{23, 35}. This means that for the case $s = 0$, see Eq. (3.50), the 18% variation still can be appreciably eliminated. For our film, however, $s = 50 \mu\text{m}$, the 0.12% difference is significantly lower than the accuracy limit. Even if the surface potential from recharging is made higher (which might be expected to be better because of "drowning" the existing variation), it still has a few percent random spatial fluctuation, larger than the variation which is to be canceled.

These discussions have been based on $B = 4$, a relatively large value which has reduced $\Delta\phi_{pc}$ considerably, see Fig. 3.10.b and our consideration prior to Eq. (3.50). For a smaller B , the resulting relative difference of the surface potential is still lower, so that the homogeneity requirement is more severe. Hence, unless a charging device or technique is available which can yield a potential homogeneity in the order of tenths of a per mill, our film is not suitable for the sequential method of recording (as well as for other methods requiring a uniform surface potential after or during exposure).

In fact, the failure of making the surface again equipotential will degrade the hologram. As we have seen, the effects of the recharging stage are to eliminate the tangential electric field at the surface (thus canceling the opposing effect), and to increase the normal one. If an equipotential state is not fully achieved, the opposing effect does not entirely vanish. This effect becomes even disadvantageous, because the normal electric field strength increases somewhat while the tangential one will be decreased, such that those

field strengths become comparable now, resulting in a low total deforming force. This has been confirmed by our experiments with our film, where recharging after exposure produced a diffraction efficiency lower than that from the charge-heat-develop method.

III.4. Development

Factors related to the thermoplastic polymer, which play a significant role in the thermal development stage are its viscosity, its electric resistivity, its surface tension and the temperature dependence of those parameters. The surface tension changes hardly in the temperature range of the development. This is shown in Fig. 3.12, where the relative change of the parameters is depicted as a function of the temperature θ , based upon data and theoretical considerations from several authors⁷³⁻⁷⁸.

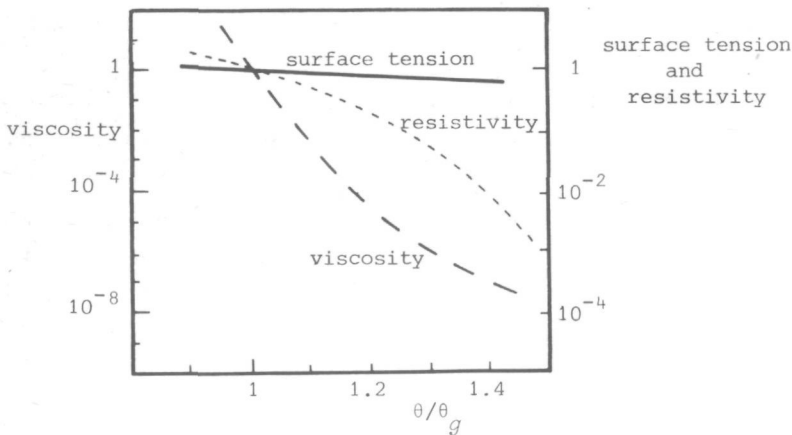


Fig. 3.12. Schematic representation of the relative change of the parameters in the vicinity of θ_g , based upon data and theory from several authors⁷³⁻⁷⁸.

At room temperature, the thermoplastic material has a very large viscosity; such a rigid layer can not be deformed. If the film temperature is raised and approaches θ_g of the thermoplastic; its viscosity decreases and the existing potential or charge distribution begins to deform the layer. This electric deforming force is resisted by the surface tension, which tries to make the layer as flat as possible.

If the film is further heated, the electric resistivity of the thermoplastic polymer decreases sharply, see Fig. 3.12. A considerable amount of the

deposited charges (at the thermoplastic surface) leak away such that the electric force diminishes. On the other hand, the resisting force increases when the radius of curvature in the extremes of the rippled surface becomes smaller, hence when the deformation amplitude has increased. Then, at a certain stage the electric force becomes equal to the resisting one; the film is just developed to the correct degree. By removing the heat supply, the deformation will be frozen.

If, however, the film temperature is further increased, the resisting force will be stronger than the deforming force. Moreover, the viscosity becomes such low that the surface tension can easily reflaten the thermoplastic surface. When this surface flattening has completed, the previously recorded information is erased.

Obviously, the most critical factor in the thermal development is the film temperature. For instance, Gray and Barnett³² had to develop their film at 55°C within an accuracy of 1°C. In Fig. 3.13, the diffraction efficiency of our film is shown as a function of the (electric) energy needed to develop the film thermally. In this experiment, the development was carried out by discharging a capacitor with a preadjusted voltage through the conductive layer (development time ≈ 0.15 s). It is seen that a change of 5% of the development energy reduces the diffraction efficiency by about 75%. A similar strong dependence has also been observed by other authors^{35,72}.

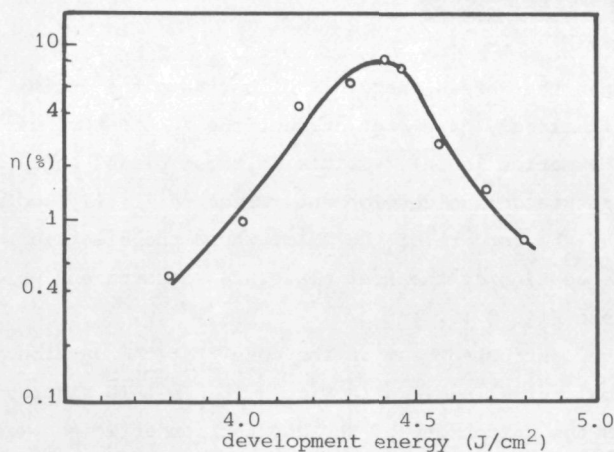


Fig. 3.13. Diffraction efficiency of our film as a function of the electric energy needed for the thermal development. Development time ≈ 0.15 s.

In practice, it is after development possible to ascertain whether the given energy was too low or too high. If the energy lies under its optimal value, it is not sufficient to raise the whole frame area to the development temperature to obtain an entirely developed film (in our case, the frame area is the size of the auxiliary glass plate with the conductive coating, the so called heat plate, see Sec. II.1.1 and Chapter V). In particular, during the recording process, our film must stick to the heat plate. If some dust contamination or tiny air bubbles are present between certain parts of the film and the plate, these parts will have an imperfect heat contact. With an insufficient heat energy, the hologram will locally not fully be developed, resulting in a nonuniformity in the diffraction efficiency at readout. An example of such a nonuniformity is shown in Fig. 3.14.

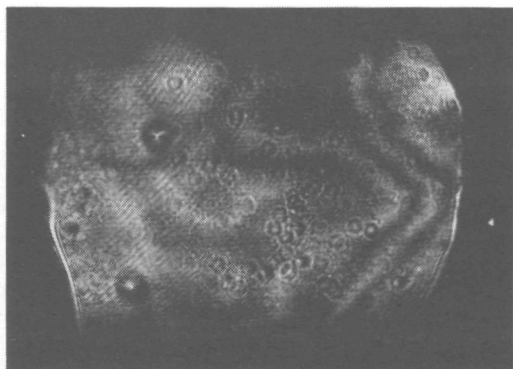


Fig. 3.14. Cross section of the reconstructed beam from a hologram developed with an insufficient energy.

On the other hand, when the chosen energy is higher than the optimal value, a part of the hologram will already have been erased (the temperature was locally too high). The deformation is only visible in those places which acquired the proper temperature during development. These relatively cooler sections are situated along the borders of the film, where the electric contacts to the conductive coating of the heat plate are situated and which dissipate the heat away, see Fig. 3.15.

A photograph of the reconstructed beam in the case that the development energy equals to its optimal value is given in Fig. 3.16. In this figure, a significant improvement in the uniformity of the diffraction efficiency is obtained. However, traces of an inhomogeneous efficiency are still observable; the measured efficiency variation over the whole frame area uses to be about 33%. Among other factors, this unevenness is caused by the imperfect heat contact mentioned previously (although its effect is less significant now than in Fig. 3.13). In relation to this efficiency unevenness, all the measured

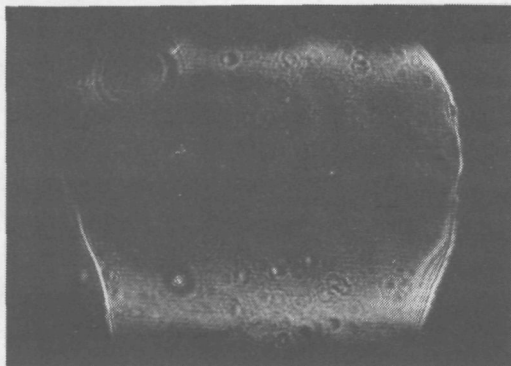


Fig. 3.15. Cross section of the reconstructed beam when the development energy has been too high.

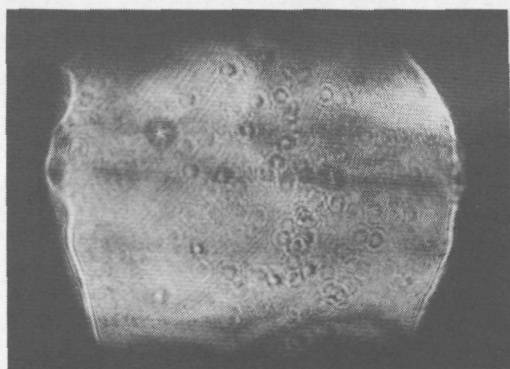


Fig. 3.16. Cross section of the reconstructed beam from a hologram developed with optimal energy.

diffraction efficiencies reported in this work are based upon the maximal values.

Another factor that plays an important role in the development stage is the development time t_d . Values of t_d from as short as tenths of a millisecond to as long as tens of minutes have been reported^{28,40,58,79}, but usually it is in the range between tenths of a second and a few seconds.

Further considerations on the development time will be given in Chapter VI.

III.5. Readout

III.5.1. Diffraction efficiency

The diffraction efficiency of a *developed* hologram on a photothermoplastic film depends on the shape⁸⁰ of the deformation profile (e.g. whether it is sinusoidal, square or triangular), the deformation amplitude, the angle of incidence and the wavelength of the light used at reconstruction, and the refractive index of the thermoplastic material. These factors determine also whether the hologram is classified as a thin or a thick hologram or something intermediate, in its turn determining the applicable formula for calculation of the diffraction efficiency⁸⁰. For instance, for a hologram with a sinusoidal deformation, whose spatial wavelength is considerably larger than both its amplitude and the wavelength of the reconstruction beam (which is supposed to be practically perpendicular to the film plane), the diffraction efficiency is given by (see Sec. II.3.3)

$$\eta = J_1^2 [2\pi(n_1 - 1)a_p/\Lambda_0] \quad (3.51)$$

The parameters that affect the diffraction efficiency include the refractive index n_1 and the wavelength Λ_0 at reconstruction, we assume that the recording conditions leading to a certain deformation amplitude a_p are constant.

It would be favourable to employ a thermoplastic material having a high value of n_1 , although the possibilities therefore are limited, because the refractive index of most thermoplastic polymers⁸¹ is confined to the range between 1.45 and 1.60.

From Fig. 3.17, one can see the diffraction efficiencies of holographic gratings (crosses), each recorded and reconstructed with the following wavelengths from a krypton laser: 647 nm, 568 nm, 521 nm, 483 nm, 476 nm and 468 nm, respectively. For comparison, the circles represent the efficiencies of a grating recorded with red light (647 nm) and reconstructed with those other wavelengths; at 647 nm the efficiencies being the same. The dashed line is calculated from Eq. (3.51) by inserting the value of a_p found from the efficiency at 647 nm, and $n_1 = 1.6$.

The increase of the η at the shorter wavelengths is clearly seen. The crosses and the circles have approximately the same rate of increase. This can be explained by noting that the photoconductor in our film has a panchromatic spectral sensitivity¹⁷, so that the produced deformations (under the same conditions) will have approximately equal amplitudes.

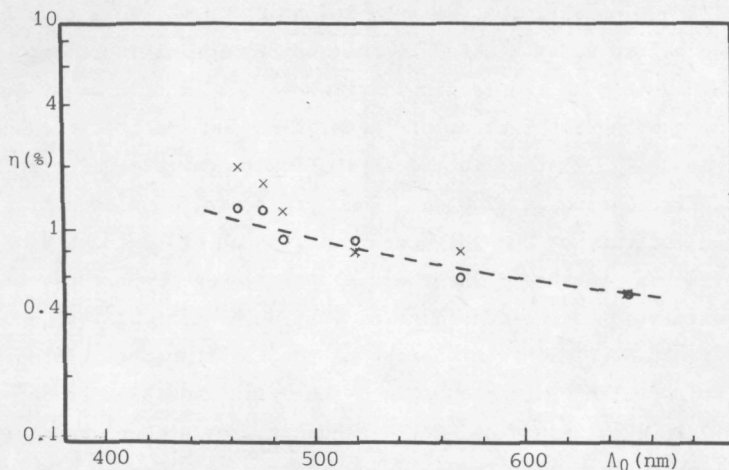


Fig. 3.17. Diffraction efficiency as a function of the light wavelength. Crosses and circles are experimental results (see text); the dashed line is calculated from Eq. (3.51).

III.5.2. Signal-to-noise ratio

In readout with a photothermoplastic film, the noise sources include³⁵:

1. The possibly existing frost deformation.
2. The nonlinearity of the recording and readout processes.
3. Light scattering by the materials composing the film.

Generally, the two first mentioned sources are the most significant³⁵.

Some considerations on frost deformation have been given in Sections II.2.4 and III.1.1. There are several possible means to suppress the formation of the frost bubbles. With regard to the choice of the thermoplastic polymer, Reich *et al.*³⁷ have suggested the use of a monocomponent thermoplastic to improve the signal-to-noise ratio because, according to them, frost deformation is caused by a phase separation phenomenon encountered only in multicomponent materials (this mechanism will be discussed in Chapter IV).

With respect to the dependence of the thermoplastic thickness, it has been found empirically⁸² that the amplitude of the frost bubbles diminishes rapidly as the thermoplastic layer is thinner than 1 μm , such that 0.5 μm is the lower thickness limit for the appearance of frost deformation. A similar conclusion has been also suggested by Matthies *et al.*⁸³

Using the simultaneous method of recording, Credelle and Spong¹³ have recorded holograms on films having a 0.2 μm thick thermoplastic layer; those

yielded a high diffraction efficiency with a low noise level. This high signal-to-noise ratio can partly be attributed to the suppression of frost deformation due to the relatively thin thermoplastic layer. The reduction of frost noise, however, is one of the characteristics of the simultaneous method, because in this method, cf. Sec. II.5.2, the light distribution to be recorded continues to illuminate the film during development. Then, this distribution still determines the conductivity of the photoconductor, which at the same time affects the deformation process of the thermoplastic layer. Only those surface ripples which are related to the recorded information are stimulated. Hence, the quasi-random frost bubbles have less chance to grow than the information related surface relief. The frost reduction by the simultaneous method appears to be the more significant, since using the sequential method and approximately the same thermoplastic thickness, Credelle and Spong have observed a high noise level.

III.5.3. Nonlinearity

III.5.3.1. Nonlinearity of the recording process

The recording process involves the information transfer from the light distribution to the charge or potential distribution, and the deformation process of the thermoplastic layer. The relation between the charge induced at the thermoplastic-photoconductive interface and the light distribution is in general non-linear, see Sec. III.2. This charge causes an electric field variation in the thermoplastic layer, which in its turn exerts deforming forces via a quadratic relation (the force by an electric field is proportional to the square of the field strength).

On the other hand, the formation of the surface relief is also affected by the surface tension, viscosity, resistivity, development time, and temperature dependence of these parameters, governed by a set of complicated hydrodynamical expressions²³. Obviously, the tendency of the whole recording processes has a strongly non-linear character. From scanning electron micrographs^{28,84}, indeed it is observable that the typical surface profile of a holographic grating is not purely sinusoidal.

Certain linear approximations, however, can be established. According to Urbach and Meier⁸⁵, the deformation amplitude can be regarded to correspond linearly to the incident exposure energy as long as this amplitude remains smaller than one fourth of the thermoplastic thickness (upon examination of Fig. 4 in a later paper by Urbach⁴⁰, the linearity is better assured if this limit is one tenth of the layer thickness). But even if such a direct

proportionality is achieved, the readout can contain traces of nonlinearity, due to the nature of a phase material considered in the next Sub-section.

III.5.3.2. Intrinsic nonlinearity of a phase material

The transmission function of a developed photothermoplastic film can be written as

$$\tau_{fv}(x, z) = \exp i[\phi_c + 2\pi(n_1 - 1)u(x, z)/\Lambda_0] \quad , \quad (3.52)$$

where ϕ_c is the constant part of the phase change introduced by the film, and $u(x, z)$ is the surface corrugation. We consider the variational part of the transmission function which, when expanded in a power series, obtains the form

$$\tau_{fv}(x, z) = 1 + i\phi_v(x, z) - \phi_v^2(x, z)/2 - i\phi_v^3(x, z)/6 + \phi_v^4(x, z)/24 + \dots \quad , \quad (3.53)$$

where $\phi_v(x, z) = 2\pi(n_1 - 1)u(x, z)/\Lambda_0$.

Depending on the magnitude of $\phi_v(x, z)$, the number of terms in the expansion to be taken into account can be reduced. For instance, for $n_1 = 1.6$ and $u(x, z) \leq 0.08\Lambda_0$ and asking an accuracy of only 5%, the rest of the real part can be ignored with respect to unity, and the rest of the imaginary part with respect to $i\phi_v(x, z)$. Then, we obtain the following linear relation

$$\tau_{fv}(x, z) = 1 + i[1.2\pi u(x, z)/\Lambda_0] \quad . \quad (3.54)$$

The chosen limit of $0.08\Lambda_0$ for the surface corrugation is somewhat severe, since for a sinusoidal thin phase grating, it yields a diffraction efficiency not higher than 2.3%. Urbach and Meier⁸⁵ have suggested a wider limit, in which the phase variation may have a maximal value of $\phi_v = 0.6$ rad, i.e. $u(x, z) \leq 0.16\Lambda_0$, such that an efficiency of 8.2% can be achieved [accuracy of the linear approximation, Eq. (3.54), is then equal to 18%]. Killat and Terrell⁸⁴ observed 10% diffraction efficiency as the limit for an approximately linear readout [accuracy of Eq. (3.54) is then 22%].

III.5.3.3. Effects of the nonlinearity

If nonlinearities are unavoidable, a certain degradation can be observed in the image formation. For a hologram of a diffuse object (having sharply defined boundaries), the reconstructed image will be smeared⁸⁶, while an object consisting of several bright points or lines will be accompanied in the readout

by other, sets of false points or lines which constitute the ghost images⁸⁶. We remark that these phenomena, reducing the signal-to-noise ratio, are dependent of the nature of the object. For instance, the first order reconstructed wave can be still a faithful reproduction of the object wave even if the recording is deliberately nonlinear (an extreme example: with a binary transmission function), provided that the object has a much lower spatial frequency than that of the hologram fringes⁸⁷.

As, for measuring the degree of the nonlinearity, we have utilized an object composed of two (long) illuminated slits, we shall show how the ghost slits will appear in the same position as the first order reconstructed image.

For simplicity, let us consider an object consisting of two infinitely long illuminated slits at (x_s, y_s) and $(-x_s, y_s)$, see Fig. (3.18); the thermo-plastic surface being located in the plane $y = 0$.

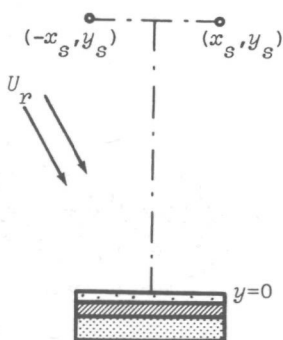


Fig. 3.18. On the consideration of the appearance of ghost images.

Applying Fresnel's approximation⁸⁹ of a cylindrical wave, the object wave function at $y = 0$ can be written as

$$\begin{aligned}
 U_o &= \text{const.} \{ \exp [i\kappa (x - x_s)^2 / 2y_s] + \exp [i\kappa (x + x_s)^2 / 2y_s] \} \equiv \\
 &\equiv |U_o| \exp i\phi_o(x, z) \quad , \quad (3.55)
 \end{aligned}$$

where $\phi_o(x, z)$ represents the phase of the object wave (at the film plane), which also contains the location of the origin of this wave. Let also a reference wave be incident on the film, which at $y = 0$ can be described by

$$U_r = |U_r| \exp i\phi_r(x, z) \quad . \quad (3.56)$$

The intensity absorbed by the film is given by

$$I_{abs} = f_1 |U_r|^2 + f_2 |U_o|^2 + f_3 U_r^* U_o + f_4 U_r U_o^* \quad (3.57)$$

where the absorption and the effects of the obliqueness of the interference planes (see Sec. III.2) are supposed to be included in the factors f_1 , f_2 , f_3 , and f_4 .

Furthermore we assume that, after development, the amplitude transmission factor is a nonlinear function of I_{abs} :

$$\tau_f = 1 + g_1 I_{abs} + g_2 I_{abs}^2 + g_3 I_{abs}^3 + \dots \quad (3.58)$$

The third term involves the square of the intensity which, from Eq. (3.57), is equal to

$$\begin{aligned} I_{abs} = & f_1^2 |U_r|^4 + f_2^2 |U_o|^4 + f_3^2 U_r^{*2} U_o^2 + f_4^2 U_r^2 U_o^{*2} + \\ & + 2 f_1 f_2 |U_r|^2 |U_o|^2 + 2 f_1 f_3 |U_r|^2 U_r^* U_o + 2 f_1 f_4 |U_r|^2 U_r U_o^* + \\ & + 2 f_2 f_3 |U_o|^2 U_r^* U_o + 2 f_2 f_4 |U_o|^2 U_r U_o^* + 2 f_3 f_4 |U_r|^2 |U_o|^2. \end{aligned} \quad (3.59)$$

Let the hologram be illuminated with a reconstruction beam identical to the reference wave. Then, apart from a constant factor, the contribution from the second order intensity term is, with Eqs. (3.57) and (3.59), given by

$$\begin{aligned} I_{abs}^2 U_r = & f_1^2 |U_r|^5 \exp i\phi_r + f_2^2 |U_r| |U_o|^4 \exp i\phi_r + \\ & + f_3^2 |U_r|^3 |U_o|^2 \exp i(-\phi_r + 2\phi_o) + f_4^2 |U_r|^3 |U_o|^2 \times \\ & \times \exp i(3\phi_r - 2\phi_o) + 2(f_1 f_2 + f_3 f_4) |U_r|^3 |U_o|^2 \exp i\phi_r + \\ & + 2 f_1 f_3 |U_r|^4 |U_o| \exp i\phi_o + 2 f_1 f_4 |U_r|^4 |U_o| \exp i(2\phi_r - \phi_o) + \\ & + 2 f_2 f_3 |U_r|^2 |U_o|^3 \exp i\phi_o + 2 f_2 f_4 |U_r|^2 |U_o|^3 \exp i(2\phi_r - \phi_o). \end{aligned} \quad (3.60)$$

We are only interested in the terms which have the same phase ϕ_o as the object wave, because they propagate in the exactly same direction as the first order reconstructed wave (we assume that the recording configuration is such that $\phi_r \neq \phi_o$, so that $-\phi_r + 2\phi_o \neq \phi_o$, $3\phi_r - 2\phi_o \neq \phi_o$, and $2\phi_r - \phi_o \neq \phi_o$). The

first of these, $2f_1 f_3 |U_p|^4 |U_o| \exp i\phi_o$, apart from the fourth power of the amplitude of U_p , yields the image of the object faithfully.

We consider the second of these terms, $2f_2 f_3 |U_p|^2 |U_o|^3 \exp i\phi_o$, which is proportional to

$$|U_o|^2 U_o = [2 + \exp(-i\kappa 2x_s/y_s) + \exp(i\kappa 2x_s/y_s) \times \\ \times \{\exp[i\kappa(x - x_s)^2/2y_s] + \exp[i\kappa(x + x_s)^2/2y_s]\}] \quad (3.61)$$

When this expression has been worked out we obtain

$$|U_o|^2 U_o = 3 \{\exp[i\kappa(x - x_s)^2/2y_s] + \exp[i\kappa(x + x_s)^2/2y_s]\} + \\ + \exp(-i\kappa 4x_s^2/y_s) \{\exp[i\kappa(x - 3x_s)^2/2y_s] + \\ + \exp[i\kappa(x + 3x_s)^2/2y_s]\} \quad (3.62)$$

The first term at the right-hand side is just a reproduction of the object wave. The second term, however, represents a wave that would have been emanated from two slits at $(3x_s, y_s)$ and $(-3x_s, y_s)$. Hence, it is the wave causing the appearance of a ghost image. The distance from each ghost slit to the nearest true slit image is equal to the separation of the slit objects ($= 2x_s$).

In a similar way it can be shown that the third-order intensity term in Eq. (3.58) yields, apart from the true reconstructed wave and the wave causing ghost images at $(3x_s, y_s)$ and $(-3x_s, y_s)$, also a wave that seems to originate from $(5x_s, y_s)$ and $(-5x_s, y_s)$. The fourth order term describes in addition a wave from $(7x_s, y_s)$ and $(-7x_s, y_s)$, and so on.

The appearance of the ghost images can be disastrous in application such as binary data storage^{89,90}, since then a signal seems to be generated in a place that ought to be dark.

III.5.4. Some measurements of the signal-to-noise ratio and the linearity

In order to measure the signal-to-noise ratio, we utilized as the object a 5×5 cm² diffuse glass plate, whose central part was covered with an opaque stripe 1.25 cm wide, see Fig. 3.19. In the reconstruction, we measured the intensity ratio between the bright and the dark parts of the real image and defined it as the signal-to-noise ratio of our film (S/N). A similar method

has been also employed by other authors^{35,37,91}, although the exact size and form of the objects were different (a standardization has not been established). An example of our reconstructed image is shown in Fig. 3.20.

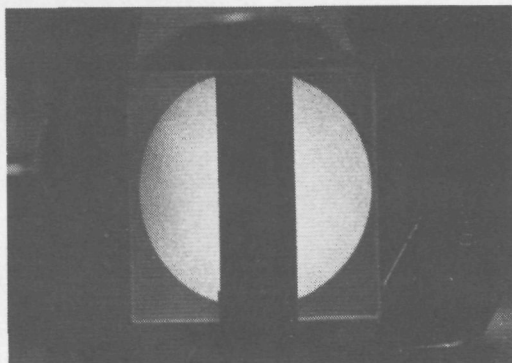


Fig. 3.19. The object used to measured the signal-to-noise ratio.

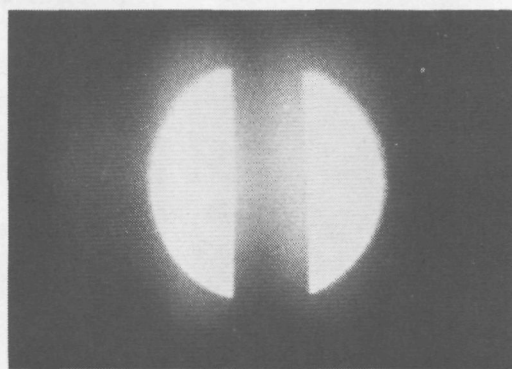


Fig. 3.20. A reconstructed image of the object.

To measure the degree of the film linearity, the greater part of the rest of our object is also covered, such that only two slits with a width of 2 mm each, separated at 12.5 mm distance, can pass the light. The intensity ratio between the brightest parts of the true slit image and the first (nearest) ghost image in the real reconstruction is then defined as the measure of the film linearity (*LIN*). This is because the more nonlinear the film would be (the more higher order intensity terms are leading to observable images), the more light contribution will be found in the first ghost image, compare our derivation and discussion in Subsection III.5.3.3.

Three examples of the reconstructed slits are given in Figs. 3.21, 3.22, and 3.23, with respectively $LIN = 180, 60, \text{ and } 30$. Due to the limited dynamic range of the photographic film used to record the images, the apparent brightness proportion at those photographs does not faithfully represent the

actual intensity ratio. We remark that, although the linearity measurement (like the signal-to-noise ratio) has not been standardized, our method is comparable to the "signal-to-ghost ratio" measurement by Goldmann⁸⁹.

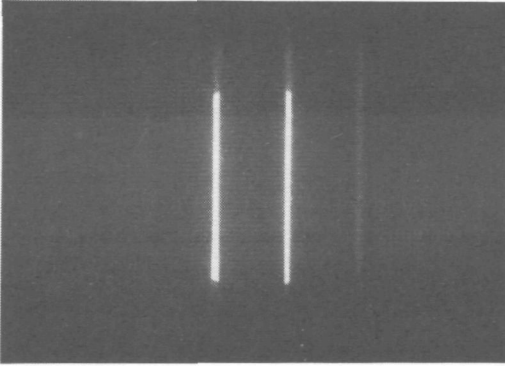


Fig. 3.21. Reconstructed image of the slits, LIN = 180.

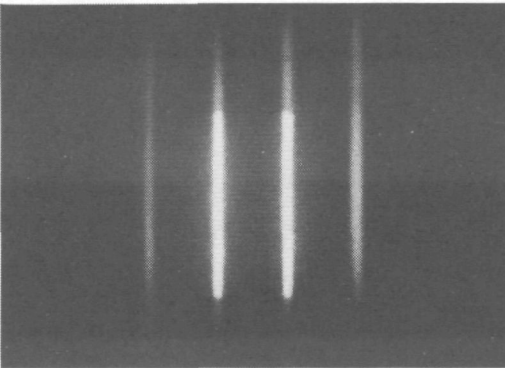


Fig. 3.22. LIN = 60.

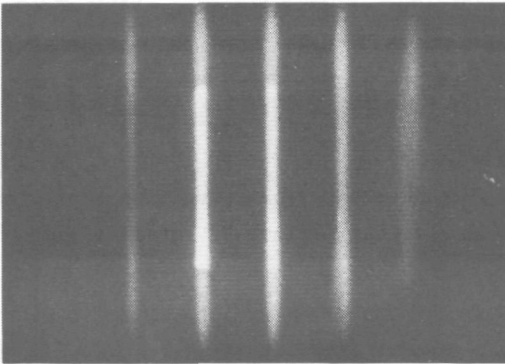


Fig. 3.23. LIN = 30.

The results of our measurements are depicted in Fig. 3.24 through Fig. 3.27. In these graphs, the diffraction efficiency η is from a holographic

grating. All measurements (η , S/N , and LIN) were obtained from holograms, recorded in green light ($\Lambda_0 = 521$ nm) with optimal parameters, except for the parameter acting as the abscissa in each graph. For instance, in Fig. 3.24, the exposure is $85 \mu\text{J}/\text{cm}^2$ (cf. Fig. 3.25), the spatial frequency 750 lp/mm, the corona voltage 12 kV and the intensity ratio of the reference to the object waves is 1 : 1.

If we assume that nonlinearity and frost deformation are the only sources of noise, the difference between the LIN and S/N curves gives the measure of the contribution from frost in disturbing the reconstruction.

In Fig. 3.24, S/N and LIN have a relatively high value in the range just below the optimal development energy. Apart from the inherently low linearity at high diffraction efficiencies, see Sec. III.5.3, the cause there is presumably that the thermoplastic material is fairly stiff and its resistivity rather high, such that the potential distribution is still reasonably proportional to the exposure. At higher development energies, however, the layer is softer and the resistivity lower; the charge on the thermoplastic surface leaks partially away or displaces itself into the soft layer, thus disturbs the original potential distribution and increases the nonlinearity. The increase of the frost contribution at higher development energies (see the difference between LIN and S/N) agrees with the observations by Lee⁹².

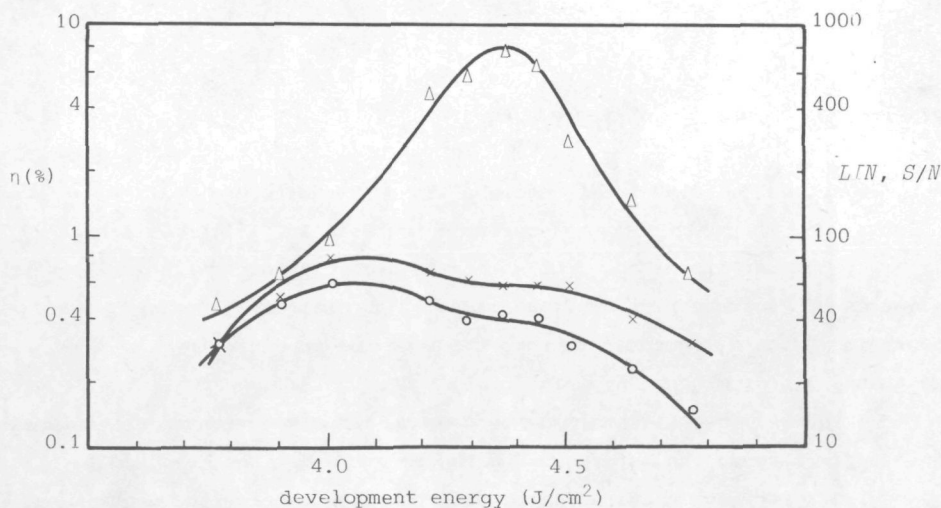


Fig. 3.24. Diffraction efficiency (Δ), linearity (\times) and signal-to-noise ratio (\circ) as a function of the development energy.

In Fig. 3.25, the results are shown as a function of the exposure energy. It is seen that a good linearity is obtained in the low exposure range, confirming our discussion in Sec. III.2.2. Frost deformation, however, becomes the most significant in that low exposure region. The cause is the relatively weak modulation in the potential distribution in the case of a low exposure, see Sec. III.2.3, such that the fairly homogeneous surface potential gives the frost more chance to grow.

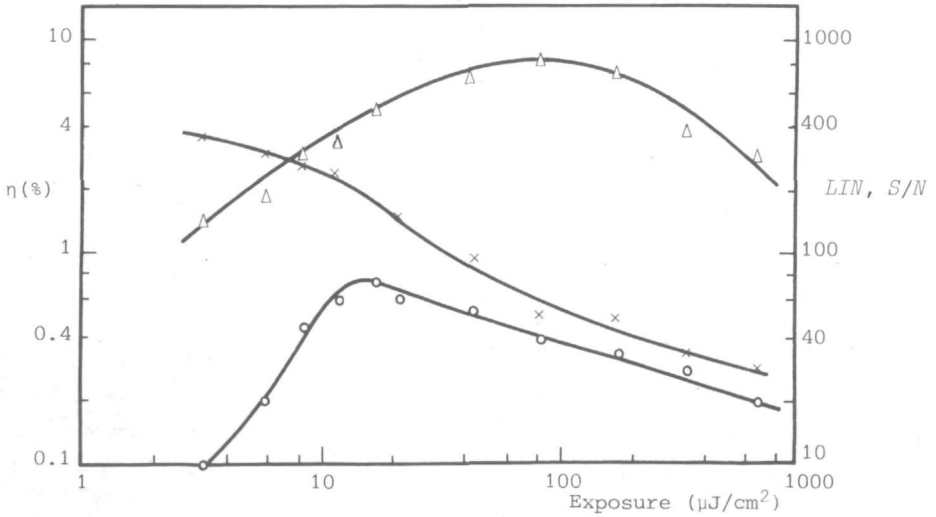


Fig. 3.25. Diffraction efficiency (Δ), linearity (\times) and signal-to-noise ratio (o) as a function of the exposure energy.

The increase of the frost contribution with the corona voltage ϕ_c is seen in Fig. 3.26. This confirms the conclusion in Sec. III.1.1, that a high surface potential (to be acquired with a high corona voltage) stimulates the formation of frost bubbles. The magnitude of the increase, however, is surprisingly low as compared to the effect of the exposure in Fig. 3.25, and to the effect of the intensity ratio in Fig. 3.27.

In Fig. 3.27, η , LIN and S/N are depicted as a function of the intensity ratio I_r/I_o between the reference and the object waves. As it could be expected, the nonlinearity becomes more severe when the object beam (the signal) is stronger than the reference beam (the bias), see part of the LIN curve to the left of $I_r/I_o = 1$.

If the ratio I_r/I_o is far from unity, the resulting modulation in the intensity distribution is small, and the initially uniform surface potential

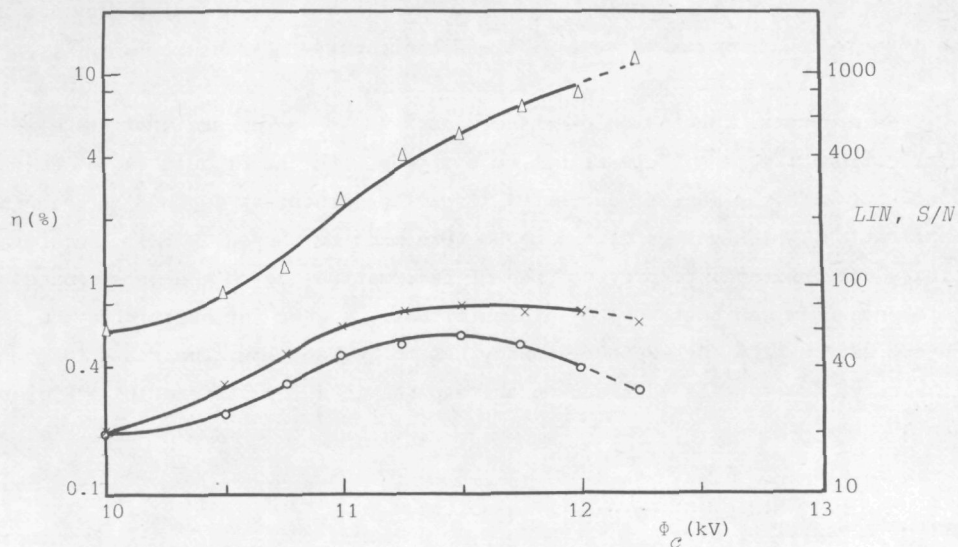


Fig. 3.26. Diffraction efficiency (Δ), linearity (\times) and signal-to-noise ratio (\circ) as a function of the corona voltage.

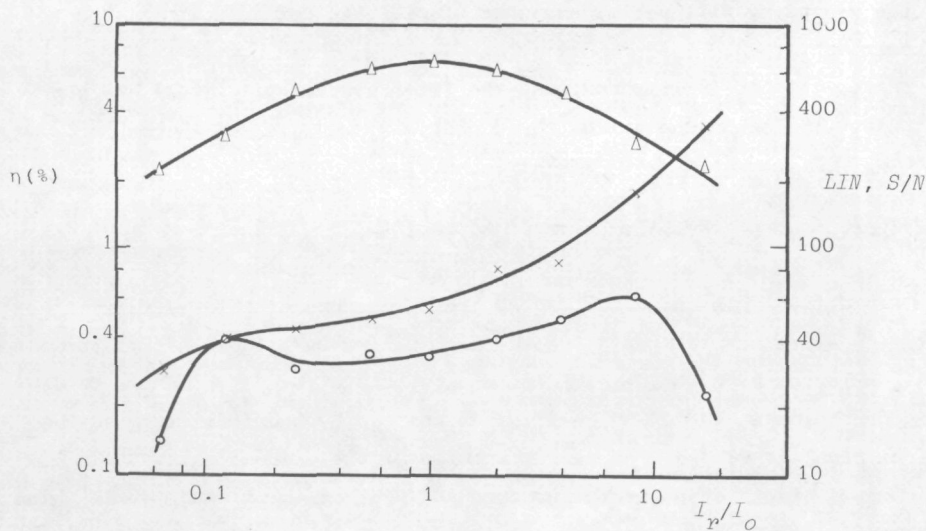


Fig. 3.27. Diffraction efficiency (Δ), linearity (\times) and signal-to-noise ratio (\circ) as a function of the intensity ratio between the reference and the object beams.

does not change significantly. Then, the frost bubbles can easily grow, as can be interpreted from the extreme left and right parts of the graph.

As a general conclusion of these measurements we remark, that the maximal diffraction efficiency appears not to coincide with the highest signal-to-noise ratio nor with the maximal degree of linearity. Hence, it depends on the aimed application, which values of the parameters must be chosen. For instance, for binary data storage, to prevent loss of information due to the ghost image, the reference beam can better be of a significantly higher intensity than the object beam, while the exposure energy has to be kept low. The resulting good linearity, however, is obtained on the expense of a low diffraction efficiency.

III.6. Reusability

Theoretically, a photothermoplastic film can be reused indefinitely if the previously recorded information is erased. The thermal erasure process should occur at a higher temperature than the development temperature, such that the conductivity will be raised sufficiently to let all charges leak away and such that the viscosity will be low enough to facilitate reflattening of the thickness variation.

The actual possibility to reuse the film, however, is limited by the effects considered in the following account.

III.6.1. Fatigue of the thermoplastic material

The fatigue⁹³ is characterized by the occurrence of a lower diffraction efficiency after several reuse cycles, accompanied by a lower signal-to-noise ratio, an increase in the development energy, and a reduction in the resolution. This degradation is caused by physical as well as by chemical changes. The physical change includes gradual destruction of the thermoplastic layer (creation of tiny craters at the surface and sputtering of the material) due to ion bombardment. This increases the scattering of light and, moreover, after many reuse cycles that much material is sputtered away that the diffraction efficiency is affected³⁵.

The chemical change, such as oxidation of the thermoplastic material, is induced by the repeated heat treatment and by the ozone generated in the corona discharge. Two other forms of the chemical change have been considered in

Sec. II.1.4, viz., scission and cross-linking of the thermoplastic polymer.

Generally, the use of a somewhat low corona voltage helps to reduce both the physical and chemical degradations, although then the diffraction efficiency will be low. To prevent chemical changes, the recording processes can be carried out in an atmosphere of nitrogen or some inert gas such as argon^{25,93}. In this way, up to 80000 record-erase cycles have been reported by Lo *et al.*⁹³

Another possible measure is to employ a thermoplastic polymer in which the scission tendency competes with the cross-linking tendency, see Sec. II.1.4. The use of a material, capable of resisting the ozone attack, has also been investigated. Colburn and Tompkins³⁵ utilized a vinyl-toluene copolymer thermoplastic having this property, and succeeded to carry out 3000 record-erase cycles practically without degradation, although compared to other recordings produced by their system, the diffraction efficiency from this thermoplastic is low (1%).

III.6.2. Residual image

This refers to the previously erased recordings which reappear in the subsequent recording, thus reducing the signal-to-noise ratio (this image has been named "ghost image" by several authors, but to prevent confusion we prefer to use this latter term only for the false images caused by nonlinearities). The origin of residual image can be found in the thermoplastic and photoconductive layers.

With regard to the thermoplastic layer, the residual image is caused by surface relief that has been not completely erased. Its existence appears to be strongly dependent of the used thermoplastic. With Staybelite Ester 10, three or four current pulses (compared to one for the development) have to be applied^{56,94} in order to erase the recorded information effectively. Lee⁵⁶, using other thermoplastic polymers, had no residual image problem at all after several thousands of reuse cycles.

The residual image arises also partly from the photoconductive layer, caused by the remanent distribution of the charge carriers which are left behind⁹⁵.

In fact, when the thermoplastic sheet of a recording is washed out (dissolved) and a fresh one is deposited, the image of that old recording can still appear when the film is charged and developed²³. DuBow and Colburn⁹⁵ attributed this effect to the low electron mobility of the PVK-TNF photoconductor at the commonly used molar ratio (low TNF fraction). The electrons,

drifting very slowly, are partly left behind in the layer after development and erasure, while the holes have disappeared due to movement and recombination at the conductive layer. Then, the field of these remaining electrons introduces the residual information in the subsequent recording process.

Several means have been suggested to minimize the formation of this remanent field⁹⁶. One of these is increasing the TNF concentration, making the electron mobility higher (giving the electrons less chance to leave behind). The mobilities of holes and electrons also increase with temperature, so that for a given composition of the photoconductor, higher development and erasure temperatures can help to suppress the residual image. Another possible method is illuminating the film with white light before the actual erasure to remove the remaining charge carriers.

Although the residual image may become a persistent problem in many applications, it can be helpful in at least one application, i.e. the double exposure technique in holographic interferometry. Here, after the first exposure, the film is developed and then the processes for the subsequent recording are performed. During the second development, the first recording is partially erased and reappears in readout together with the second information, thus yielding the desired superimposed images. The recording method can be sequential³⁴ as well as simultaneous⁹⁷. This technique is preferred above performing two exposures successively before development, because this last method leads to more noise in readout^{34,97}.

We remark that the readout only yields the sum of the two exposures faithfully (recorded successively before development) if the total exposure energy is very low, see Sec. III.2.2. Otherwise, the nonlinear behaviour of the photoconductor will introduce false contributions (noise) in the readout. The low exposure energy, however, yields a low diffraction efficiency. Hence, the utilization of the residual image is a favourable way indeed to accomplish the double exposure technique.

III.6.3. Contamination of the thermoplastic surface

Another noise source in the repeated use of the film is caused by dust and dirt particles collected at the thermoplastic surface. This surface is usually tacky, and small particles can easily adhere to it, especially during (and shortly after) the recording stages, due to electrostatic attraction by the deposited charges (or their residues) at that surface. If the direct vicinity of the film is not dust free, the collected particles will increase light

scattering, while part of them penetrate the thermoplastic layer (during softening) and will introduce inhomogeneities that disturb the deforming forces and, still more disastrously, they can stimulate an electric breakdown.

We have carried out some experiments on the reusability of our film, although it is actually not intended for erasure and reuse⁹⁸. Two varieties of the film were considered. The first, coded as PT-1000, is the film used to obtain the experimental results⁹⁹ in Chapter II and III (except the results depicted in Figs. 3.1, 3.3, 3.4, 3.5, which are obtained with the second film type), and has an optimal exposure of about $85 \mu\text{J}/\text{cm}^2$, cf. Fig. 3.25.

The second is a new type, PT-1000S, having an optimal exposure of about $1 \mu\text{J}/\text{cm}^2$, and is employed in the rest of the experiments considered in this work. We have found that it is not possible to reuse the PT-1000S, viz., after a complete erasure of the previous recording, we can not make a recording at all on the same area, even if the development energy has been raised by a factor 50% of its original (optimal) value. The cause is presumably a complete and permanent chemical change, since we found that the film then became less flexible and the light scattering increased significantly.

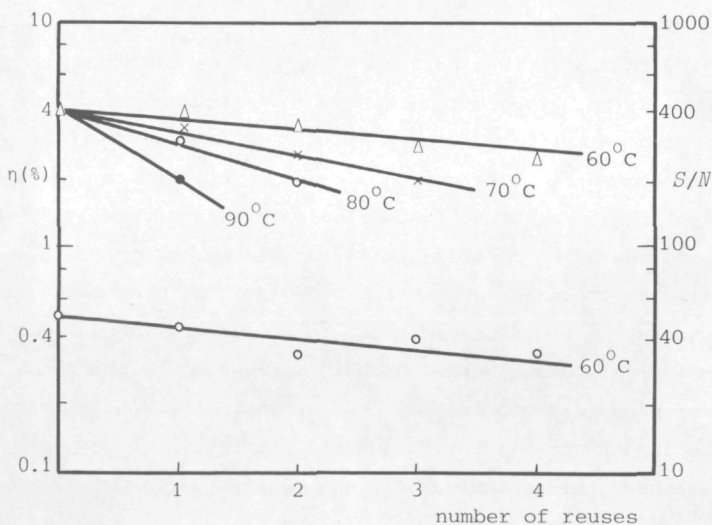


Fig. 3.28. Diffraction efficiencies (upper curves) and signal-to-noise ratio (lower curve) as a function of the number of record-erase cycles.

In Fig. 3.28 we depict the results with the type PT-1000. We have placed a certain length of the film with the recordings on it into an oven for 20 minutes

at several temperatures. The lowest temperature for erasure turned out to be 60°C . It is also the most favourable value, since at higher temperatures the chemical degradation will be stimulated (as can be seen from Fig. 3.28).

III.7. The role of the thermoplastic thickness

Apart from influences from other recording parameters (such as the surface potential), it is primarily the thickness of the thermoplastic layer that determines the predominant wavelength of frost deformation, the optimal spatial wavelength of a recording, and less significantly, the spatial bandwidth of the recording.

Budd⁴¹ has suggested a theory for frost deformation from which it follows that the predominant wavelength is approximately equal to twice the thermoplastic thickness. Some investigators^{15,32} found that the optimal wavelength of their holograms did not agree with the value predicted by Budd's theory. Although this theory has been revised later by Killat²⁴ (both theories are of the dynamic type, cf. Chapter IV) and supplemented with our quasi-static theory presented in Chapter IV, the discrepancies observed by those investigators are not surprising.

This is because the conditions corresponding to frost deformation are different from those in holographic recordings. In frost theories, the potential (or charge density) of the thermoplastic surface prior to the heating is assumed to be homogeneous. In holographic recordings, however, the potential (or charge density) is always a function of the coordinates parallel to the film surface (according to the recorded intensity distribution).

Moreover, only the thickness of the thermoplastic has been taken into account in the theories of frost deformation. In holograms, the deforming forces follow from a field distribution that is influenced by the photo-induced charge at the thermoplastic-photoconductive interface. The photoconductor thickness plays an important role in the generation of this charge (see Sec. III.2), hence, this thickness can not be ignored in determining the response of a holographic recording.

The thickness \bar{h} of the thermoplastic sheet affects the spatial bandwidth (BW) of the film response, too, (the bandwidth is defined as the difference between spatial frequencies where the diffraction efficiency has dropped to 0.5 its maximal value). Urbach and Meier⁸⁵ observed that this bandwidth can be approximated by $(6\bar{h})^{-1}$. Later, it has been reported²³ that a value range between $(6\bar{h})^{-1}$ and $(4\bar{h}/3)^{-1}$ is a better approximation.

We have gathered experimental results from various authors^{13,15,22,23,28,32,60,100,101} concerning the relations of the optimal spatial wavelength λ_{op} and the reciprocity of the bandwidth $(BW)^{-1}$ to the thermoplastic thickness h . Since those relations appear to depend also on the recording method, we distinguish in Fig. 3.29 the results from the sequential method (open circles) and the simultaneous method (dots).

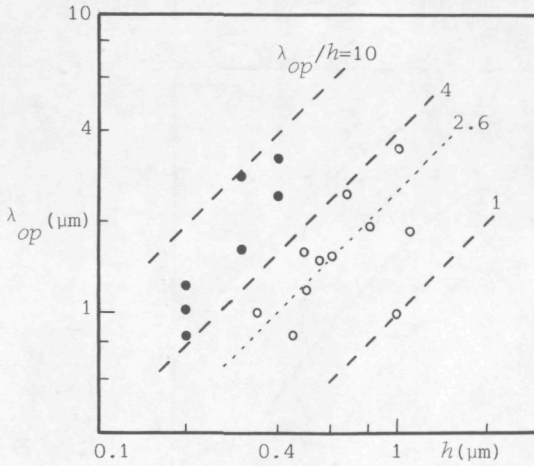


Fig. 3.29. Experimental results of various authors:
a. The optimal spatial wavelength as a function of the thermoplastic thickness;

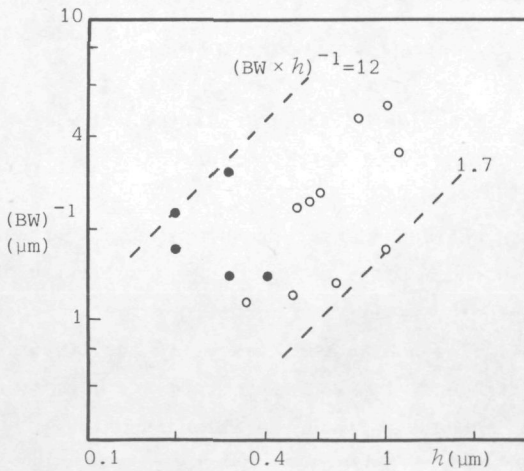


Fig. 3.29.b. The reciprocity of the bandwidth as a function of the thermoplastic thickness.

It is seen that the ratio λ_{op}/h in the sequential method tends to be lower than in the simultaneous method. Roughly, the ratio in the first method is between 1 and 4, while in the simultaneous method it is between 4 and 10. Such a distinction is more difficult to observe in the bandwidth values; the

boundaries, however, are about $(12h)^{-1}$ and $(1.7h)^{-1}$.

In fact, the bandwidth appears to be strongly susceptible to changes in the recording parameters. Some examples are given in Figs. 3.2 and 3.30, where the spatial frequency response of our film is depicted as a function of one of the parameters. For comparison, the upper curve is obtained with all parameters at their optimal values, cf. Sec. III.5.4. It is seen that the bandwidth tends to be narrower when one of the parameters is below its optimal value.

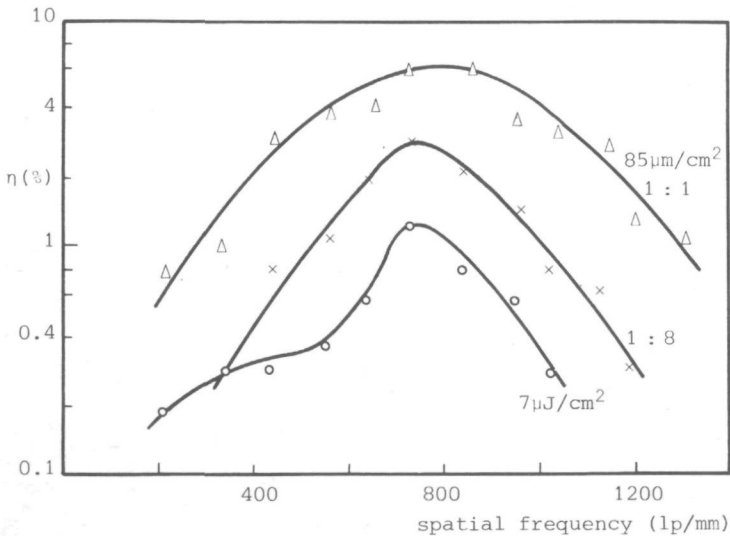


Fig. 3.30. Diffraction efficiency as a function of the spatial frequency, for different values of the exposure energy and the intensity ratio.

In principle, one can have a high optimal spatial frequency (low λ_{op}) as well as a broad BW by selecting a thin thermoplastic layer. The lower limit of h depends on the needed η , since a thin layer will not permit a large deformation amplitude, hence will not allow a high efficiency. If the linearity between exposure and deformation amplitude a_p is also taken into account, a more severe limitation is introduced, because a linear relation is only assured⁸⁵ for $a_p \leq 0.25h$ (or even better⁴⁰, $a_p \leq 0.1h$).

Let, as an example, a maximal η of 30% at $\Lambda_0 = 0.633 \text{ nm}$ be a requirement. Then, from the formula for a sinusoidal grating, Eq. (3.51), with $n_1 = 1.6$, a_p should have a value of $0.24 \mu\text{m}$. If the linearity condition $a_p \leq 0.25h$ is applied, the thermoplastic layer must be at least $0.96 \mu\text{m}$ thick. But such a thickness yields in the sequential method an optimal spatial frequency of only 400 lp/mm (if we use the representative ratio $\lambda_{op}/h = 2.6$, see Fig. 3.29.a).

In practice, some compromise is made between the diffraction efficiency

and the linearity. If we take a value $\eta = 10\%$, cf. Sec. III.5.3, maintaining the linearity requirements between α_p and exposure, we obtain $h = 0.46 \mu\text{m}$, yielding a maximal response at about 830 lp/mm in the sequential method. This thickness value lies also in the range ($\approx 0.5 \mu\text{m}$ or less) within which the growth of frost deformation is less significant, see Sec. III.5.2. Hence, from these considerations, a thermoplastic thickness of about $0.5 \mu\text{m}$, such as employed in our film, is the optimal value.

IV. QUASISTATIC THEORY OF FROST DEFORMATION IN THERMOPLASTIC FILMS*

IV.1. Introduction

Since the first investigations^{22,102} on the thermoplastic films as an optical recording material, it has been observed that such a film gives a bandpass spatial frequency response (cf. Sec. II.2.4), with a peak at some central frequency. The spatial wavelength related to this central frequency, which is dependent of several variables^{15,28,32,56}, appears to be directly proportional to the thickness of the thermoplastic layer.

For the use of these films knowledge of this wavelength-thickness relation is important and several theoretical approaches^{24,41} have been formulated for the simplified case of frost deformation. These theoretical approaches apply as part of the efforts to ultimately explain the wavelength-thickness relation in a thermoplastic recording (the conditions and the process in such a recording are more complex than in the case with frost deformation, see Sec. III.7).

The frost deformation, which is caused by surface instabilities, occurs generally when a thermoplastic film, whose surfaces are initially charged to a uniform and sufficiently high potential difference, is heated to its softening temperature. The resulting surface corrugation shows a quasirandom bubble pattern having a predominant spatial wavelength (cf. Sec. II.2.4). Experimentally this predominant wavelength has been revealed (see Fig. 4.1) to be proportional to the thickness of the thermoplastic layer, the proportionality factor being roughly between unity and four.

According to Budd⁴¹, this wavelength is approximately equal to twice the thermoplastic thickness. His theory was revised by Killat²⁴, who concluded that the wavelength-thickness ratio should be approximately equal to 4. (In later work Killat and Terrel⁸⁴ found experimentally a factor of π for this ratio.)

Both theories^{24,41} are of the dynamic type, i.e., the surface perturbation

* This Chapter is a slightly modified version of a previously published paper¹¹.

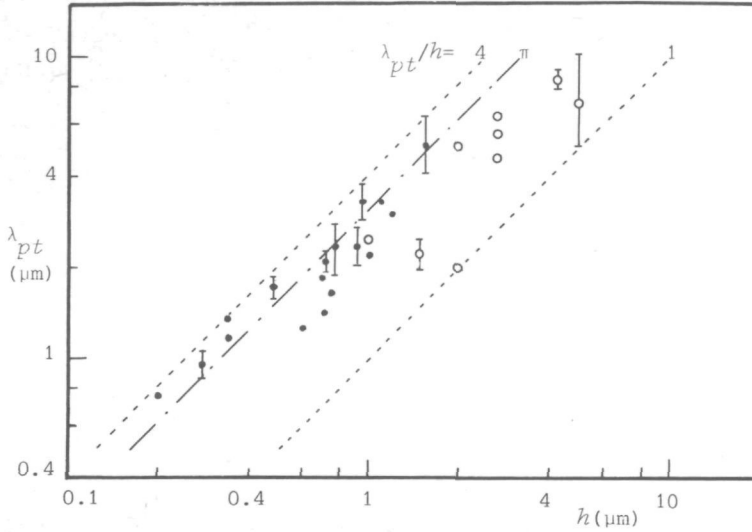


Fig. 4.1. The predominant spatial wavelength λ_{pt} of frost deformation as a function of the thickness h of the thermoplastic layer, based upon experimental results of various authors. The open circles were obtained with the heating stage performed separately after charging^{13,63,82,103,104,105}; the dots obtained with a continuous charging during heating^{24,84}.

is taken to depend on time, starting from an extremely small deformation. The predominant wavelength is deduced from the growth tendency of this deformation, considering only the initial electric potential distribution. A crucial fact, however, is that this distribution will change during the process because of the increasing deformation. The growth tendency, depending on the potential distribution, will therefore vary during the deformation process.

In the present Chapter we explain the predominant wavelength-thickness relation using a quasistatic approach. Its principles will be considered in Sec. IV.2. In Sec. IV.3 the electric potential distribution in a deformed layer is derived, using two models, viz., the equipotential and the non-equipotential models. The wavelength-thickness relation is then calculated in Sec. IV.4 and compared to the experimental results from other authors. This Chapter is concluded in Sec. IV.5 by a discussion of the results and the frost mechanism suggested by other authors.

IV.2. Theory

IV.2.1. Equilibrium condition

We consider a film consisting of three layers: a substrate and a thermoplastic layer, with a conductive material in between. With the conductive layer at ground potential, the upper surface of the thermoplastic is initially charged uniformly, and the film is heat softened. Then, noiselike microscopic bubbles on the thermoplastic surface will grow under the influence of electric forces and the surface tension. Rather than following the course of this process, we consider its final state, occurring when the deforming forces have come to an equilibrium. We assume the heating time to be long enough to reach this state. Then, the pressure p in the deformed, but still soft, thermoplastic layer obeys the relation

$$\vec{\nabla} p = \vec{0} \quad . \quad (4.1)$$

At a frosted surface (see e.g. Fig. 2.5), the bubbles show locally a tendency to be elongated in a certain direction. In a small area containing a few bubbles we may thus approximate the final deformation by a system of parallel wrinkles. Such a system is depicted in Fig. 4.2, where x , y , and z are the local Cartesian coordinates, the xz plane coincides with the surface before the deformation, and the x axis is perpendicular to the wrinkles. The wrinkle pattern is assumed to have a sinusoidal cross section (in the xy plane)*, so that the final surface deformation $u(x)$ at the xy plane can be written as

$$u(x) = a \cos(kx + \psi) \quad , \quad (4.2)$$

where a denotes the deformation amplitude, while $\lambda = 2\pi/k$ is the spatial wavelength of the deformation. The origin is chosen such that the phase term ψ vanishes; see Fig. 4.2. We need to determine the combination of values of a and k that satisfies the equilibrium condition. For this purpose we consider the forces across the interface at the extremes of the deformation, see Fig. 4.3. In this figure, p_{el} denotes the pressure produced by the electric field and γ the effective value of the surface tension (the influence of the

* In case of a deviation from a pure sinusoidal form, representation by a Fourier integral can be used.

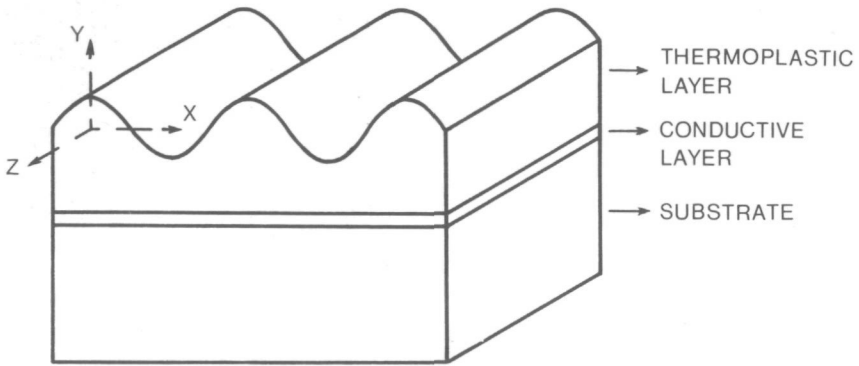


Fig. 4.2. Frost deformation, considered as a system of parallel wrinkles.

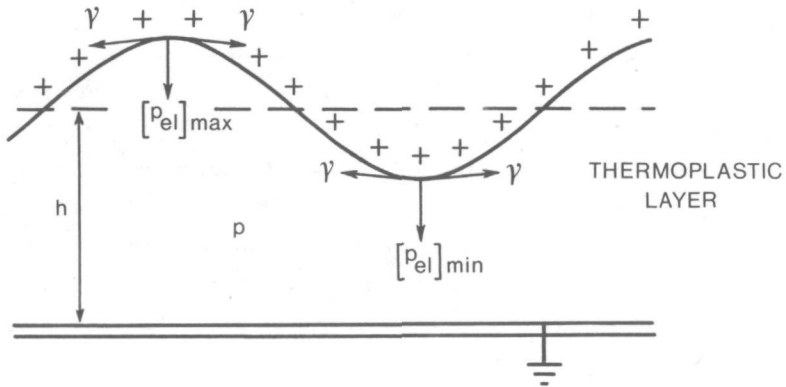


Fig. 4.3. The pressures in the equilibrium state; h is the thickness of the thermoplastic layer before deformation.

electric field on γ will be considered in Sec. IV.2.2). For a cylindrically curved interface, the excess pressure is equal to γ/r , where r is the radius of curvature of this interface¹⁰⁶. The pressure p at the interface can then be written as

$$p = (p_{el} - \gamma/r)_{max, min} \quad (4.3)$$

where the subscripts max, min refer to the extremes of the surface

deformation $u(x)$. We have ignored the influence of gravity since in practice it is negligible compared to the effects of the electric field. Using $r = [1 + (du/dx)^2]^{3/2} / (d^2u/dx^2)$, and Eq. (4.2) we obtain $r_{min} = 1/ak^2$ and $r_{max} = -1/ak^2$. Since the equilibrium pressure is homogeneous throughout the deformed layer [see Eq. (4.1)], we obtain from Eq. (4.3)

$$(p_{el})_{min} - (p_{el})_{max} = ak^2(\gamma_{max} + \gamma_{min}) \quad (4.4)$$

The quantities p_{el} and γ will further be expressed in terms of the surface charge density σ and the surface potential ϕ_s .

IV.2.2. Surface tension

Schmid *et al.*¹⁰⁷ and Hayes¹⁰⁸ have studied the influence of an electric field on the surface tension of NaCl-water solutions. Expressions for the surface tension of a thermoplastic film have been derived^{41,61} by consideration of infinitesimal surface perturbations. In the following we present a derivation not necessarily restricted to small deformations.

We consider a subvolume ΔV of the softened layer carrying a charge ΔQ on its upper surface ΔA (Fig. 4.4). The infinitesimal work dG needed to enlarge this area to $\Delta A + dA$ is equal to (cf. Adam¹⁰⁹)

$$dG = \gamma dA + \phi_s dQ \quad (4.5)$$

where dQ is the change of the charge due to the enlargement of the thermoplastic surface and ϕ_s is the surface potential.

In Eq. (4.5) we have assumed that the process is isothermal and isobaric; these assumptions are usually valid as the process is carried out at the softening temperature and in an unbounded air environment. Moreover, the number of thermoplastic molecules in ΔV is taken constant, which is true if we can avoid chemical reactions. Otherwise, we should add to the right-hand side the terms $-S dT + \Delta V dp + \mu dn$, where the symbols are well known from thermodynamics¹¹⁰. The first term on the right-hand side of Eq. (4.5) implies a completely plastic deformation since in case of an elastic deformation we would have to use^{111,112} $f dA$ instead of γdA , with $f = \gamma + \Delta A (\partial \gamma / \partial A)$. This plastic consideration can be justified if the process is sufficiently slow¹¹². With some mathematics¹⁰⁹ we then obtain from Eq. (4.5) the relation

$$\frac{d\gamma}{d\phi_s} = - \frac{\partial Q}{\partial A} \frac{d\text{ef}}{\text{def}} - \sigma \quad (4.6)$$

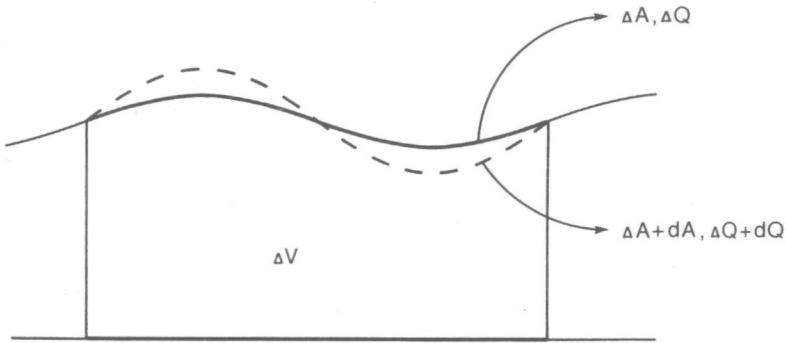


Fig. 4.4. On the derivation of Eq. (4.5): an area ΔA carrying a charge ΔQ is enlarged to $\Delta A + dA$.

IV.2.3. The pressure due to the electric field

Calculations involving the pressure due to an electric field have often been beset with ambiguities¹¹³. According to several textbooks¹¹⁴⁻¹¹⁶, the pressure gradient caused by an electric field within a dielectric liquid in the absence of space charges is given by

$$\vec{\nabla} p = -\frac{1}{2}\epsilon_0 E_1^2 \vec{\nabla} \epsilon_{r1} + \frac{1}{2}\epsilon_0 \vec{\nabla} [E_1^2 \rho (\partial \epsilon_{r1} / \partial \rho)] \quad (4.7)$$

where E_1 , ϵ_{r1} , and ρ denote the electric field strength, the relative permittivity, and the density of the liquid, respectively; ϵ_0 is the permittivity of vacuum. If we apply the integral form of Eq. (4.7) to the region around the interface, for an electric field perpendicular to the liquid's surface, the first term on the right-hand side leads to a pressure difference across the interface¹¹⁴ of

$$p^{(1)} = \frac{1}{2}\epsilon_0 (\epsilon_{r1} E_1^2 - \epsilon_{r2} E_2^2) \quad (4.8)$$

where ϵ_{r2} and E_2 are the relative permittivity and the electric field strength in the air, respectively. Killat²⁴ used a similar formula for the case of an

equipotential interface.

On the other hand, Hakim and Higham¹¹⁷ have experimentally proven that if a region within a dielectric liquid is exposed to an electric field, it experiences — with respect to parts without field influence — an extra pressure due to electrostriction:

$$p_{es} = \epsilon_0 E_1^2 (\epsilon_{r1} - 1) (\epsilon_{r1} + 2) / 6 \quad . \quad (4.9)$$

Since the pressure in the field-free region is usually equal to the atmospheric pressure, p_{es} plays a similar role to $p^{(1)}$ in Eq. (4.8). Gaynor and Aftergut⁴⁹ applied Eq. (4.9) for estimating a surface parameter of their thermoplastic recording.

Hence, at least two expressions have been used for the pressure difference across a thermoplastic surface. It can be shown, however [e.g., from Durand's¹¹⁶ expression (118)], that the right-hand side of Eq. (4.7) yields the sum of $p^{(1)}$ and p_{es} at the liquid's surface as long as the electric field is perpendicular to this surface. As $p^{(1)}$ vanishes inside the liquid, Hakim and Higham's result applies if the considered point is not situated at the surface. Therefore, we insert for p_{el} in Eq. (4.9) the total pressure difference $p^{(1)} + p_{es}$.

IV.3. Potential distributions

Assuming in the equilibrium state the electric potential Φ to be independent of z , Φ has to satisfy the two-dimensional Laplace equation:

$$(\partial^2/\partial x^2 + \partial^2/\partial y^2)\Phi = 0 \quad . \quad (4.10)$$

This equation has to be solved in air as well as in the thermoplastic layer.

In order to state the boundary conditions we remark that, initially, the surface carries a uniform potential and charge density. When the charging stage is finished and the film is heated, the potential distribution will change because of the layer deformation and the charge leakage through this layer. The leakage current depends nonlinearly on the electric field strength¹¹⁸ and on the temperature^{75, 118}, while the total charge loss is a function of the heating time. To describe this complex situation, two simple models have been proposed^{24, 41, 62}: one using a uniform charge density (perfectly insulating surface), the other a uniform surface potential. Budd⁴¹ concluded that the latter model is more appropriate. Killat²⁴, however, asserted that the

insulating surface is a better model, although in his experiments the electric charging was continued during the heating stage. He generated thereby a practically uniform potential on the thermoplastic surface^{62,104} because the (positive) charges tend to flow to places with a lower potential until all surface parts have acquired the same potential. Moreover, for several configurations^{119,120} it can be shown that throughout the space extending a few μm above the surface, the potential has practically the same value, provided that the charger is located a few cm above it. A uniform surface potential can be thus readily approximated in practice. Therefore, we prefer to consider the equipotential model first.

Some published solutions^{24,41,121} to Laplace's equation are related to our problem. To our knowledge, however, a solution, valid for all possible wavelengths and amplitudes of the deformation, has not been published. In the present paper, this solution is derived using a method^{122,123} in which the area is divided into subareas and the separate solution of Laplace's equation in each subarea is obtained.

In both models we consider a section of the deformed layer extending between $x = 0$ and $x = \frac{1}{2}\lambda$ (Fig. 4.5). This section is divided into M slices of equal thickness parallel to the yz plane.

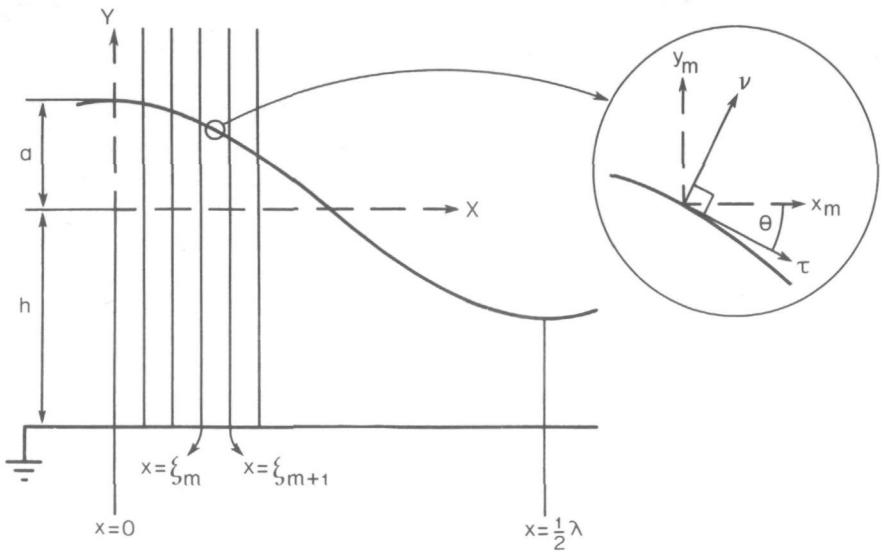


Fig. 4.5. On the derivation of the potential distributions: a $\frac{1}{2}\lambda$ section of the deformed layer is divided into M subareas.

IV.3.1. Equipotential model

In this model, the constant potential at the wrinkled surface is associated with surface charge fluctuations that affect the surface tension. In equilibrium, the electric forces perpendicular to the curved surface are in balance with the components of the surface tension in the same direction.

Solutions of Laplace's equation for the m th subarea in thermoplastic and air, respectively, are given by

$$\Phi_{tp,m} = A_{0m} + A_{1m}y_m + [A_{2m} \sinh ky_m + A_{3m} \cosh ky_m] \cos kx_m \quad , \quad (4.11)$$

$$\Phi_{air,m} = B_{0m} + B_{1m}y_m + [B_{2m} \exp ky_m + B_{3m} \exp(-ky_m)] \cos kx_m \quad , \quad (4.12)$$

in which A_{lm} and B_{lm} are constants, $l = 0, 1, 2, 3$, and $\xi_m < x_m < \xi_{m+1}$, where $\xi_m = \frac{1}{2}\lambda m/M$, $m = 0, 1, 2, \dots, M-1$.

If Y_m is limiting value of the order of $10/k$ and $u(x_m) = a \cos kx_m$, the boundary conditions are

$$\Phi_{tp,m} = 0 \quad \text{for } y_m = -h \quad , \quad (4.13.a)$$

$$\Phi_{air,m} < \infty \quad \text{for } y_m = Y_m \quad , \quad (4.13.b)$$

$$\frac{\partial \Phi_{tp,m}}{\partial \tau} = 0 \quad \text{for } y_m = u(x_m) \quad , \quad (4.13.c)$$

$$\Phi_{tp,m} = \Phi_s \quad \text{for } y_m = u(x_m) \quad , \quad (4.13.d)$$

$$\Phi_{air,m} = \Phi_{tp,m} (= \Phi_s) \quad \text{for } y_m = u(x_m) \quad , \quad (4.13.e)$$

where h is the thickness of the layer before deformation and τ is a coordinate in the xy plane tangential to the surface. Note that, in principle, the boundary conditions (4.13.c) and (4.13.d) are equivalent. In the approximation we use in our derivation (see Appendix B), however, this is not the case and consequently both conditions have to be applied simultaneously.

Condition (4.13.c) can be written as

$$\frac{\partial x_m}{\partial \tau} \left[\frac{\partial \Phi_{tp,m}}{\partial x_m} \right]_{y_m=u(x_m)} + \frac{\partial y_m}{\partial \tau} \left[\frac{\partial \Phi_{tp,m}}{\partial y_m} \right]_{y_m=u(x_m)} = 0 \quad . \quad (4.14)$$

Here, the derivatives with respect to τ can be obtained (see the inset in Fig. 4.5) from

$$\begin{pmatrix} x_m \\ y_m \end{pmatrix} = \begin{pmatrix} \cos \theta & -\sin \theta \\ \sin \theta & \cos \theta \end{pmatrix} \begin{pmatrix} \tau \\ \nu \end{pmatrix}, \quad (4.15)$$

where ν is the coordinate normal to the surface and $\theta = \arctan(\frac{du}{dx_m})$. If M is sufficiently large (see Appendix B), we can express the potential in the thermoplastic layer as

$$\begin{aligned} \phi_{tp,m} = & \frac{\phi_s}{h} \frac{1 + \alpha_m k \coth[k(h + \alpha_m)]}{1 + (1 + \alpha_m/h) \alpha_m k \coth[k(h + \alpha_m)]} \times \\ & \times \left\{ h + y_m - \frac{a \sinh[k(h + y_m)] \cos kx_m}{\sinh[k(h + \alpha_m)] + \alpha_m k \cosh[k(h + \alpha_m)]} \right\}, \quad (4.16) \end{aligned}$$

in which $\alpha_m = a \cos(k\xi_m)$.

Similarly, we can derive the potential distribution in the air. This results in

$$\phi_{air,m} = \phi_s, \quad u(x_m) \leq y_m \leq Y_m, \quad (4.17)$$

compare our previous remark about the practically uniform potential within a region several μm above the surface.

IV.3.2. Nonequipotential model

For comparison we consider the other model in which previous authors^{24,62} assumed a uniform charge density. If the deformation amplitude is not very small, Laplace's equation cannot be solved within this model since the boundary conditions appear to be incompatible. Therefore, we again introduce a dependency of the surface charge density $\sigma(x_m)$ on x_m , but contrary to the equipotential model we now assume a nonvanishing tangential component of the electric field. Herewith the boundary conditions are described by

$$\phi_{tp,m} = 0 \quad \text{for } y_m = -h, \quad (4.18.a)$$

$$\phi_{air,m} < \infty \quad \text{for } y_m = Y_m, \quad (4.18.b)$$

$$\frac{\partial \Phi_{tp,m}}{\partial \tau} = \frac{\partial \Phi_{air,m}}{\partial \tau} \quad \text{for } y_m = u(x_m) \quad , \quad (4.18.c)$$

$$\epsilon_0 \left(- \frac{\partial \Phi_{air,m}}{\partial v} \right) - \epsilon_0 \epsilon_{r1} \left(- \frac{\partial \Phi_{tp,m}}{\partial v} \right) = \sigma(x_m) \quad \text{for } y_m = u(x_m) \quad , \quad (4.18.d)$$

$$\Phi_{tp,m} = \Phi_{air,m} \quad \text{for } y_m = u(x_m) \quad , \quad (4.18.e)$$

where the relative permittivity of air is put equal to unity. The following solutions of Laplace's equation satisfy boundary conditions (4.18.a) and (4.18.b), respectively:

$$\Phi_{tp,m} = C_{1m}(h+y_m) + C_{2m} \frac{\sinh[k(h+y_m)]}{\sinh kh} \cos kx_m \quad , \quad (4.19)$$

$$\Phi_{air,m} = D_{0m} + D_{2m} \exp(-ky_m) \cos kx_m \quad , \quad (4.20)$$

in which the constants C_{2m} and D_{2m} , using Eq. (4.18.c) and with the aid of Eq. (4.15), are for sufficiently large M approximated by

$$C_{2m} = - \frac{C_{1m} a \sinh kh}{\sinh[k(h+a_m)] + \cosh[k(h+a_m)]} \quad , \quad (4.21)$$

$$D_{2m} = \frac{C_{1m} \exp ka_m}{1 + \tanh[k(h+a_m)]} \quad . \quad (4.22)$$

On the other hand, from condition (4.18.d) and Eqs. (4.19) and (4.20) we obtain

$$\begin{aligned} & [\cos kx_m + ak \sin^2(kx_m)] \epsilon_0 D_{2m} k \exp(-ka_m) + \epsilon_0 \epsilon_{r1} C_{1m} + \\ & + \{ \cosh[k(h+a_m)] \cos kx_m - ak \sinh[k(h+a_m)] \} \times \\ & \times \sin^2(kx_m) \} \epsilon_0 \epsilon_{r1} C_{2m} k / \sinh kh = \\ & = \sigma(x_m) [1 + a^2 k^2 \sin^2(kx_m)]^{\frac{1}{2}} \quad . \end{aligned} \quad (4.23)$$

The left-hand side can be written as $\sigma_c + \sigma_h$, where σ_c is the constant part and σ_h depends harmonically on x_m . Then

$$C_{lm} = \sigma_c / \epsilon_0 \epsilon_{r1} \quad , \quad (4.24)$$

and substituting Eqs. (4.21), (4.22), and (4.24) into Eq. (4.23), we can express σ_h in terms of σ_c . The surface charge density $\sigma(x_m)$ can then be calculated as

$$\begin{aligned} \sigma(x_m) = & \frac{\sigma_c}{[1 + a^2 k^2 \sin^2(kx_m)]^{\frac{1}{2}}} \times \\ & \times \left[1 + \frac{(1/\epsilon_{r1}) + \tanh[k(\bar{h} + \alpha_m)]}{1 + \tanh[k(\bar{h} + \alpha_m)]} a^2 k^2 \sin^2(kx_m) + \right. \\ & \left. - \frac{(1 - 1/\epsilon_{r1}) ak \cos kx_m}{1 + \tanh[k(\bar{h} + \alpha_m)]} \right] . \end{aligned} \quad (4.25)$$

Only when ak is extremely small can the charge density be approximated by σ_c , and in this case the earlier mentioned publications^{24,41,62} apply. The constant D_{0m} in Eq. (4.20) can be found by applying boundary condition (4.18.e). The resulting potential distributions are then

$$\Phi_{tp,m} = \frac{\Phi_{s0}}{h} \left(\bar{h} + y_m - \frac{a \sinh[k(\bar{h} + y_m)] \cos kx_m}{\sinh[k(\bar{h} + \alpha_m)] + \cosh[k(\bar{h} + \alpha_m)]} \right) , \quad (4.26)$$

$$\Phi_{air,m} = \frac{\Phi_{s0}}{h} \left(\bar{h} + \frac{a \exp[-k(y_m - \alpha_m)] \cos kx_m}{1 + \tanh[k(\bar{h} + \alpha_m)]} \right) , \quad (4.27)$$

where $\Phi_{s0} = \sigma_c h / \epsilon_0 \epsilon_{r1}$ denotes the surface potential for $a = 0$.

IV.4. Relation between λ and a

IV.4.1. Equipotential model

From the foregoing formulas, we now derive a relation between the spatial wavelengths and the amplitudes of the frost deformation. Equation (4.6) can be written as

$$d\gamma = -\sigma d\Phi_s \quad . \quad (4.28)$$

**uiterlijk
terugbezorgen
op:**

2 2 AUG. 8 0

Gelieve dit werk
aan onderstaand
adres terug te
bezorgen of
goed verpakt
gefrankeerd terug
te zenden



**bibliotheek
technische
hogeschool
delft**

Doelenstraat 101
2611 NS Delft

Postbus 98
2600 MG Delft

015 - 78 56 79

At the extremes of the surface deformation, the surface charge density (being equal to the normal component of the electric flux density) is given by

$$(\sigma)_{max,min} = \epsilon_0 \epsilon_{r1} \left[- \frac{\partial \Phi}{\partial y_m} \right]_{max,min} \quad (4.29)$$

Integrating Eq. (4.28) over $[0, \phi_s]$ and applying Eqs. (4.16) and (4.29) we obtain

$$(\gamma)_{max,min} = \tilde{\gamma} - (\epsilon_0 \epsilon_{r1} \phi_s^2 \alpha_{max,min}) / 2h \quad , \quad (4.30)$$

where

$$\begin{aligned} \alpha_{max} &= \{ 1 + (1 + a/h) ak \coth[k(h+a)] \}^{-1} \quad , \\ \alpha_{min} &= \{ 1 - (1 - a/h) ak \coth[k(h-a)] \}^{-1} \quad , \end{aligned} \quad (4.31)$$

and $\tilde{\gamma}$ denotes the value of the surface tension at the softening temperature without the influence of electric charges. On the other hand, according to Eqs. (4.8) and (4.9) the pressures induced by the electric field are equal to

$$(p_{el})_{max,min} = \epsilon_0 \left(\frac{1}{2} \epsilon_{r1} + \frac{(\epsilon_{r1} + 2)(\epsilon_{r1} - 1)}{6} \right) \left[\frac{\partial \Phi}{\partial y_m} \right]_{max,min}^2 \quad , \quad (4.32)$$

so that together with Eqs. (4.4) and (4.30), we obtain the expression for the wavelength-thickness ratio λ/h in the equilibrium state

$$\frac{\lambda}{h} = 2\pi \left\{ \frac{(a/h) [(U_{th}/\phi_s)^2 - \frac{1}{2}(\alpha_{max} + \alpha_{min})]}{[\frac{1}{2} + (\epsilon_{r1} + 2)(\epsilon_{r1} - 1)/6\epsilon_{r1}] (\alpha_{min}^2 - \alpha_{max}^2)} \right\}^{\frac{1}{2}} \quad . \quad (4.33)$$

The quantity $U_{th} = (2\tilde{\gamma}h/\epsilon_0 \epsilon_{r1})^{\frac{1}{2}}$ is the threshold voltage for the frost deformation; compare Cressman⁶¹.

With $\epsilon_{r1} = 2.3$ for²⁴ Staybelite Ester 10, computations yield λ/h as a function of a/h with ϕ_s/U_{th} as a parameter. The result is shown in Fig. 4.6. After insertion of Eq. (4.31) into Eq. (4.33), an equation for λ/h resulted that turned out to have no real solution in the region below the dashed curve. To interpret this, note that the frost growth, starting when the layer is softened, continues as long as equilibrium is not reached. We assume that this growth process occurs in the region where equilibrium equation (4.33) cannot

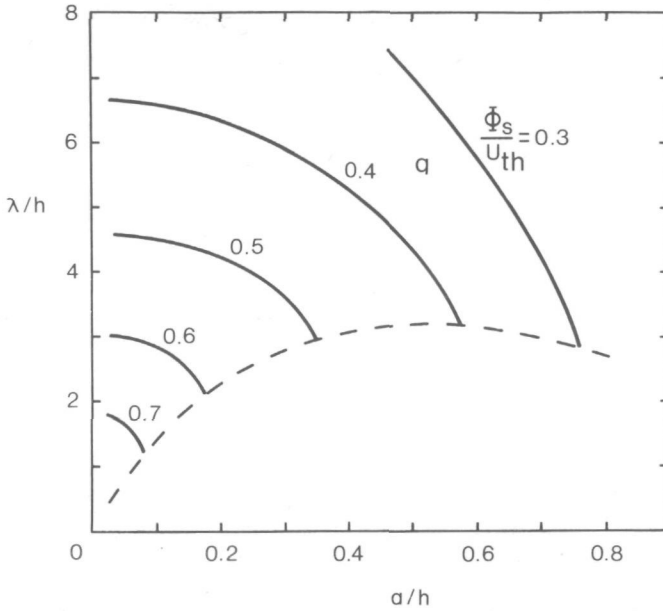


Fig. 4.6. Relation between λ/h and a/h in the equilibrium state for several values of Φ_s/U_{th} ; equipotential surface, $\epsilon_{r1} = 2.3$. No solution is obtained below the dashed curve.

be solved. When the boundary of this region is reached, Eq. (4.33) becomes solvable and in the resulting equilibrium state the growth process will terminate. Hence, in this model the final deformation should have a tendency to follow the dashed curve.

IV.4.2. Nonequipotential model

We now consider the model with a nonequipotential surface (see Sec. IV.3.2). Integration of Eq. (4.28) yields, using Eqs. (4.25) and (4.26),

$$\gamma = \tilde{\gamma} - \frac{\epsilon_0 \epsilon_{r1} \Phi_{s0}^2}{2h[1 + a^2 k^2 \sin^2(kx_m)]^{1/2}} \left(1 + \frac{(1/\epsilon_{r1}) + \tanh[k(h+a_m)]}{1 + \tanh[k(h+a_m)]} a^2 k^2 \sin^2(kx_m) + \frac{(1 - 1/\epsilon_{r1}) ak \cos kx_m}{1 + \tanh[k(h+a_m)]} \right) \left(1 + \frac{(a/h) \cos kx_m}{1 + \tanh[k(h+a_m)]} \right) \quad (4.34)$$

which at the extremes of the deformation reduces to

$$\begin{aligned}
 (\gamma)_{max,min} &= \bar{\gamma} - \left(\frac{\epsilon_0 \epsilon_{r1} \Phi_{s0}^2}{2h} \right) \left[1 - \left(1 - \frac{1}{\epsilon_{r1}} \right) \beta_{max,min} \right] \times \\
 &\times \left(1 + \frac{\beta_{max,min}}{kh} \right) , \quad (4.35)
 \end{aligned}$$

where

$$\begin{aligned}
 \beta_{max} &= ak\{1 + \tanh[k(h+a)]\}^{-1} , \\
 \beta_{min} &= -ak\{1 + \tanh[k(h-a)]\}^{-1} . \quad (4.36)
 \end{aligned}$$

The pressures due to the electric field are, according to Eqs. (4.8) and (4.9), given by

$$\begin{aligned}
 (p_{el})_{max,min} &= \epsilon_0 \left(\frac{1}{2} \epsilon_{r1} + \frac{(\epsilon_{r1} + 2)(\epsilon_{r1} - 1)}{6} \right) \times \\
 &\times \left[\frac{\partial \Phi}{\partial y_m} \right]_{max,min}^2 - \frac{1}{2} \epsilon_0 \left[\frac{\partial \Phi}{\partial y_m} \right]_{max,min}^2 . \quad (4.37)
 \end{aligned}$$

By substituting Eqs. (4.35) and (4.37) into Eq. (4.4) we obtain the expression for the wavelength-thickness ratio at equilibrium:

$$\begin{aligned}
 \frac{\lambda}{h} &= 2\pi \left\{ \frac{\alpha}{h} \left[\frac{1}{2} + \frac{(\epsilon_{r1} + 2)(\epsilon_{r1} - 1)}{6\epsilon_{r1}} \right]^{-1} \times \right. \\
 &\times \left[\left(\frac{U}{\Phi_{s0}} \right)^2 - \frac{1}{2} \left(2 + (\beta_{max} + \beta_{min}) [-1 + \epsilon_{r1}^{-1} + (kh)^{-1}] \right) \right. \\
 &\left. \left. - \frac{(1 - \epsilon_{r1}^{-1})(\beta_{max}^2 + \beta_{min}^2)}{kh} \right) \right] \left[2(\beta_{max} - \beta_{min}) + \right. \\
 &\left. \left. + \{ 1 - [\epsilon_{r1} + \frac{1}{3}(\epsilon_{r1} + 2)(\epsilon_{r1} - 1)]^{-1} \} (\beta_{min}^2 - \beta_{max}^2) \right]^{-1} \right\}^{\frac{1}{2}} . \quad (4.38)
 \end{aligned}$$

The relation between λ/h and a/h , computed for several values of Φ_{s0}/U_{th} , is presented in Fig. 4.7. Within a certain region in this diagram, the free energy

of the layer appears to be negative. This free energy for a frosted area A is equal to $\bar{E}A$, where the mean energy \bar{E} of the layer can be written (cf. Cressman⁶¹ and Budd⁴¹).

$$\bar{E} = \frac{2}{\lambda} \int_0^{\frac{1}{2}\lambda} \int_0^1 \gamma \left[1 + \left(\frac{du}{dx_m} \right)^2 \right]^{\frac{1}{2}} dx_m dz \quad (4.39)$$

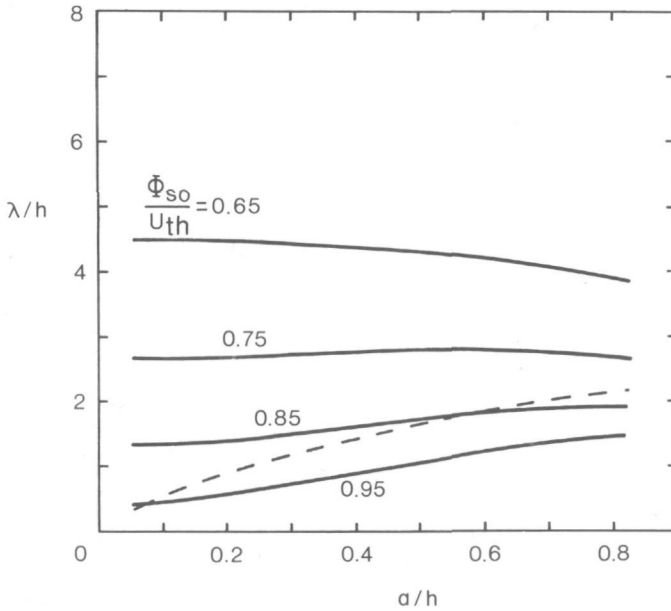


Fig. 4.7. Relation between λ/h and a/h in the equilibrium state for several values of Φ_{s0}/U_{th} ; nonequipotential surface (see Sec. IV.3.2), $\epsilon_{p1} = 2.3$. The free energy of the layer is negative below the dashed curve.

The specific surface energy γ is identically given by Eq. (4.34). No distinction exists between the specific surface energy and the surface tension, since our deformation was considered to be of the plastic type^{111,112}. From Eqs. (4.39) and (4.34), the dashed curve in Fig. 4.7 is obtained, along which $\bar{E} = 0$ and below which $\bar{E} < 0$. We know that frost deformation commences when a negative surface tension (thus a negative free energy) makes the surface unstable⁶¹. We may thus expect that a final deformation, which must be free from any instability, can only appear upon or above the dashed curve. But a stable equilibrium always requires a minimal energy¹²⁴. Hence, in this model the ultimate deformation should occur at the curve where $\bar{E} = 0$. (A similar calculation for the

equipotential case yields a positive energy along and above the dashed curve in Fig. 4.6.)

In Fig. 4.8 we compare the dashed curves, upon which the final deformation in the two models should occur, with kh as the ordinate. It is seen that the equipotential model has a greater tendency to select a predominant value of kh (at the nearly horizontal part of the curve). This agrees with previous experimental results^{24, 84} that the best reproducibility is obtained if the corona is kept working during the heating stage, hence if the surface is practically equipotential (cf. remarks in the third paragraph of Sec. IV.3). Furthermore, the resulting predominant value of kh , like that from Killat and Terrell⁸⁴, is approximately equal to 2. In a wide range of the amplitude a , which implies an important range of ϕ_s/U_{th} (see Fig. 4.6), our equipotential model leads to the same value.

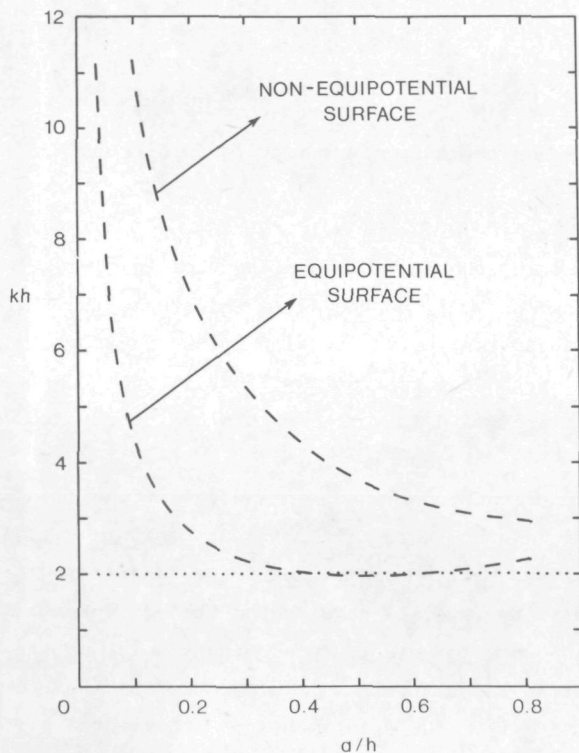


Fig. 4.8. The dashed curves from Figs. 4.6 and 4.7 are redrawn with kh as the ordinate. The dotted line represents the resulting predominant value of kh from the experiments of Killat and Terrell.

Finally, we consider the experimental results of Gravel¹²⁵. He gave his single-layer photothermoplastic film a voltage lower than the threshold value U_{th} , so that no frost bubbles appeared when the film was heated. The bubbles did appear, however, at parts of the film that were exposed to light before and during the heating stage. At that time none of the available models could explain this. We note according to Figs. 4.6 and 4.7 that frost deformation can grow even when the surface potential is lower than U_{th} , provided that the growth occurs in the forbidden region (i.e., the region of no equilibrium in Fig. 4.6 or the region of instability in Fig. 4.7). In Gravel's film, a spatial difference in the electric pressure exists, due to a charge decrease at the exposed area⁵⁴. If the film is softened, the extrapressure from the rest of the film induces an instability at the exposed area, starting the growth of the frost deformation.

IV.5. Discussion

IV.5.1. The frost wavelength and the optimal wavelength in thermoplastic recordings

In our quasistatic approach, the spatial wavelength of the frost deformation is found to depend not only on the layer thickness, the surface potential, the permittivity, and the surface tension of the layer (as in earlier dynamic theories), but also on the deformation amplitude. We have derived potential distributions that are valid for all possible amplitudes and wavelengths of the deformation.

Two models have been considered, one involving an equipotential surface, the other a nonequipotential surface; this latter transforms into a model having a uniform charge density when the amplitude of the deformation is extremely small as compared to the spatial wavelength. The equipotential model appears to show a greater tendency to select a predominant value of the ratio between that wavelength and the layer thickness. This ratio is found to be in good agreement with the results from the experiments of other authors. Verification of our theory with the frost deformation experimentally obtained, will be given in Sec. VI.3.

We remark that one may not simply compare the frost wavelength calculated theoretically to the spatial wavelength of maximal response in a thermoplastic recording. This is because the boundary and initial conditions for the frost

deformation are different from that of an usual optical recording, see Sec. III.7.

Unfortunately, some authors^{32,92} have applied Budd's theory for comparing the spatial wavelength of maximal response of their *recordings*, while this theory was actually only intended for *frost deformation*. Consequently, some discrepancy was unavoidable.

On the other hand, the frost bubbles encountered *in* a holographic recording (which lowers the signal-to-noise ratio) may have a predominant wavelength equal to the spatial wavelength of the holographic fringes⁵⁶, provided that the fringes have a wavelength near to the "natural" frost predominant wavelength⁵⁴ (i.e., the predominant wavelength on the unexposed film). This is because in the early stage of the deformation process, the small, information-related surface corrugation can act as the initial deformation for the frost bubbles. Then, depending on the recording conditions (such as whether the recorded information has a low modulation, see Sec. III.5.4) this initial deformation will grow. This causes the frost wavelength (which, in the unexposed case, is already close to the fringes' wavelength) to be "tuned" to the wavelength of the holographic fringes.

IV.5.2. *On the phase separation phenomenon*

Reich *et al.*³⁷ have suggested that frost deformation is caused by spinodal decomposition in the thermoplastic material, instead of by a fluctuation of the surface tension due to the deposited charges. This spinodal decomposition is a phase separation phenomenon¹²⁶ that can be encountered in multicomponent materials (such as polydispersed and plasticized polymers) under application of thermal and electric stresses.

One of the motivations to propose this mechanism was the discrepancy between the "factor of 2 rule" resulting from Budd's theory (relating the frost wavelength to the thermoplastic thickness, based upon surface tension fluctuations) and the observed ratio of the optimal spatial wavelength to the layer thickness in holographic recordings. To support their suggestion, Reich *et al.* have prepared films using a single component thermoplastic material (i.e. polymer having a sharp defined molecular weight) as well as films from a multicomponent material. Indeed, the holograms recorded on single-component films showed a significantly higher signal-to-noise ratio than on the multi-component films.

We remark that, since the frost deformation and the deformation constituting a holographic recording are two different things that ought to be

considered separately (see Sec. IV.5.1), the aforementioned discrepancy is unavoidable.

Apart from this, in order to compare with the observed frost wavelengths, we have gathered some values of the spatial wavelength from phase separation (not related to frost deformation) as reported in literature¹²⁷⁻¹³¹. Actually, we have found only a single result valid for polymers¹³¹ (in other inspected publications concerning phase separation in polymers, the spatial wavelength, or the thickness of the sample, or both, were not mentioned). Nevertheless, the data observed in glasses¹²⁷⁻¹³⁰ are presented here to seek a certain trend, if any, in the ratio between the wavelength λ_{ps} and the sample thickness h_{ps} , see Table IV.1.

Table IV.1. Results obtained from phase separation, relating the spatial wavelength λ_{ps} and the sample thickness h_{ps}

λ_{ps} (μm)	h_{ps} (μm)	λ_{ps}/h_{ps}	Reference
0.002	0.1	2×10^{-2}	Anderson and Luehrs ¹²⁷
0.125	5000	2.5×10^{-5}	deVekay and Majumdar ¹²⁸
0.4	25000	1.6×10^{-5}	Flannery <i>et al.</i> ¹²⁹
0.01	70000	1.4×10^{-7}	Schmidt and Charles ¹³⁰
0.1	600	1.6×10^{-4}	McMaster ¹³¹
500	600	8×10^{-1}	McMaster ¹³¹ (coarsening effect)

It is seen that the ratio λ_{ps}/h_{ps} is spread over a very broad range of values. Moreover, its magnitude tends to be very much lower than the values λ_{pt}/h observed in frost deformation as depicted in Fig. 4.1. An exception is the second result from McMaster; however, the 500 μm spatial wavelength was obtained not less than about 100 minutes after the first value (0.1 μm) was established. According to the author, this coarsening has been caused by a mechanism other than the spinodal decomposition.

The apparently absence of correlation between λ_{ps} and h_{ps} in Table IV.1 is in agreement with the theory^{126,132}, viz., that no thickness factor appears in the expression for the spatial wavelength in the spinodal decomposition. On the contrary, the predominant wavelength to thickness ratio for frost deformation is still confined within a certain value range (between 1 and 4), see Fig. 4.1.

In fact, those values obtained with a continuing corona (which tends to produce an equipotential surface, see Sec. IV.3) have been reported to be reproducible and are located within a relatively narrow spread around $\lambda_{pt}/h = \pi$. This agrees with the equipotential model in our quasistatic theory.

The rest of the values in Fig. 4.1 (the open circles) were obtained with the heating stage separated from charging. Then, the thermoplastic surface cannot be expected to have a homogeneous potential, and according to our non-~~the~~ equipotential model, the predominant wavelength-to-thickness ratio cannot be sharply defined.

Hence, we suggest that the final shape of the frost deformation is well-determined by the surface tension and the electric forces. The role of phase separation can be found in the factor δL ("microscopic noise level deformation")²⁴ and "noiselike microscopic bubbles" (see Sec. IV.2.1), i.e. one of the stimuli for frost deformation, which will grow further under the influence of the existing forces. Other examples of the stimuli are dust particles and tiny craters caused by ion bombardment.

We have made a photomicrograph of frost bubbles on our film, carrying some dust particles (see Fig. 4.9). It is seen that the perturbation around the dust particle shows a concentrated structure and has a slightly higher contrast (hence, larger deformation) than the rest, suggesting that such a dust particle functions as a stimulus for the frost bubbles, indeed.

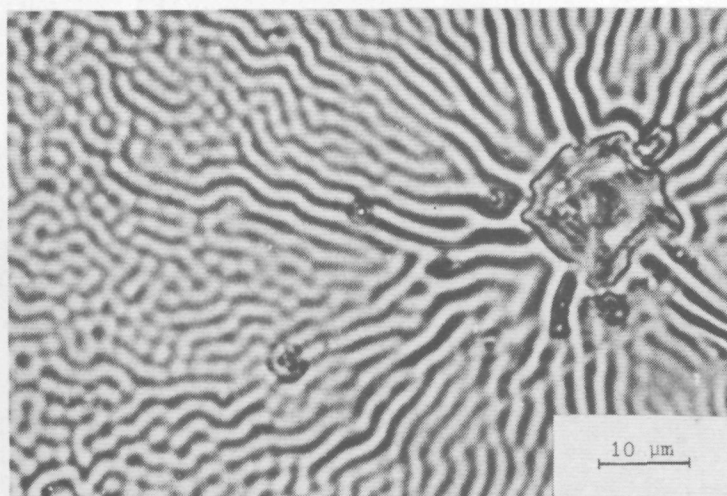


Fig. 4.9. Photomicrograph of frost bubbles around a dust particle.

The low signal-to-noise ratio of films consisting of multicomponent thermoplastic material can be explained with the aforementioned mechanism, i.e. a phase separation produces microscopic bubbles, which in their turn grow to form the quasi-random frost deformation.

To summarize, we suggest that the behaviour of frost deformation is ultimately determined by the surface tension and the electric forces. A phase separation plays its role more likely as a stimulus for the frost bubbles, than as the sole mechanism for this deformation.

V. A CAMERA SYSTEM FOR THE RECORDING PROCESS

In this chapter we describe a system that enables us to carry out the recording process with our film. For convenience, the cross section of the film previously shown in Fig. 2.1.b is again depicted in Fig. 5.1. It has a width of 35 mm and is delivered from the manufacturer¹⁷ on a roll with a length of 30 m. The conductive layer is not attached to the film but is deposited upon an auxiliary glass plate (the "heat plate"), which is a component of the system.

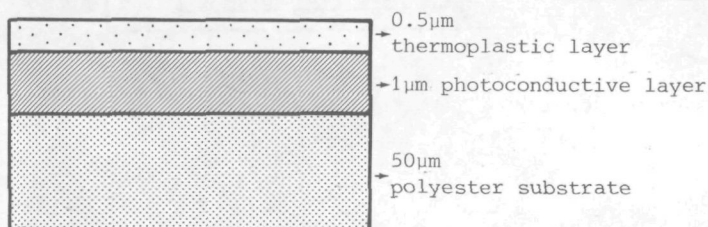


Fig. 5.1. Cross section of the film used in our experiments.

A schematic overview of our system is given in Fig. 5.2. The general set-up is based upon that of a commercially available apparatus¹⁷, but modifications related to the transport, heating and charging systems have been introduced. With regard to its construction, the system can be divided into a camera, a shutter, a high-voltage supply and an electronic control box. We can distinguish two subsystems having different functions in the recording process, i.e. a subsystem for the film transport, and a subsystem for performing the recording stages which consists of a charging section, an exposure section, a development section (with temperature control) and a facility to select one among several possible sequences of recording steps.

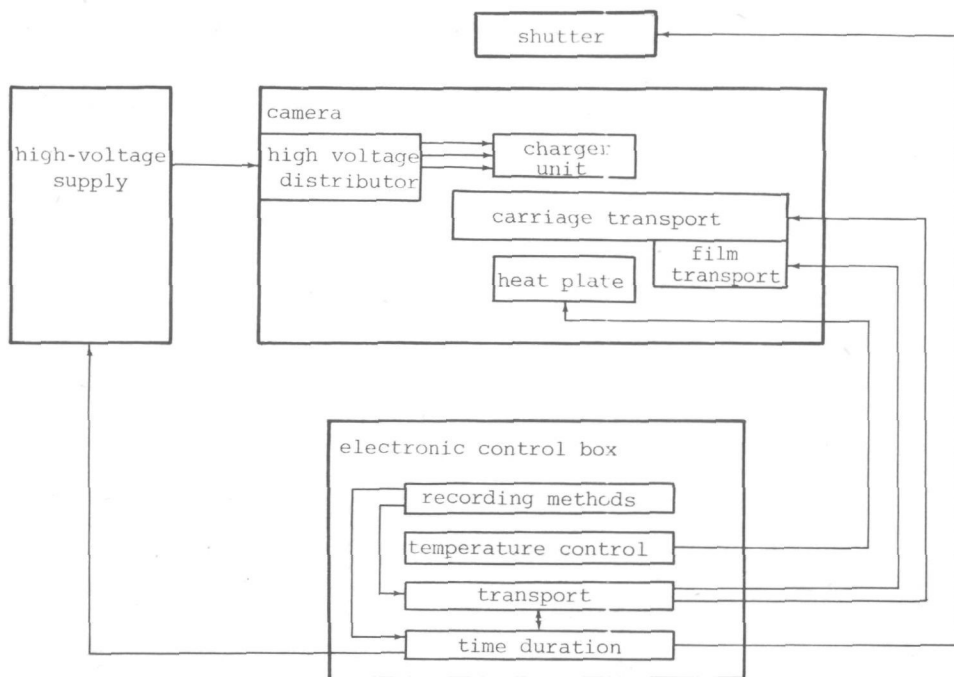


Fig. 5.2. Schematic overview of the apparatus.

V.1. The camera

In the camera, see Figs. 5.3 and 5.4, one can find some components of the mechanism for the film transport as well as a high voltage distributor, a charger unit and the heat plate.

V.1.1. Film transport mechanism

This mechanism (see Figs. 5.4 and 5.5.a) consists in principle of a motor to wind the film and a carriage that can be moved with the aid of a second motor. In this carriage, which normally (in the idle state) is situated in the centre or at the right-hand side of the camera, the charger unit and two rollers are mounted.

When the instruction for the film transport starts (by depressing the relevant button at the panel of the electronic control box), the carriage begins to move to the left, see Fig. 5.5.b. During this movement, roller 2

lifts the film from the heat plate.

When the carriage has passed the heat plate and comes to the left-hand side of the camera, it turns a microswitch which, via the electronic control, turns off the motor which has shifted the carriage. At this moment, the film is completely free from the heat plate. Immediately, the film winding motor is

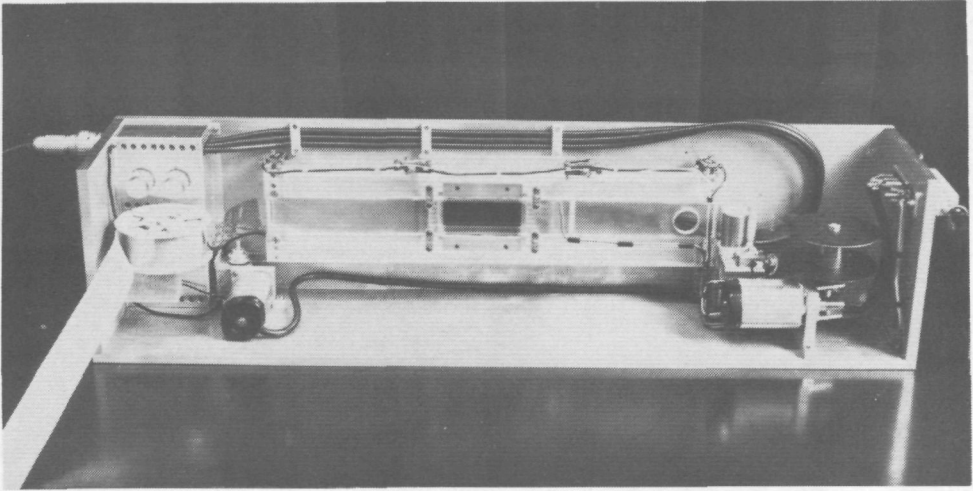


Fig. 5.3. The camera, back view.

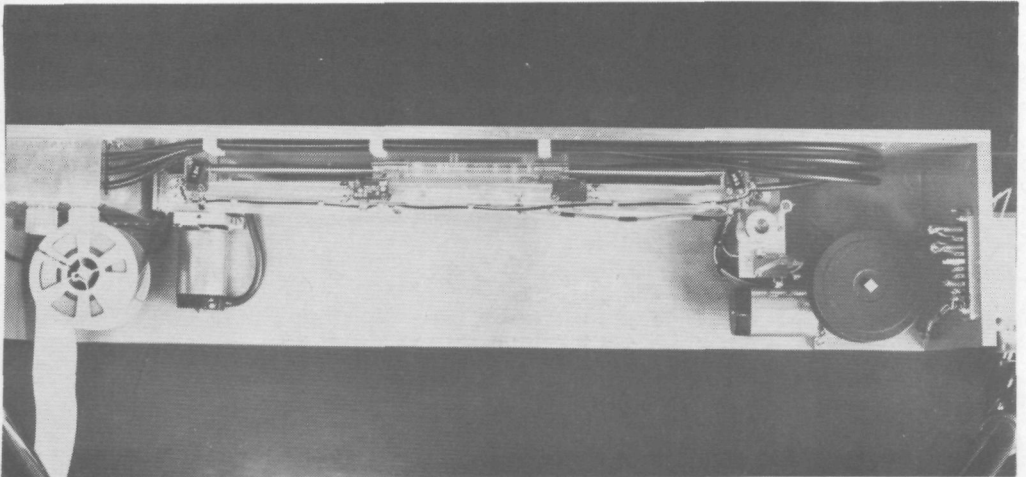


Fig. 5.4. The camera, upper view.

activated to transport the film along a distance of a single recording frame, see Fig. 5.5.c.

Normally, the length of a frame is equal to the length of the heat plate (80 mm). But one can also utilize the "economical" frame size, in which this length is about 45 mm. This economical frame size is meant to save film material, e.g. when the optimal recording parameters have not been attained and must be sought first by trial and error. The film transport along either the

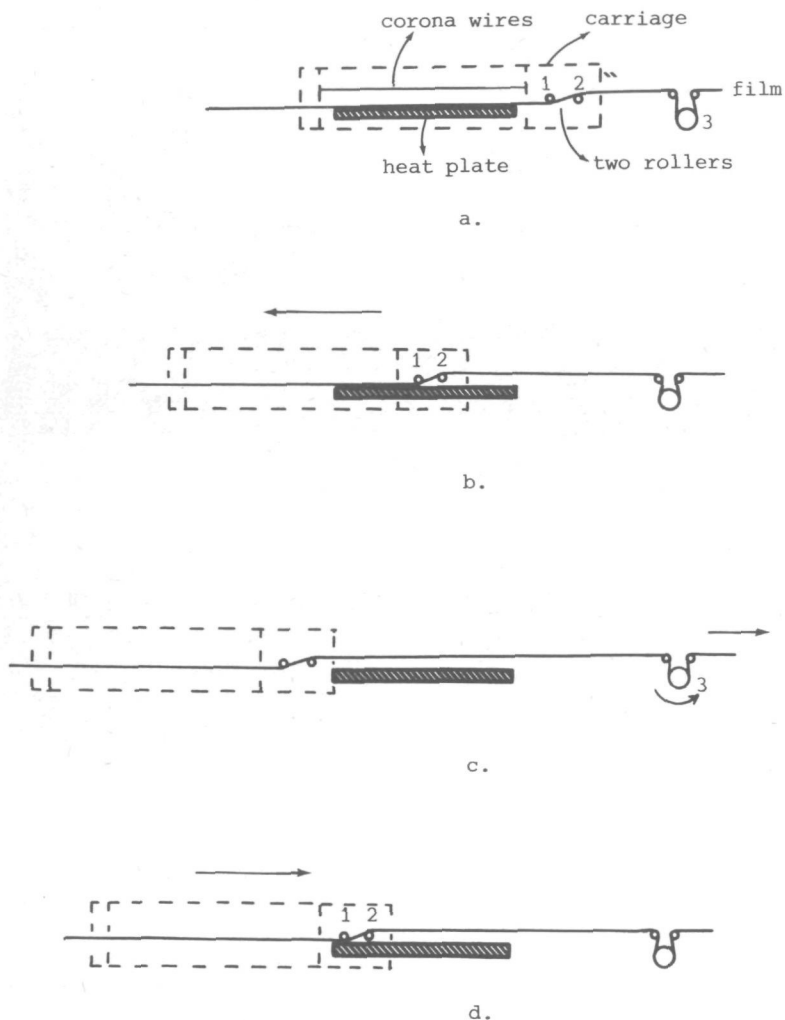


Fig. 5.5. The movements for transporting the film (see text).

normal or the economical frame length is directed by the electronic control through roller 3, the perimeter of which is equal to the desired frame size (actually, a hollow cylinder can be sheathed onto the roller such that two perimeters are available).

If the film transport is completed, the carriage moves to the right, see Fig. 5.5.d. Roller 1 presses the film against the heat plate to provide a preliminary contact (the actual adherence occurs by charges deposited during the charging stage). The adherence is necessary for the mechanical stability of this flexible film, and for a good thermal contact during development.

Passing centre of the camera, the carriage turns off the carriage motor by depressing two microswitches. With the carriage now facing the heat plate, the recording stages can start (see Sec. V.4.2).

V.1.2. High-voltage distributor

The distributor, mounted at the left-hand side of the camera (Fig. 5.3), is intended to distribute the high voltage to each of the wires in the charger unit. If necessary, it can be used to carry out adjustment of this voltage. Its schematic diagram is given in Fig. 5.6.

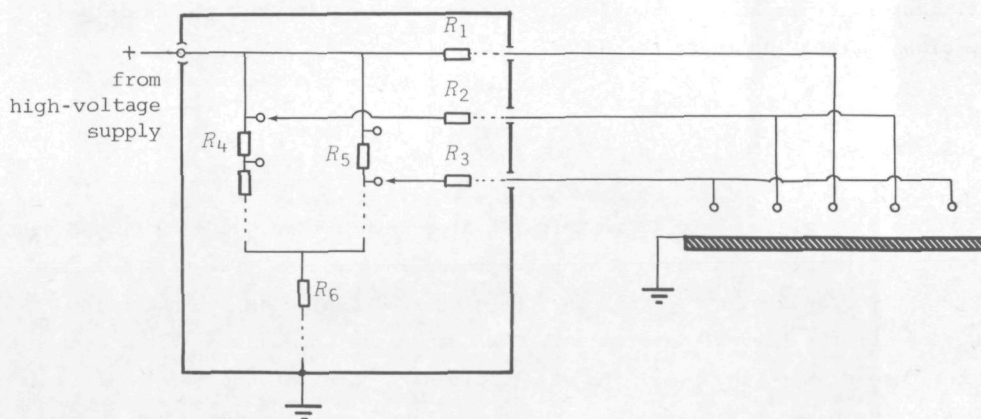


Fig. 5.6. The high-voltage distributor (left), and its connection to the charger unit (right). R_1 , R_2 , R_3 , each consists of 15 resistors @ 820 k Ω , in series. R_4 , R_5 , each consists of 9 resistors @ 120 k Ω , in series. R_6 consists of 19 resistors @ 180 k Ω , in series.

The high voltage connection is divided into three lines, which are coupled to the wires of the charger unit via a network of 12.3 M Ω resistors. With the high-voltage supply operating at 12 kV (this is about the maximal useful value), the resistor network limits the current in each line to less than 1 mA, or 3 mA in total. This last value does not lead to a serious shock¹³³, and is surely below the lethal limit¹³³, if one accidentally comes into contact with the corona wires while the system is working (nevertheless, such a contact should be avoided in any case).

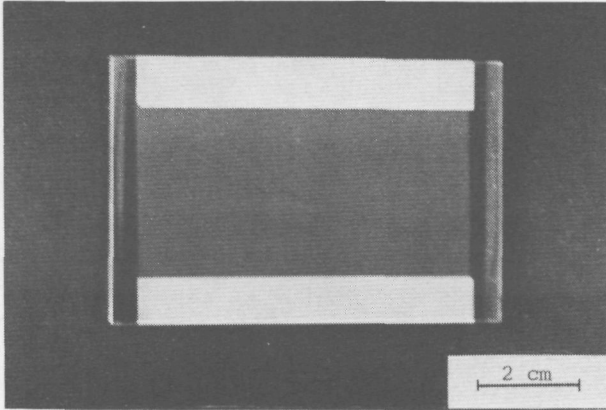
Since we have not succeeded in obtaining appropriate high-voltage resistors, R_1 , R_2 , and R_3 have been built from 15 resistors (1 W maximal power) respectively. Each of these resistors can withstand a potential difference of 1000 V peak, as well as its corresponding dissipation with a maximal current of 1 mA. A similar consideration applies for R_6 .

With the network composed from R_4 , R_5 , and R_6 , one can adjust (lower) the voltage which will, via R_2 and R_3 , be put on the non-central wires. This adjustment facility is part of the attempt to produce a charge distribution as homogeneous as possible at the thermoplastic surface. With two rotary switches, we can select the most favourable voltage combination (cf. Sec. V.1.4).

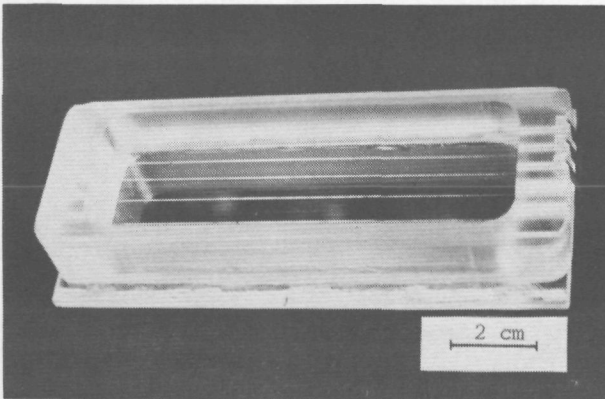
All resistors are mounted inside a box having perspex walls of 5 mm thick, surrounded by a grounded metal cover. The shafts of the two rotary switches have perspex extension pieces, to isolate all high voltage parts of the distributor. It is strongly advisable, however, to rotate the switch only if the high-voltage supply is turned off.

V.1.3. The heat plate

This is a glass plate (2 mm thick) coated with a thin gold layer, against which the flexible film rests during the recording process. The gold coating acts as the ground electrode for the charging stage, also as the heating resistor for the thermal development. The heat plate is mounted at the centre of the camera (see Fig. 5.3). Its size defines the area of the film that is useful in each recording sequence (the recording frame). We use a heat plate with a width of 8 cm to allow a full three-dimensional perception when observing a hologram (matched to the eye distance). Such a heat plate is shown in Fig. 5.7; the shining strips along its longer edges are (thick) gold contacts for electrical connection of the plate to the rest of the system. Some considerations on its conductive coating will be given in Sec. V.4.4.

Fig. 5.7. The heat plate.*V.1.4. The charger unit*

This unit consists of a perspex frame, within which five thin wires are spanned parallel over a length of 10 cm, see Fig. 5.8. There are three groups (the central wire, the two wires adjacent to the centre, and the outer wires) which are separately connected to the cables leading to the high-voltage distributor.

Fig. 5.8. The charger unit.

The frame is mounted such that one of its sides faces the film surface. The other side is covered with a glass plate having a transparent In_2O_3 conductive coating which is grounded. This coating, both assures that the high voltage is restricted to the interior of the unit, and enlarges the charging current. This is because during charging, a practically constant potential

difference exists between the corona electrodes and the grounded In_2O_3 layer. Some ions are continuously released by this potential difference, and those free ions will contribute to the charging current. Without such a conductive layer, the increase of the potential at the charged thermoplastic surface will reduce the current considerably.

We have measured the corona current distribution over the film plane (in the direction perpendicular to the wires). To this end, nine copper strips, each of 2 mm width, were glued equidistantly upon a glass plate, placed in a position identical to that of the heat plate; the strips are then parallel to the corona wires. Each of the copper strips was grounded via a 100 k Ω resistor, thus assuring that they are equally loaded. A high-input resistance millivoltmeter measured the voltage drop across each resistor, indicating the corona current flowing through each strip, see Fig. 5.9.

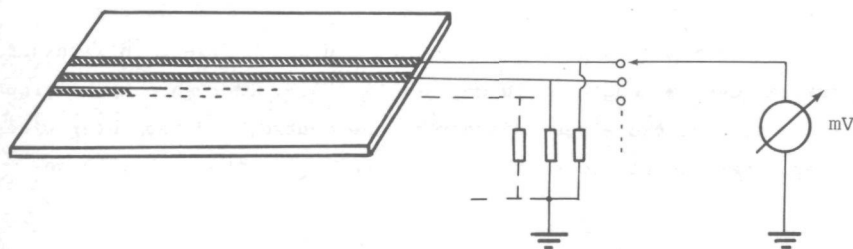


Fig. 5.9. Set-up for measuring the current distribution of the charger unit.

The current distributions for various configurations of the charger unit have been obtained in absence of the photothermoplastic film. In fact, we have also tried to measure the current when the film was present. However, after a few seconds of transient current, the steady state (leakage) currents flowing to the strips mutually differed too little to be distinguished from measurement inaccuracies. This is not very surprising, since after a few seconds of charging, the film surface tends to be fairly equipotential (a possible local potential difference is soon levelled by the continuous corona discharge). The leakage current, depending on the potential difference across the film, is also practically uniform over the film area.

We then concentrated on the current measurements without the film, which required a much lower corona voltage. Nevertheless, the measurements are still relevant to the actual usage, since at the beginning of a charging stage the surface potential of the film is practically zero, such that the initial

currents will, to a certain degree, resemble the distribution measured without the film.

From those measurements, we can observe whether a local peak exists in the charging current distribution. Such a peak, which easily leads to a breakdown, can be avoided by readjustment of the voltages applied to the wires. Moreover, we can observe whether current peaks are present at various places at the film plane with lower values in between. Since the deposited charges play an important role in the adherence of the film to the heat plate, such a spatial inhomogeneity in the charging current usually results in a trapped air bubble between film and heat plate, degrading the thermal contact needed for the development.

The prototype of the charger unit consisted of five stainless steel wires of $150\ \mu\text{m}$ diameter, spanned at an equidistance of $5\ \text{mm}$. The centre wire had a distance of $5\ \text{mm}$ to the film plane, the adjacent to this $6\ \text{mm}$ and the outer wires $8\ \text{mm}$, see Fig. 5.10.a. These different distances to the film plane were intended for minimizing the edge effect (the larger corona current from the outer wires) but, as we can see in Fig. 5.10.b, this effect is not completely eliminated. The current is measured over each $(2 \times 75\ \text{mm}^2)$ of the copper strips. The zero coordinate is the centre-line of the film plane.

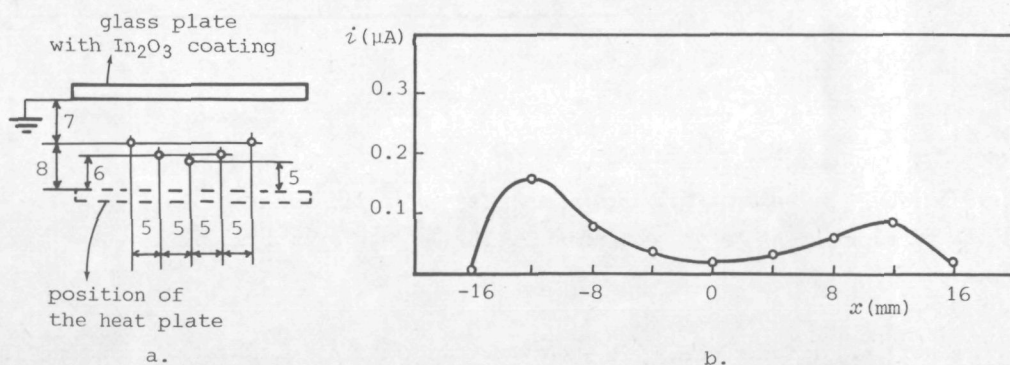


Fig. 5.10.a. Configuration of the prototype of the charger unit.

b. Its current distribution; the voltage at all wires was $6.8\ \text{kV}$.

We have used this charger unit in our preliminary experiments only. Due to its awkwardly high corona onset voltage (about $6.4\ \text{kV}$), this unit has soon been replaced by a more definitive charger unit, which is still in use and which has an onset voltage of $3.18\ \text{kV}$, cf. Sec. III.1.2.

In Fig. 5.11, the configuration and the current distribution of that unit

are depicted. It consists of five Ni wires of 50 μm diameter with a spacing of 5 mm, the distance to the film plane for all wires is (2.7 ± 0.2) mm, while the distance to the In_2O_3 layer of the glass plate covering this unit is 12 mm.

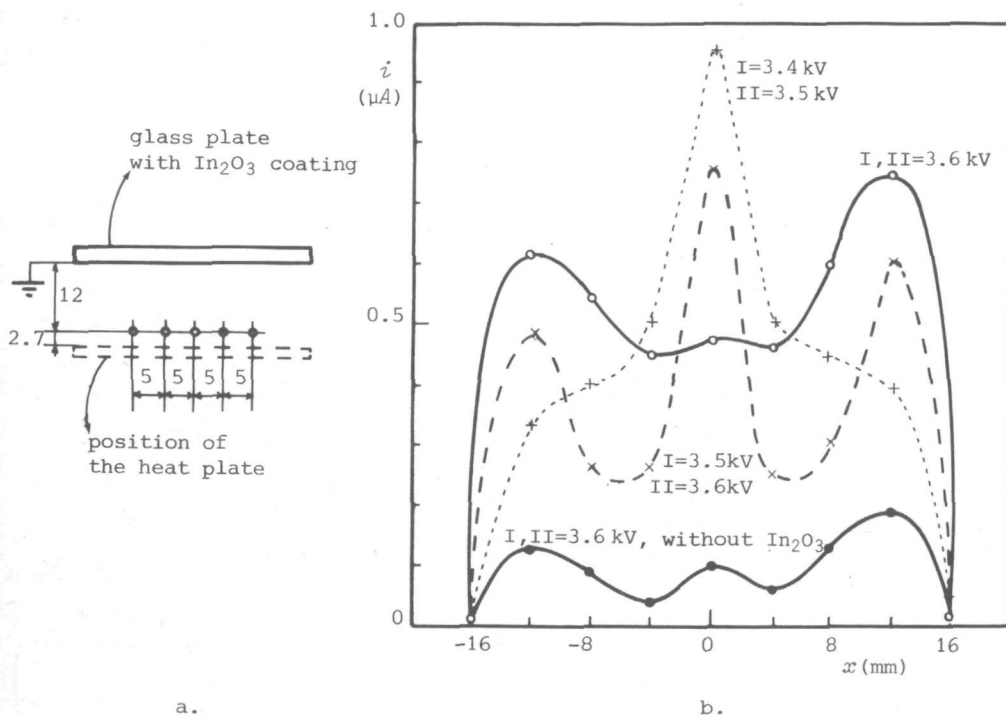


Fig. 5.11. a. Configuration of the definitive charger unit. b. Its current distribution, for several values of the voltages at the outer wires (I) and at the wires adjacent to the centre (II). The voltage of the centre wire is 3.6 kV in all cases.

A very significant change is seen when the glass plate with In_2O_3 coating is removed from the back side of the charger unit. This confirms our considerations early in this Section (Sec. V.1.4). With the In_2O_3 coating, the total current from the corona wires (3.6 kV) to this coating is 0.9 μA .

The present distance of 12 mm between the wires and the In_2O_3 coating is approximately the optimal value. A shorter distance, which increases the charging current further, leads to an electrical breakdown between the wires and the coating. A longer distance reduces the charging current; making the device less efficient.

We also have measured the current distribution for other distances between

the wires and the film plane. In Fig. 5.12, this distance is (3.2 ± 0.2) mm. Apart from a lower current, it is seen that changes of the corona voltage affect the current less significantly than in the case of Fig. 5.11.

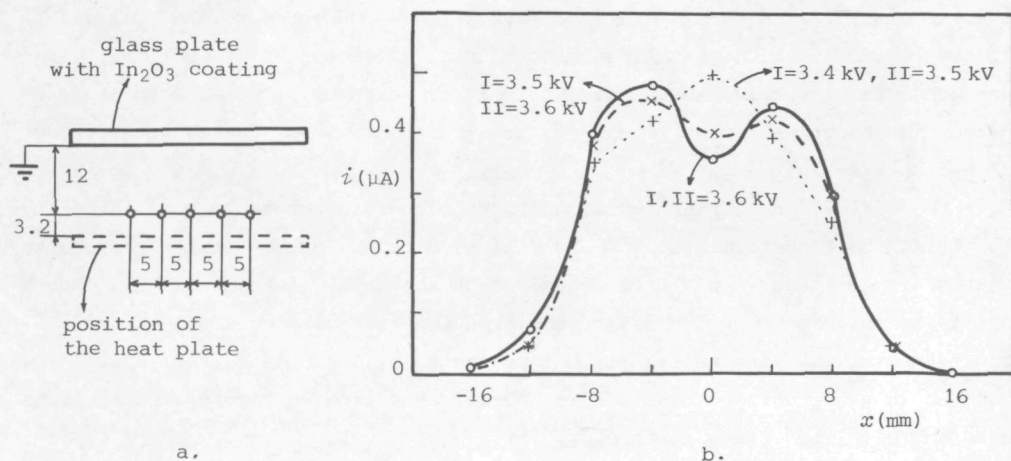


Fig. 5.12.a. Configuration of the modified charger unit, where the distance between the wires and the film plane is increased to (3.2 ± 0.2) mm. b. Its current distribution.

One will obtain a still larger current if the distance is closer than 2.7 mm (cf. Fig. 5.11). However, in experiments we have found that a closer distance leads easily to (local) film damage due to ion bombardment. Hence, the charger unit of Fig. 5.11 is presently the best configuration.

V.2. The shutter

The shutter is of a commercially available electromechanical type. It has a timer unit, from which the shutter can be excited with an adjustable exposure time from $1/25$ to 32 s. Besides this, the shutter can be opened and shut with the aid of external electronic signals. In our system, these signals are provided by the electronic control. For exposure times shorter than 1 s combination of the electronic control and the timer unit is always necessary (see Sec. V.4.1); for longer exposure times and operation of the camera in the manual mode, however, it is not compulsory.

V.3. The high-voltage supply

By regulating the input AC voltage of this supply with a variable transformer (to a maximum of 250 V) we can obtain a high voltage up to approximately 13.2 kV (unloaded), or 12.2 kV when connected to the camera (hence loaded by the high-voltage distributor, cf. Sec. V.1.2). For the charging stage, a value in the range 11 - 12 kV is favourable, as a compromise between a charging current as high as possible and a lower chance of breakdown at the charger unit.

The activation of this supply during the charging stage is carried out by switching the transformer to the 220 V line voltage. To protect the components in the high-voltage supply from transient phenomena and to minimize the chance of electrical breakdown (caused by the transient charging current) at the charger unit, the line voltage is not connected by a simple switch. Instead, we have built a switching circuit, able to raise the line voltage gradually (from zero to full line voltage within 0.75 s).

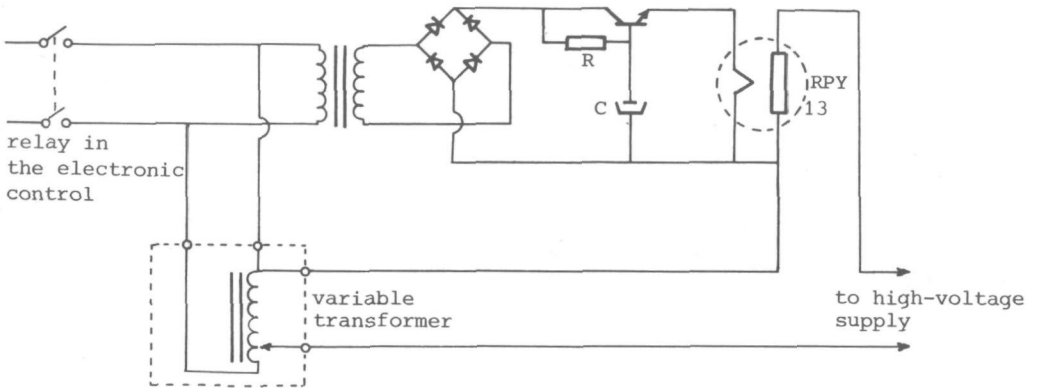


Fig. 5.13. Switching circuit for the gradual start of the charging stage.

A schematic diagram of the circuit is given in Fig. 5.13. The switching is based upon the resistance change of the photo-electric component RPY 13 (two are used in parallel), which reacts upon the light intensity from a filament inside this device. When a relay in the electronic control starts the charging stage, the filament voltage increases gradually in accordance with the charging of the capacitor in a RC network. The filament inside RPY 13 then becomes incandescent, and the resistance in series with the variable transformer is reduced, raising the voltage.

The termination of the charging stage occurs simply by disengaging the relay such that the line voltage will be interrupted directly (no disadvantageous transient appears to be involved during this switching off).

V.4. The electronic control

The working of the whole system is directed from this control device, the front panel of which is shown in Fig. 5.14. Its functions will be considered in greater detail in the remainder of this section.

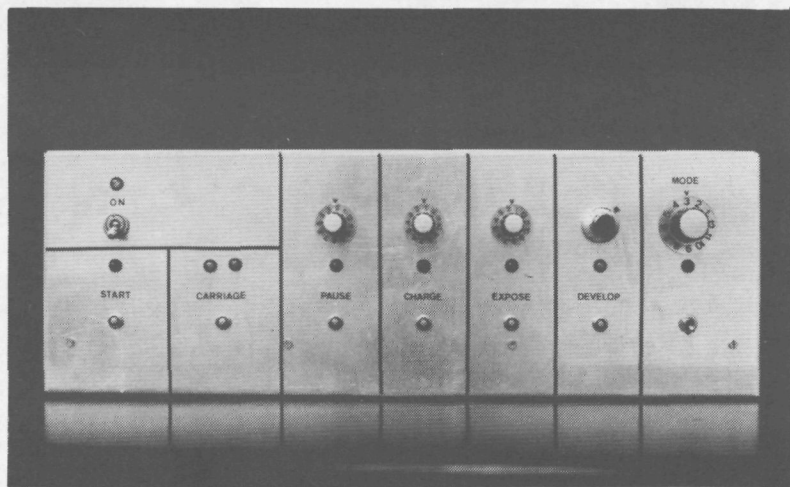


Fig. 5.14. Front panel of the electronic control.

V.4.1. Time duration

The time duration of several stages in the recording process is continuously adjustable.

1. *Charging.* The charging stage is performed while the carriage (with its charger unit) stays stationary facing the recording frame. An advantage of a stationary charging configuration (as compared with the use of a sweeping corona device) is that the corona voltage can start in a somewhat gradual way, reducing the chance of a breakdown caused by transient current peaks,

cf. Sec. V.3.

The time during which the high-voltage supply is activated can be adjusted between 1 and 30 s. The higher the voltage at the corona electrode, the greater the breakdown chance will be, hence the shorter the charging time should be. On the other hand, a prolonged charging can help to attain a more uniform surface potential at the film, since the charges tend to "fill" parts of the surface which have a lower potential than the rest.

2. *Pause.* After charging, the carriage moves to the right part of the camera. Arriving there, a few seconds pause must be allowed for the damping of possible mechanical vibrations (due to the carriage movement) before the exposure can be made. This pause is adjustable from 0.5 to 13 s.

3. *Exposure.* At the electronic control box, the exposure time is adjustable from 1 to 30 s. For shorter exposure times (down to 1/125 s), this part of the electronic control should be used in conjunction with the timer unit of the shutter. It provides then the instruction for opening, while the shutting signal comes from the timer unit.

The duration of the development stage is not adjusted by any timer. Instead, it is regulated by a feed-back scheme, based upon the temperature of the film, see Sec. V.4.4.

V.4.2. *Transport instructions*

This part of the electronic control is meant to regulate the necessary movements, for film transport (sending the carriage to the left part of the camera, winding the film, and bringing the carriage to the centre) and for moving the carriage to the right when the charging stage is finished. This last movement is necessary to prevent a reversed flow of ions from the charged film surface to the corona electrode. Moreover, it renders the film unobstructed during the exposure, though actually the charger unit is transparent (apart from thin electrode wires).

If needed, after exposure and development the carriage can return to the central position. This facility allows one e.g. to perform the recording stages again without first transporting the film (as needed in the double exposure technique).

V.4.3. Execution of a few recording modes

This part has originally been designed to perform the recording stages according to the known techniques like the sequential and the simultaneous methods. During tests with those methods, however, our film turned out to yield a worse response than with the charge-expose-develop technique, while in literature the latter technique is generally quoted as inferior to those other methods. After analysis of the film, it can indeed be explained why our film is not suitable for methods requiring a uniform surface potential during or after the exposure, see Sec. III.3.

Therefore, we have modified this part of the electronic control. Presently, the possible variations of the process sequence are as depicted in Fig. 5.15. Each of these variations can be performed by selecting the proper position of the rotary selector switch, at the right-hand side of the control panel.

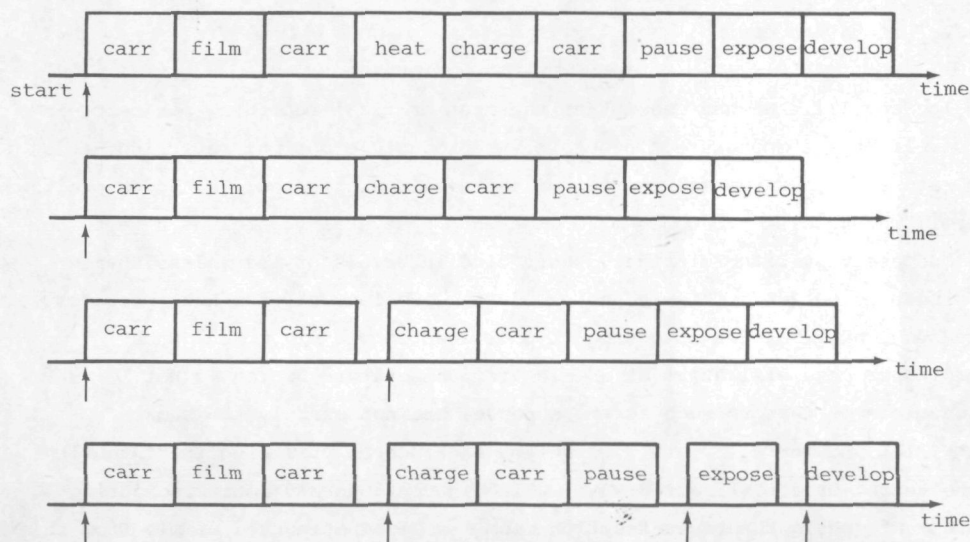


Fig. 5.15. Possibilities of the recording stages. The arrows \uparrow indicate that a corresponding push button must be depressed; "carr" means carriage transport and "film" denotes film winding.

At the first row, two heating stages are involved. The first is prior to charging, the second the actual development stage after exposure. This technique, which has been devised after our own experiences, will be further described in Sec. VI.2. At the second row, one can recognize the conventional

charge-expose-develop method, and like the method at the first row, it is performed automatically by depressing the "start" push button (the push button at the utter left of the control panel). The separation of the recording stages from the film transport is given in the variation at the third row. In this position of selector switch, it is possible e.g. to carry out two exposures on one recording frame, each with its own recording process.

The possibility to perform two exposures successively before development is provided at the fourth row, where almost all functions can be executed separately. It leads to the manual mode of recording (in the process sequence, we must each time depress the corresponding push button). It is also intended for experiments, e.g. for trying out other sequences of the recording stages. It was in this switch position, which has been unmodified since the original design, where we originally developed the technique involving two heating stages represented at the first row in Fig. 5.15.

V.4.4. *Temperature control*

In Sec. III.4 we have seen that the most critical recording parameter is the development temperature. To obtain a reproducible optimal recording, this temperature (or the thermal energy for the development) should be under precise control. The necessity becomes more apparent if several recordings have to be made successively with relatively short time intervals of, say, less than one minute in between. This is because during development, the heat plate is warmed too, and it takes some time to cool down completely. Then, each recording process will start at an elevated temperature, which is not reproducible if factors such as those pauses are not exactly the same.

Killat and Terrell⁸⁴ utilized a feed-back scheme utilizing the intensity of the second-order diffracted wave, which is continuously monitored during development (while the reconstruction beam is illuminating the film). From this intensity, or its time derivative, an electronic circuit decides whether the supply of the development energy should be stopped. The system can be calibrated to yield an optimal first-order intensity.

Another possibility is to measure the film temperature during development, and to interrupt the energy supply when the optimal temperature is achieved. We have applied this method, which is modification of a technique developed by others¹³⁴ (they measured the film temperature before the softening stage). Since the development stage is generally short (about 1 s), and since the film is quite thin (low heat capacity), temperature sensors like thermocouples and thermistors are less suitable. The reason is their usually considerable heat

capacity, so that they do not yield the temperature of the film unambiguously.

Therefore, we have used the conductive layer at the heat plate as the temperature sensor. Its coating has surely some finite heat capacity, but this does not constitute a problem, because the coating acts at the same time as the heat source itself. As another advantage, the measurement involves the whole recording frame, and hence no problem with possible local temperature inhomogeneities, which could induce errors if a point-shape sensor was used, will occur.

The sensing is based upon the change of the resistance with temperature. To this end, a unique and reproducible relation between the material's resistivity and its temperature must be obtained. We have tried to apply an In_2O_3 coating as the conductive layer at the heat plate, in view of its high transmittance and strength (very good adhesion to the glass plate). During tests, however, it turned out that for this material no unambiguous resistance-temperature relation can be established.

In these tests, the glass plate with the In_2O_3 coating, supported on its back side by a 1 cm thick iron block to assure a temperature homogeneity, is placed inside an oven. A thermocouple junction, soldered on a 1 cm² thin metal plate, is clamped against the coated side of the glass plate. The electrical resistance of the coating is measured continuously. The oven is turned on, raising the temperature of the glass plate slowly (from 22°C to 100°C in 35 minutes), and then turned off to let the plate cool down naturally or forced with a blower. Several glass plates, originating from different coating processes, have been measured.

A typical result is shown in Fig. 5.16. The resistance is measured between the two long edges of a 11 × 4 cm² coated glass plate. It is seen that the resistance after a complete heating and cooling cycle is higher than its start value. Suspecting that this was caused by reaction with oxygen from air, we covered the coating with a sheet of our photothermoplastic film (also in order to approach the real situation). No significant change has been observed, even when the film was substituted by a blank glass plate that was tightly clamped to minimize contact between coating and air.

We then baked the coated glass plate at 300°C for 2½ hours to accelerate the probably occurring aging process. After baking, the resistance appeared to be increased to about three times its original value. We repeated the aforementioned resistance measurement procedure. An example is given in Fig. 5.17. Surprisingly, a negative temperature dependence was observed, but it was still not reproducible. No change has also been detected by covering the coating with the film or the blank glass plate.

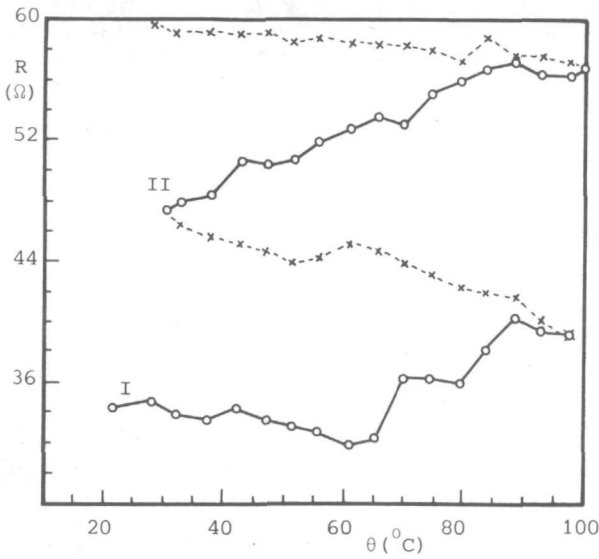


Fig. 5.16. Resistance-temperature relation of a single In_2O_3 layer during two heating and cooling cycles. Circles (o): heating; crosses (x): cooling. I: first run, II: second run.

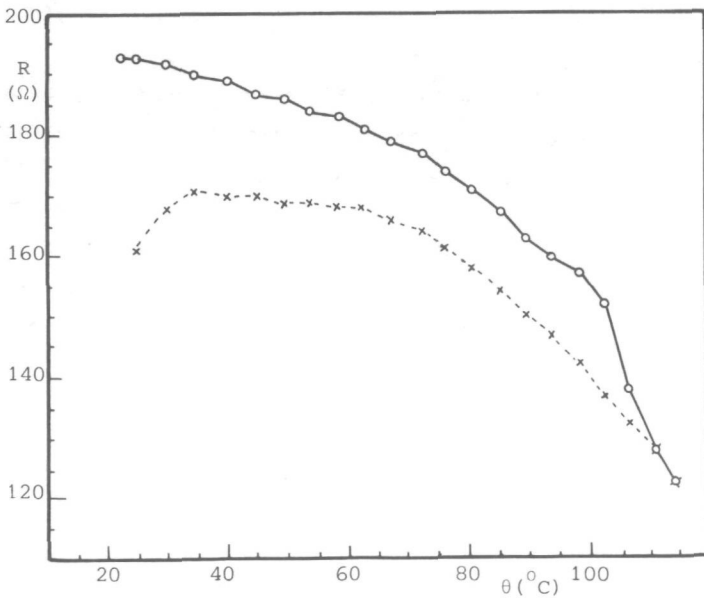


Fig. 5.17. Resistance-temperature relation of an In_2O_3 layer after baking at 300°C for $2\frac{1}{2}$ hours. Circles (o): heating; crosses (x): cooling.

We subsequently stopped the use of an In_2O_3 and proceeded to a gold coating. Originally, we wished to have a $8 \times 5 \text{ cm}^2$ coating upon the heat plate, the thickness of which should be such that its resistance is approximately 140 ohm if measured between its long edges. This relatively high resistance value would be favourable to yield a large (absolute) change with temperature, which makes measurement and control of the development stage easier. However, the maximal resistance across the Au coating turned out to be approximately 50 ohm only (hence, a surface resistance of 80 ohm), above which (i.e. for thinner layers) the coating is no longer stable, cf. Sec. II.1.2. For a layer with a resistance between 30 and 40 ohm, the result of the resistance measurement, using the aforementioned procedure, is depicted in Fig. 5.18.

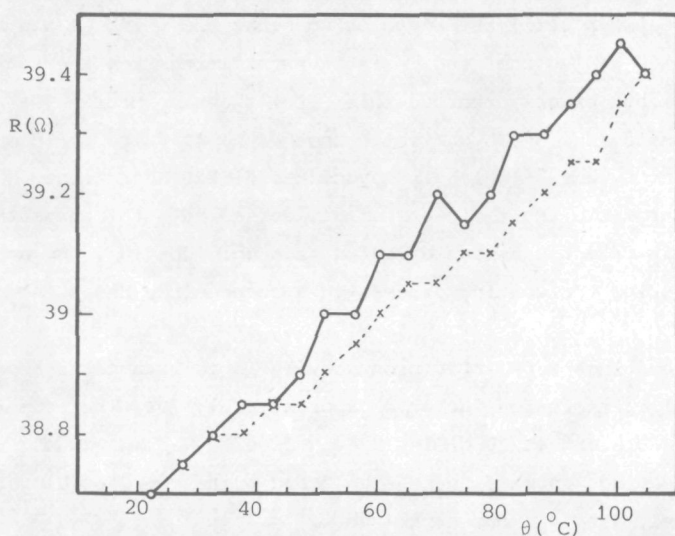


Fig. 5.18. Resistance-temperature relation of a gold layer. Circles (o): heating; crosses (x): cooling.

A more or less unambiguous dependence of the temperature is now established. Using the circuit intended for temperature control of the thermal development (see Fig. 5.19), we have also measured the resistance-temperature relation with the heat plate at its place in the camera. To this end, the heat plate is backed with a metal block with a thermocouple junction inserted in between. The whole unit is covered with a heat insulating material, except for a central area of 2.5 cm diameter where a hot air jet can be blown. An accurately known

voltage (1.20 to 4.00 volt) is given across the Wheatstone bridge of Fig. 5.19. From the output voltage of the measurement circuit, we can find the temperature coefficient of the coating, cf. Eq. (5.3). For a heat plate resistance R_{hp} of 38.7 ohm (at 19°C), a series of both these and the previous measurements yields a temperature coefficient of $(0.211 \pm 0.005) \text{ }^\circ/\text{ }^\circ\text{C}$.

During preliminary use in the recording processes, however, the resistance turned out to increase (by about 2%) every time the film was transported. This is attributed to the weak adhesion of the relatively thin coating to the glass plate, causing part of the layer to be taken away by the film. It even happened if a protecting layer of chiolite had been deposited upon the gold coating. To overcome this problem, thicker coatings have been produced with a resistance of about 22 ohm, and a temperature coefficient (for $R_{hp} = 22.1$ ohm at 19°C) of $(0.307 \pm 0.006) \text{ }^\circ/\text{ }^\circ\text{C}$. An improvement has then be observed.

However, these coatings still seemed to be somewhat too thin. As was the case with R_{hp} between 30 and 40 ohm, the resistance resulting from the coating process appeared to be not exactly reproducible; from the same process, a sample could have a resistance of 26 ohm while another had a value of 18 ohm. This spread in resistance values (which is beyond the direct adjustment capability of our electronic circuit) is presumably caused by a thickness that is not sufficiently far from the unstable region of a gold coating. Any small condition variation during the coating process then changes the resistance considerably.

New, thicker Au coatings were later produced. Their resistance is about 10 ohm with an optical transmission factor of approximately 70%. The temperature coefficient (for $R_{hp} = 9.8$ ohm at 20°C) is $(0.345 \pm 0.007) \text{ }^\circ/\text{ }^\circ\text{C}$. The resistance of these coatings appears to be stable and quite reproducible. These are the layers presently used for our experiments.

The temperature control for the thermal development, Fig. 5.19, is a Wheatstone bridge with the heat plate (R_{hp}) placed in one of its branches. The value of R_a is 1.4 ohm, while the values of the other resistors are respectively $R_b = 100 R_{hp}$ and $R_c = 100 R_a$.

For development, a stabilized voltage difference ($V_s - V_s'$) is applied across the bridge. While the current flowing through R_{hp} heats the photothermoplastic film, the output voltage V_o from the bridge is fed to an amplifier IC₁ and compared (in a comparator IC₂) to a preadjusted reference voltage V_{ref} , which is obtained from a voltage regulator IC₃. When the temperature of the gold coating (and the film) is raised, R_{hp} increases and so do the voltages V_o from the bridge and V_{oA} from the amplifier. As soon as V_{oA} reaches the reference

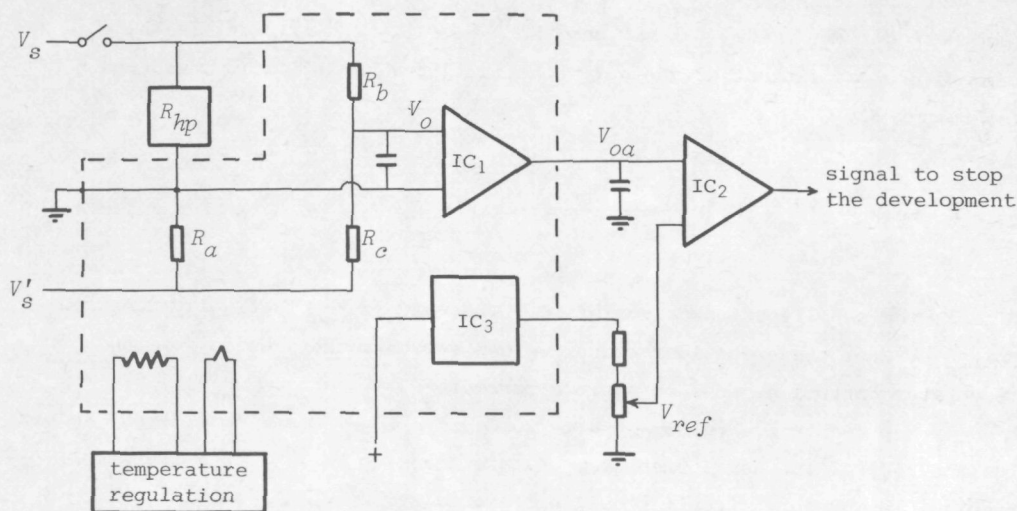


Fig. 5.19. Temperature control for the development stage. The part within the dashed line is a temperature regulated "oven" (see text).

value V_{ref} , the comparator emits a signal which, through other circuits, interrupts the supply ($V_s - V_{s'}$) and terminates the development stage. V_{ref} is first adjusted, by trial and error, such that the development is optimal.

The output voltage V_o from the Wheatstone bridge is given by

$$V_o = (V_s - V_{s'}) \frac{R_{hp}}{R_{hp} + R_a} - \frac{R_b}{R_b + R_c} \quad (5.1)$$

The values of R_a and R_b are chosen to obtain a vanishing V_o at a certain temperature θ_1 of the heat plate (e.g. the room temperature). At temperature $\theta_2 = \theta_1 + \Delta\theta$, the resistance R_{hp} will have increased to $R_{hp} + \Delta R_{hp}$. Since the resistance change ΔR_{hp} is small (the temperature coefficient is only 0.345% per $^{\circ}\text{C}$ and the representative temperature increase is 50°C), the voltage V_o can be written as

$$\begin{aligned} V_o(\theta_2) &= V_o(R_{hp} + \Delta R_{hp}) = V_o(R_{hp}) + \frac{\partial V_o}{\partial R_{hp}} \Delta R_{hp} = (V_s - V_{s'}) \frac{R_a}{(R_{hp} + R_a)^2} \Delta R_{hp} = \\ &= (V_s - V_{s'}) \frac{R_a R_{hp}}{(R_{hp} + R_a)^2} \times c_T \times \Delta\theta \quad , \quad (5.2) \end{aligned}$$

remembering $V_O(R_{hp}) = V_O(\theta_1) = 0$ and where $c_T = (1/R_{hp})(\Delta R_{hp}/\Delta\theta)$ is the temperature coefficient of the gold coating. After amplification, we obtain at the output of IC₂

$$V_{Oa}(\theta_2) = (V_S - V_S') \frac{R_a R_{hp}}{(R_{hp} + R_a)^2} \times c_T \times F_A \times \Delta\theta \quad , \quad (5.3)$$

with F_A the amplification factor of IC₂. The voltage V_{Oa} is finally compared to V_{ref} . From these considerations, we can see that the accuracy of the temperature control depends on various parameters.

If representative values of $\theta_1 = 20^\circ\text{C}$ and $\theta_2 = 70^\circ\text{C}$ are considered, and if the accuracy of the development temperature needs to be 1°C , then the error from the measurement circuit should not exceed 2%.

We consider the temperature coefficient as an inherent property of the gold coating and therefore assume that its value does not vary during a reasonable usage period (the errors indicated in the previous values of c_T were the measurement inaccuracies).

A slight difference in the value of $(V_S - V_S')$ occurs between the unloaded condition and when the heating current is drawn from it. However, once the (practically constant) current flows, the voltage difference remains constant, so that in Eqs. (5.1) - (5.3) the value of $V_S - V_S'$ for the loaded power source can be inserted. Its DC variation is less than 0.5 volt for $(V_S - V_S') = 55$ volt (the contribution of remanent 50 Hz variation is filtered away by the capacitors shown in Fig. 5.18).

An error can be introduced by R_a due to a change in its temperature. This change is caused by heating effect of the development current, and by variation in the ambient temperature. To reduce this heating effect, the value of R_a is kept low. Moreover, it is constituted by two carbon resistors (negative temperature coefficient) in series, R_{ac} , connected parallel to two wire-wound resistors (positive temperature coefficient) in series, R_{aw} . The total resistance is given by

$$R_a = \frac{R_{ac} R_{aw}}{R_{ac} + R_{aw}} \quad , \quad (5.4)$$

and its change due to a temperature change $\Delta\theta_a$ is equal to

$$\Delta R_a \approx \frac{\partial R_a}{\partial \theta} \Delta \theta_a = \frac{R_{ac} R_{aw}}{(R_{ac} + R_{aw})^2} (R_{ac} c_{Tw} + R_{aw} c_{Tc}) \Delta \theta_a \quad (5.5)$$

where c_{Tw} and c_{Tc} are the temperature coefficient of the wire-wound and the carbon resistors, respectively. We use carbon resistors having $c_T = -0.3^\circ/100$ per $^\circ\text{C}$ and wire-wound resistors with a mean c_T of $0.11^\circ/100$ per $^\circ\text{C}$. Hence, by selecting $R_{ac}/R_{aw} = 3/1.1 = 2.7$, the total temperature coefficient $(R_{ac} c_{Tw} + R_{aw} c_{Tc})$ can be made to approach zero.

The remaining source of error, the variation of the ambient temperature can, besides affecting the value of R_a (now much less significantly), also induce drift in the amplifier IC_1 and in the reference voltage generator IC_3 . To eliminate these errors, each of these components is placed in a small container, which is warmed and temperature regulated at a constant value of $(40 \pm 0.5)^\circ\text{C}$. Due to this small "oven", after the apparatus is switched on, before taking holograms about 10 minutes should be allowed to let the temperature in the container become stable.

We have experienced that the temperature control for the development works very satisfactorily. Once the reference voltage (hence the development temperature) has been adjusted, a series of 25 holograms can be made successively without significant change in their quality. After that, the reference voltage should be raised slightly. This change is caused by a small increase (about 1%) in the resistance of the heat plate due to the wear of the coating by the repeated film transport.

VI. SOME EXPERIMENTS WITH THE FILM AND THE CAMERA SYSTEM

VI.1. The effects of the development time

The most critical factor at the development stage is the film temperature or the needed thermal energy, see Sec. III.4. However, these factors depend also on the time during which the development stage is carried out. In this section, we consider the effects of the development time on three factors, i.e. the needed energy, the needed development temperature, and the obtained diffraction efficiency. In these discussions, the film is always at room temperature $(21 \pm 1)^\circ\text{C}$ before development (in Sec. VI.2, the development starts at an elevated temperature of the film).

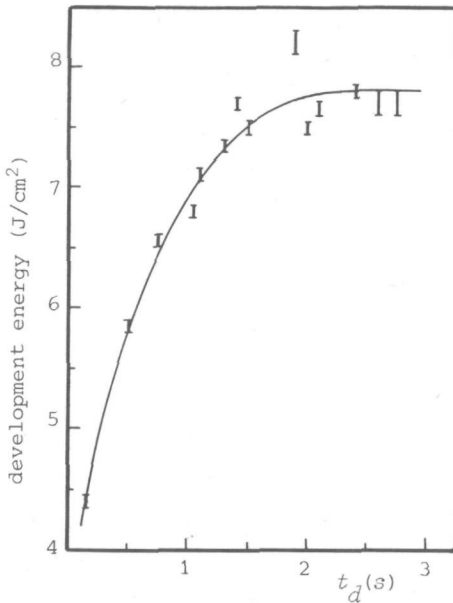
VI.1.1. Development energy

The needed thermal energy is supposed to be linearly related to the electric energy fed to the heat plate. In Fig. 6.1, the electric energy required to achieve an optimal development is depicted as a function of the development time t_d . The measurement for $t_d = 0.15$ s was obtained with the development performed by discharging a capacitor through the conductive layer, see Sec. III.4. The other results have been acquired using our system, by varying the voltage supply for the heating ($V_s - V_s'$ in Fig. 5.19).

It is seen that in the region $t_d \lesssim 1.9$, the required energy increases with longer development times. The cause lies in the substrate as well as in the heat plate, which have a higher heat capacity than the thin thermoplastic layer. With longer development times, more energy is absorbed by this substrate and the heat plate. Hence, in order to arrive at the same range of development temperatures θ_d (θ_d varies also somewhat with t_d , see Fig. 6.2), a longer development time requires a higher thermal energy⁷⁹.

The flattening of the curve in Fig. 6.1 at $t_d \approx 1.9$ s is attributed to the time required by the heat to penetrate from the conductive layer into the heat plate. Studying the problem concerning heat transfer, Eckert and Drake¹³⁵

Fig. 6.1. Development energy as a function of the development time.



have considered a solid substance with a flat surface, which initially has a uniform temperature. At time $t = 0$, a constant heat flux starts to flow through this surface into the material. Then, the distance covered by the heat (the penetration depth d_p) is given by

$$d_p(t) = 2.81 (\alpha_T t)^{1/2} \quad , \quad (6.1)$$

where α_T is the thermal diffusivity of the material and t the elapsed time.

In our case, the heat is generated by the current resulting from a constant voltage difference. Since the relative resistance change due to the temperature raise is negligibly small (the temperature coefficient of the conductive layer is 0.345% per $^{\circ}\text{C}$, see Sec. V.4.4), the current is practically constant and so is the dissipated heat. Hence, we can apply Eq. (6.1). Inserting $d_p = 2.2$ mm (the thickness of the heat plate used in these experiments) and $\alpha_T = 3.4 \times 10^{-7}$ m²/s for a glass plate¹³⁵, the time required by the heat to arrive at the back side of the plate is equal to $(2.2 \times 10^{-3}/2.81)^2/(3.4 \times 10^{-7}) = 1.8$ s, which is very near to the observed time of 1.9 s for the levelling of the curve, see Fig. 6.1.

The situation at $t > (1.8 - 1.9)$ s is difficult to formulate mathematically. For instance, the temperature change at the back surface of the glass plate

should now be taken into consideration. We remark that above 1.8-1.9 s, no extra energy (over the amount needed for 1.9 s) is needed to raise the temperature of the heat plate, or part of it, all the way from room temperature. A kind of saturation effect occurs, which leads to the flattening of the curve in Fig. 6.1.

VI.1.2. Development temperature

In our experiments, the temperature θ_d to achieve the optimal development has been calculated from the needed reference voltage (hence, the output voltage) of the temperature control, see Fig. 5.19 and Eq. (5.3). The change of this development temperature θ_d with the development time t_d is shown in Fig. 6.2.

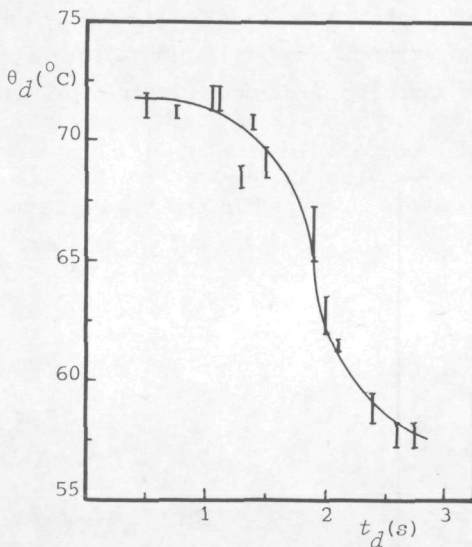


Fig. 6.2. Development temperature as a function of the development time.

It is seen that θ_d depends on the time during which the film is heated; this is in agreement with the observations made by other authors³³. This is because, when the development time is short, a higher temperature must be provided to make the thermoplastic material soft enough to deform quite fast.

The inflection of the curve at $t_d \approx 1.9$ s is related to the levelling of the energy in Fig. 6.1. The cause is that when t_d is longer than 1.9 s, the heat plate has been heated such that directly after the termination of the heating current, the film remains at an elevated temperature, causing the

deformation process to continue to some degree. On the other hand, when $t_d < 1.9$ s, the development must solely rely on the heat from the conductive layer; this introduces an extra requirement for a higher temperature (apart from the requirement considered in the previous paragraph), which results in a rather sudden change in the curve of θ_d .

VI.1.3. Diffraction efficiency

In Fig. 6.3, one can see the effect of the development time on the diffraction efficiency. The observed change in the efficiency can be explained from the fact that, when the thermoplastic material is heated to its softening temperature, its conductivity increases and the deposited charges begin to leak away. Due to the usually low mobility of the charge carriers, however, the charges need some time to move over a distance that is sufficiently long to lower their contribution to the deformation process significantly. Hence, if the development time is kept short, most charges still play a role in deforming the layer, resulting in a relatively large deformation amplitude.

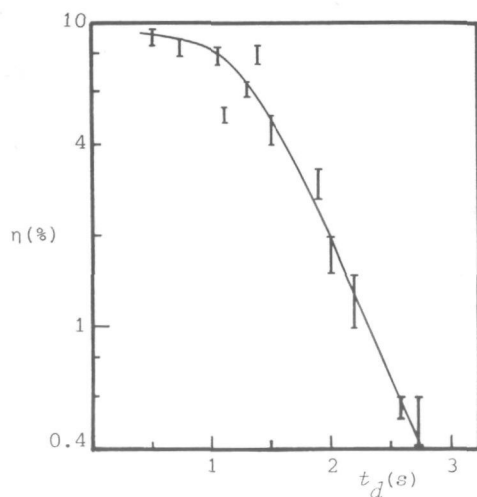


Fig. 6.3. Diffraction efficiency as a function of the development time.

One might expect to have an increasingly high diffraction efficiency at (very) short development times. The maximally obtainable deformation is, however, limited by the recording conditions such as the initial surface potential (which, among others, depends on the performance of the corona device). Hence, for a given system, a maximal value of the diffraction efficiency occurs, as is shown by the levelling of the curve for $t_d < 1$ s

in Fig. 6.3.

The measured efficiency for $t_d = 0.15$ s (for which t_d the energy has been included in the graph of Fig. 6.1), is not depicted in Fig. 6.3. This is because that development time has been obtained⁹⁹ from a different camera system, which produced a diffraction efficiency not higher than 5% if the hologram was recorded and reconstructed with $\Lambda_0 = 632.8$ nm (all other experiments in this Chapter have also been carried out with $\Lambda_0 = 632.8$ nm).

VI.2. Recording method with two heating stages

VI.2.1. The principle

In Sec. III.3 and Sec. V.4.3, we have mentioned that our film is not suitable for the sequential and simultaneous methods, both of which have been reported⁵⁶ to yield a higher diffraction efficiency than the charge-expose-develop method. In our efforts to find some other technique that is appropriate for our film and at the same time produces a higher efficiency, we have carried out experiments in which two heating stages are involved. The first heating (the "preheating stage") taken place just before charging, while the second one is the actual development stage, see the upper row in Fig. 5.15.

Using this technique, we have observed an increase in the diffraction efficiency and a better homogeneity of this efficiency over the recording area, as compared to the charge-expose-develop method. The increase in efficiency can be attributed to two causes, i.e. a shorter development time and a more effective charging process.

We remark that, after the preheating, the absorbed thermal energy remains for some time in the substrate and the heat plate. Then, when the actual development stage starts, the film is at an elevated temperature, which makes that less energy is required to arrive at the development temperature. For a constant heating power, this means a shorter development time, hence a higher diffraction efficiency, see Fig. 6.3.

The other cause, the more effective charging process, follows also from the detained energy in the substrate and heat plate. At the beginning of the charging stage, the film temperature is still fairly high. Then, a relatively large leakage current flows through the film, which in turn causes a large corona current, creating a host of free ions in air. In the subsequent phases of the charging stage, the film has somewhat cooled down, and the leakage

current decreases. The free ions, however, still assist to a certain extent the charging current. This leads finally to a high deposited charge density.

VI.2.2. Leakage current measurements

To detect the increase of the leakage current with temperature, we have attempted to measure this current by clamping a sheet of the film between two plate-shape brass electrodes, see Fig. 6.4. The electrodes with the film were placed upon a resistive heater (electrically insulated with a glass plate), and the whole assembly was then covered by heat insulating material after attaching a thermocouple junction at the lower electrode. The thermocouple wires were connected to a meter that was insulated from the rest of the set-up. The upper brass electrode was connected to the positive output of a variable voltage supply (the negative output was grounded), capable of delivering voltages to a maximum of 3000 V. The lower brass electrode was grounded via a resistor of $10\text{ M}\Omega$. Using a millivoltmeter preceded by a $10\times$ amplifier having a very high input impedance, we measured the voltage drop across the $10\text{ M}\Omega$ resistor. Hence, we could detect small currents down to 0.01 nA , which would produce a voltage drop of 0.1 mV .

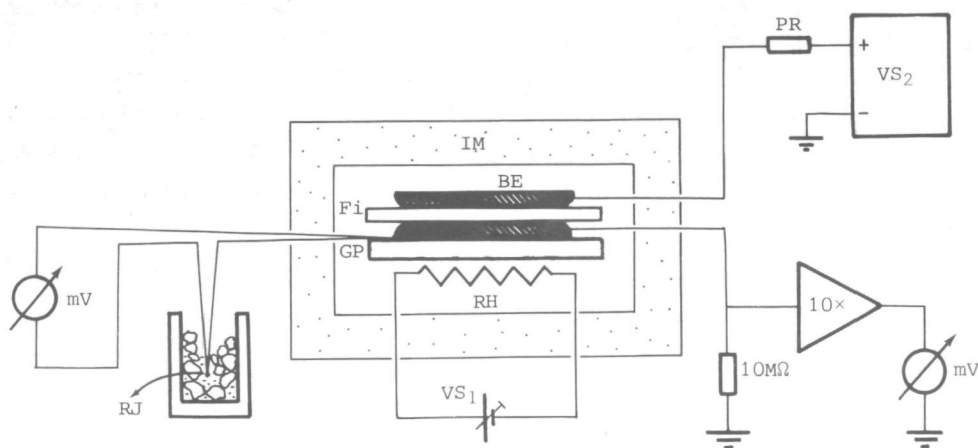


Fig. 6.4. A set-up for measuring the current through the film. BE = brass electrodes, Fi = film, GP = glass plate, RH = resistive heater, IM = heat insulating material, RJ = reference junction of the thermocouple, VS₁ = variable voltage supply (for the resistive heater), VS₂ = variable voltage supply (for the voltage difference across the film), PR = protective resistor.

For an electrode area of $25 \times 10 \text{ mm}^2$, the results are depicted in Fig. 6.4. The asterisks indicate that from that voltage on the current jumped intermittently to a high value (higher than $1 \mu\text{A}$), due to small pulsed discharges (audible as a soft sputtering sound). The current jumps did not damage the film, but further measurements were impossible due to the blocking by the protection circuit of our high impedance amplifier. Such a discharge has been pointed out by other authors¹³⁶ too, and can be attributed to charge injection by the metal electrodes, since such a charge injection governs the conduction through an insulating polymer film¹³⁷.

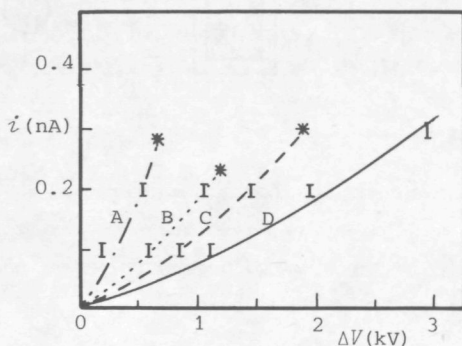


Fig. 6.5. The current through the film as a function of the voltage difference across it, measured with the set-up shown in Fig. 6.4. The film temperatures are A: 50°C , B: 40°C , C: 30°C , D: 21°C .

We then measured the leakage current of the film at its proper place in the camera, the film was charged with our corona device in order to approach the real situation. The back side of the heat plate was covered with a $\frac{1}{2}$ cm thick metal plate to assure a uniform and stable temperature during measurements and then wrapped with heat insulating material, see Fig. 6.6. A thermocouple junction was inserted between the glass and metal plates. From a variable voltage supply, a current was sent to the conductive layer to heat the film and the glass plate. When the measured temperature had reached a required value, we waited for about 10 minutes to let the temperature become stable before the corona voltage was switched on and the measurements were carried out.

The results are shown in Fig. 6.7 (all wires in the charger unit had the same voltage); the result for $\theta = 22^\circ\text{C}$ is comparable to that in Fig. 3.3. The increase of the leakage current with temperature, especially at higher corona voltages, is clearly seen.

In the considered temperature range, the current from the corona wires to the In_2O_3 coated glass plate of the charger unit does not change significantly;

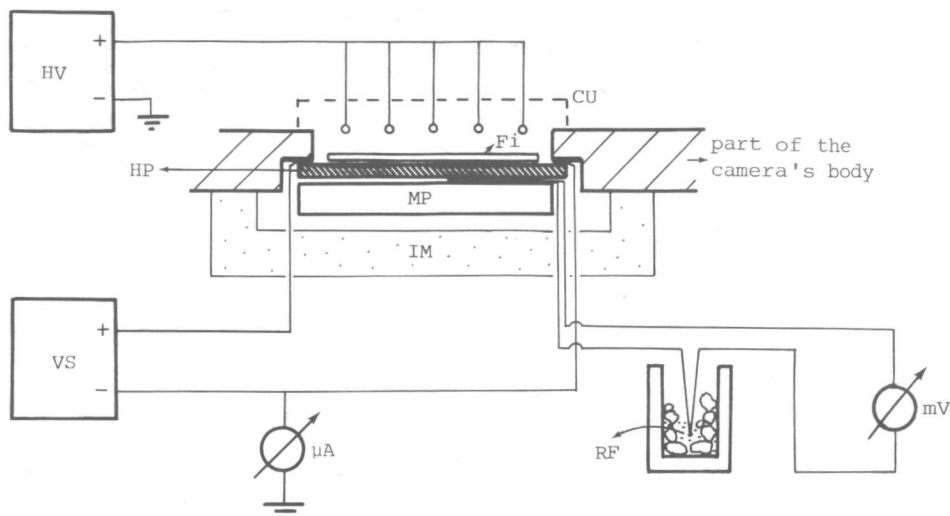


Fig. 6.6. A set-up in the camera for measuring the leakage current. HV = high voltage supply, CU = charger unit, Fi = film, HP = heat plate, MP = metal plate, IM = heat insulating material, VS = variable voltage supply for the heating current, RF = reference junction of the thermocouple.

its value being $45 \mu\text{A}$ at $\phi_c = 10 \text{ kV}$. Hence, the effect of the film temperature on the charging current is practically entirely due to the leakage through the film.

Obviously, the improvement of the charging stage is dependent of the temperature behaviour of the film during this stage as well as between this stage and the development. If the temperature remains high above room temperature, the continuously large leakage current will spoil the deposited charges, while if the temperature is too low to cause a large corona current initially, hardly any improvement can be expected. On the other hand, too low a temperature before development will not appreciably shorten the development time.

In Fig. 6.8, the temperature of the film is depicted as a function of the time until the start of the development, for three values of the preheating time (these are equal to the development time considered in Sec. VI.1); we let the ends of the preheating stage coincide. In these experiments, the duration of the charging stage is 1.5 s, the time for the carriage movement to the right is about 3.5 s, pause 3 s and the (simulated) exposure time is 2 s. The temperatures have been calculated from the output voltage of our temperature control [see Fig. 5.19 and Eq. (5.3)], which has been registered on a recorder.

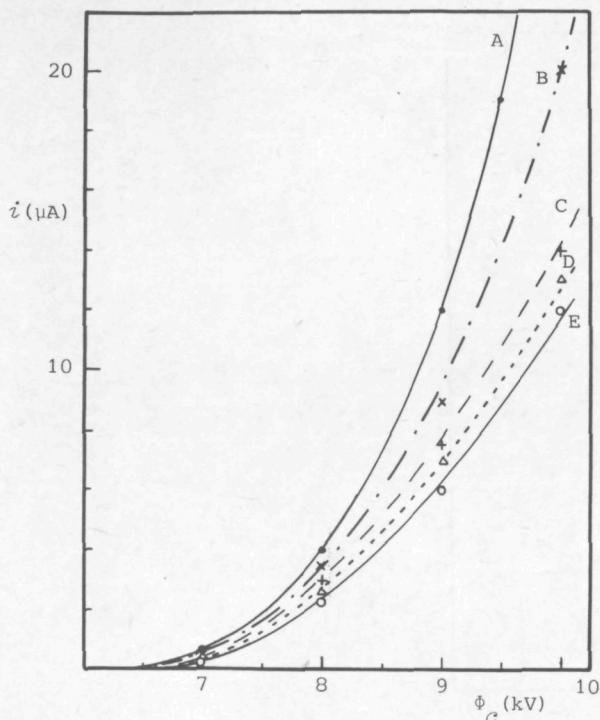


Fig. 6.7. Leakage current through the film as a function of the corona voltage. The film temperatures are A: 60°C, B: 50°C, C: 40°C, D: 30°C, E: 22°C.

In the periods that the heating current does not flow, a low voltage (0.376 V) is put across the Wheatstone bridge in Fig. 5.19, to yield still a (much lower) output voltage but not to warm the conductive layer. For a preheating time t_p of 1.9 s, the development time t_d is about 0.95 s; a preheating time of 1.5 s leads to $t_d = 0.8$ s, while if $t_p = 0.5$ s, we obtain $t_d = 0.3$ s.

VI.2.3. The results from the method

From Fig. 6.8 and from our considerations in Sec. VI.2.1, it can be concluded that the longer the preheating stage, the more obvious the improvement in the charging process and the shortening of the development time will be, both leading to a higher diffraction efficiency.

From Fig. 6.9, one can infer the improvement of the diffraction efficiency for those three values of the preheating time t_p . Indeed, the relative increase of the efficiency is higher if t_p is longer. At $\phi_c = 11.75$ kV, for $t_p = 1.9$ s the increase is from $\eta = 3.25\%$ to $\eta = 6\%$, for $t_p = 1.5$ s the increase of η is from 4.5% to 7.5%, while for $t_p = 0.5$ s, η increases from 8% to 11.5%.

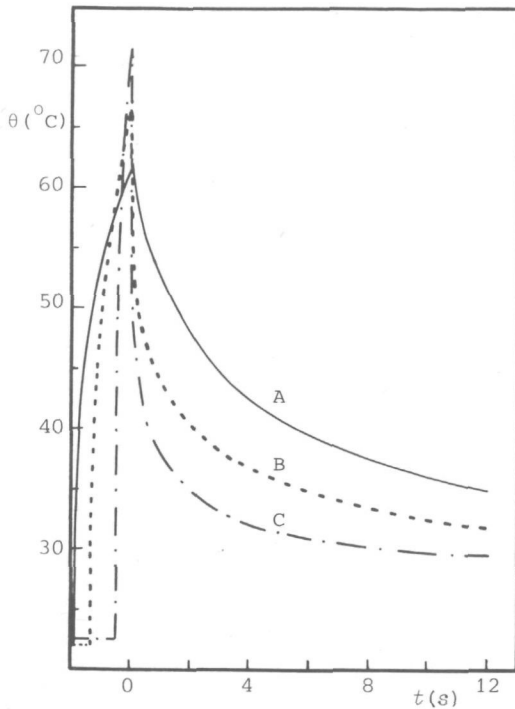


Fig. 6.8. Temperature of the film as a function of the elapsed time t for three values of the preheating time t_p . A: $t_p = 1.9$ s, B: $t_p = 1.5$ s, C: $t_p = 0.5$ s.

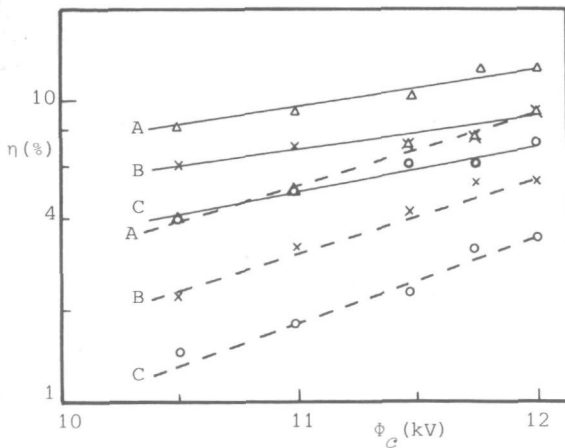


Fig. 6.9. Diffraction efficiency as a function of the corona voltage, from the charge-expose-develop method (---) and from the method with two heating stages (-). Three preheating stages are considered. A: $t_p = 0.5$ s, B: $t_p = 1.5$ s, C: $t_p = 1.9$ s.

We remark that the results with two heating stages at $\phi_c = 12$ kV are not reproducible because of a great chance of a breakdown from the initially large charging current.

Apart from a higher diffraction efficiency, this technique also improves the homogeneity of the efficiency over the recording frame. We have found that the variation of the efficiency over the recording area is now about 15% for $t_p = 1.9$ s, compared to 33% in the usual charge-expose-develop method, Sec. III.4. This improvement follows from the elevated temperature before development, which makes that (parts of) the film need not be heated all the way from room temperature. The smaller temperature difference to be covered allows then a more uniform temperature distribution over the frame area.

A disadvantage of this method is that the exposure is carried out while the film is at an elevated temperature; the film then is slightly expanded as compared with its size at room temperature. When the reconstruction, in e.g. the real time technique of holographic interferometry, is performed at room temperature, a zero fringe condition generally can not be obtained. An example of this is shown in Fig. 6.10. Using the usual charge-expose-develop method, not more than $\frac{1}{2}$ line pair is observed in the real time over a recording area of 30×75 mm². At the same area, 5 line pairs are counted when the method with two heatings have been used ($t_p = 1.5$ s). Both photographs in Fig. 6.10 represent an area of 30×45 mm², i.e. a part of the whole recording area.

We conclude that this method with two heating stages would be appropriate mainly for information display, using systems having originally a relatively long development time, e.g. due to the limited voltage supply to heat a large recording area.

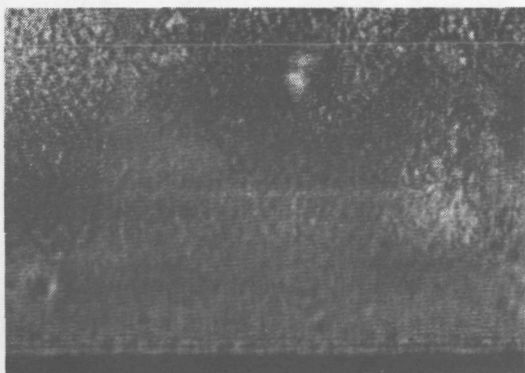


Fig. 6.10.a. Cross section of part of the in the real time reconstructed beam: the recording was made with the charge-expose-develop method.

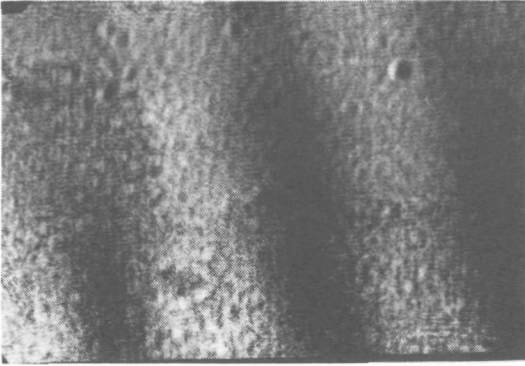


Fig. 6.10.5. Cross section of part of the in the real time reconstructed beam: the method with two heating stages was employed.

VI.3. Spatial wavelength of frost deformation

VI.3.1. Optical arrangements for the measurements

In Chapter IV we have presented a theory of frost deformation. The spatial wavelength of frost deformation following from this theory shows a reasonable agreement with the experimental results of other authors⁸⁴. In this Section we will verify the theory by inspecting the size of frost bubbles obtained with our film.

During experiments, the existence of frost deformation is inspected by looking for a colourful light scattering when the film is illuminated with intense white light. We have found that it is difficult to obtain a clearly observable frost deformation (hence, having not too small amplitudes) if the heating stage is separated from the charging stage.

The results are improved if the film is heated while the charging is continuing (compare the remark^{24, 84} that reproducibility of the results was best with the corona charging kept going during the heating). In fact, we have experienced that with this latter technique and applying a heating temperature between 5 and 10% lower than normal, it is possible to make the frost more pronounced by repeating (a few times, if necessary) the charging and heating. This is because in a subsequent heating with the lowered temperature, the existing frost bubbles are not erased. Instead, they become stimuli of the deformation (see Sec. IV.5.2) that will grow, so that a somewhat larger amplitude than the previous frost is obtained.

After obtaining frost bubbles on the film, several methods are applicable

to measure their spatial wavelength. One of these is to take a microphotograph of a part of the film (see an example in Fig. 2.5), and measure the distance between adjacent ripples in a representative section of such a photograph. Knowing the magnifying factors of the microscope and the photo printer, we can calculate the actual frost wavelength.

Another method is illuminating the film with a perpendicularly incident plane wave of laser light, see Fig. 6.11. The surface corrugation of the film acts as a (quasi-) random phase grating, which diffracts (or scatters, since it is random) the laser light. If we measure the intensity of the scattered light as a function of the scattering angle, we can find the intensity peak which is produced by the predominant frost wavelength. The relation between the scattering angle θ_s of such a peak and the predominant wavelength λ which produces it is given by

$$\lambda = \Lambda_0 / \sin \theta_s \quad , \quad (6.2)$$

where $\Lambda_0 = 632.8 \text{ nm}$ is the laser wavelength in vacuum.

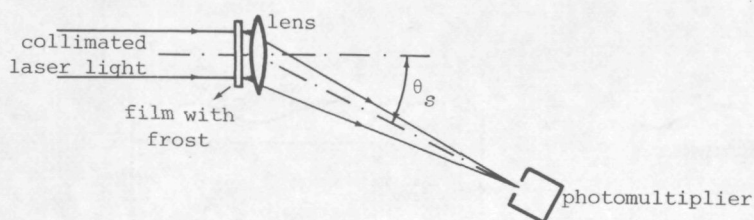


Fig. 6.11. A set-up for measuring the scattered intensity as a function of the scattering angle.

In Fig. 6.12, one can see a typical result of such measurements. We obtain $\lambda = (1.90 \pm 0.25) \mu\text{m}$; then, the ratio to the thickness h of the thermoplastic layer (we use the value $h = 0.5 \mu\text{m}$ mentioned by the manufacturer) is equal to $\lambda/h = (3.8 \pm 0.5)$.

If we inspect the graph between λ/h and a/h for the equipotential model in Fig. 4.6, this result seems to approach the values at the horizontal part of the dashed curve. However, the curve in Fig. 4.6 may not be directly applied to our case. That curve is valid for a film consisting of a substrate and a thermoplastic layer with a conductive sheet in between. There, the deformation can be such large that the surface corrugation touches the conductive layer.

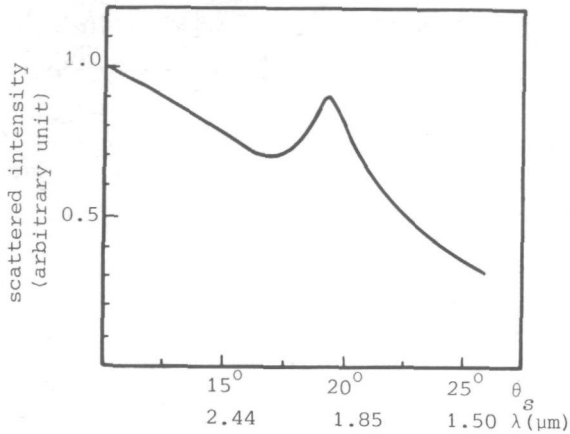


Fig. 6.12. A result of the measurements of the scattered intensity as a function of the scattering angle.

In our case, the deformation amplitude can never exceed the thickness of the thermoplastic layer, which is only a fraction of the whole film thickness consisting of a 50 μm substrate, a 1 μm photoconductor, and a 0.5 μm thermoplastic material, see Fig. 6.13. Hence, only a limited part of the aforementioned curve applies to our case.

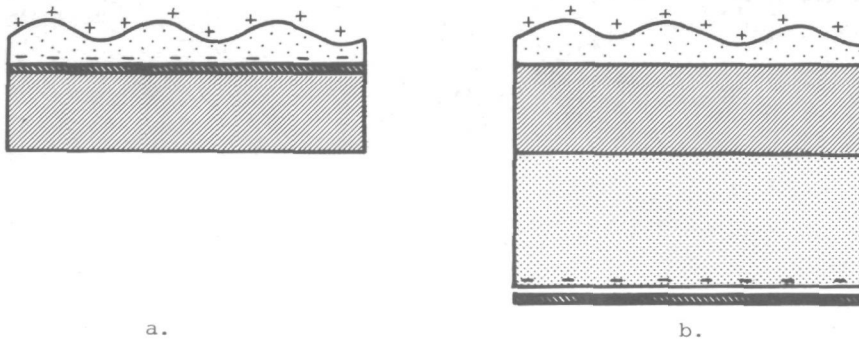


Fig. 6.13. The difference of the boundary conditions between: a. The film considered in Chapter IV, b. The film used in our experiments (see text).

To verify the theory in that limited part of the curve (see later in Fig. 6.21), we need to measure the spatial wavelength as well as the amplitude of the frost deformation. To this end, we have built an interference microscope set-up, see Fig. 6.14.

It is a Mach Zehnder interferometer; the part inside the dashed lines is

a normal microscope, with the mechanical translation facility for moving the observed film and also with low magnification possibilities (using its white light source and its optics) for easily seeking an appropriate part of the film.

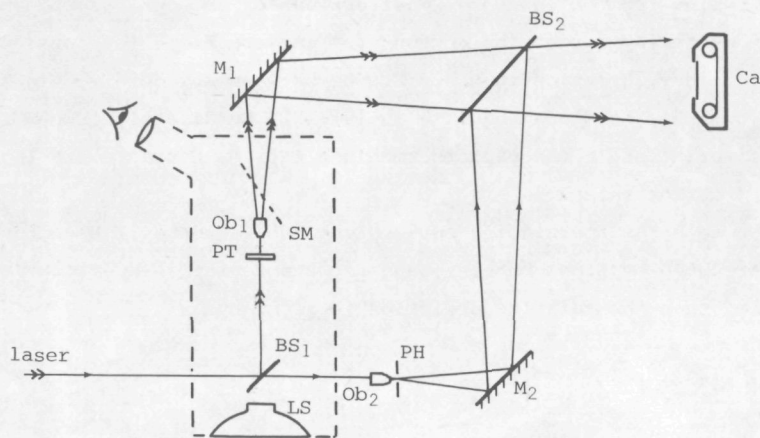


Fig. 6.14. Interference microscope set-up; parts within the dashed line is a normal microscope. LS = light source of the microscope, BS₁, BS₂ = 50/50 beam splitters, Ob₁, Ob₂ = 40× microscope objectives, PH = 10 μm pinhole, PT = photothermoplastic film with frost on it, SM = mirror in the microscope that can be shifted to inspect the object through the eyepiece, M₁, M₂ = mirrors, Ca = camera.

In two arms of the interferometer, two identical 40× microscope objectives are situated at equal optical paths from beam splitter BS₂, such that in the absence of the photothermoplastic film, when the mirrors and beam splitters are properly adjusted, a zero fringe condition is observed at the film plane of the camera Ca. First, the distance between the photothermoplastic film and Ob₁ is adjusted to give a sharp image of the frost bubbles at the film plane of Ca (during this adjustment, the beam from Ob₂ is blocked). This film plane is situated at about 80 cm from the objectives so that (since 40× microscope objective has a 4 mm focal length), a short calculation yields a magnification factor of approximately 200× at the film plane. As usually employed in microphotography, the exact value of the magnification factor can be found by making an exposure of a calibrated scale graduation which is substituted at the place of the photothermoplastic film.

Next, mirror M₂ is deliberately "misaligned" to produce interference

fringes at the film plane. Since the size of the film frame ($24 \times 36 \text{ mm}^2$) in the camera is much smaller than its distance to the microscope objectives, the waves arriving at this frame may be assumed to be plane waves (having some distortion introduced by thickness variation in the photothermoplastic film, for the wave coming from Ob_1 , and by imperfections of the optical components). Then, if we momentarily forget the components' imperfections (we consider them in Sec. VI.3.3), any variation in the distance between the observed interference lines (which ought to be spaced equidistantly) will be directly proportional to the thickness variation in the photothermoplastic film, hence to the local amplitude of frost deformation.

If we denote s_1 as the spacing between the interference lines without the variation introduced by frost bubbles, and δs_1 the deviation due to a peak of a frost bubble, then the relative deviation is given by

$$\delta s_1 / s_1 = (n_1 - 1) a / \lambda_0 \quad , \quad (6.3)$$

where n_1 is the refractive index of the thermoplastic material and a the frost amplitude. In Fig. 6.15.a, one can see an example of the enlarged image of a frosted part of the film (the beam from Ob_2 being blocked). In Fig. 6.15.b, the same part of the film is shown with fine interference fringes produced by those two beams.

At places where the frost deformation shows a broader distance between two adjacent peaks (also having a higher contrast, hence larger deformation amplitude), deviations from straight interference lines can be observed. The deviation, however, is too small to be measured directly with a reasonable accuracy. Applying a higher magnification in the enlargement can possibly facilitate the measurements, but unless we use a large size photographic paper or made many enlargements of various parts of the frosted area, the measurements will be confined to a limited part of the frosted area. Producing a coarser interference pattern with the interference microscope is not advisable, since the line spacing may exceed the frost size, leading to ambiguities in the interpretation.

We have applied a measurement technique based upon the creation of Moiré patterns. It is known^{138,139} that when two patterns, consisting of frequent bright and dark parts, are superimposed, a new pattern (the Moiré pattern) will appear, showing bright and dark parts with generally a greater spacing than in the original patterns. Using this technique, any deviation in the distance between our interference lines will result in a change of the (considerably greater) distance in the Moiré lines. Hence, we can determine the deviations

quite easy and accurately over a broad frosted part of the film.

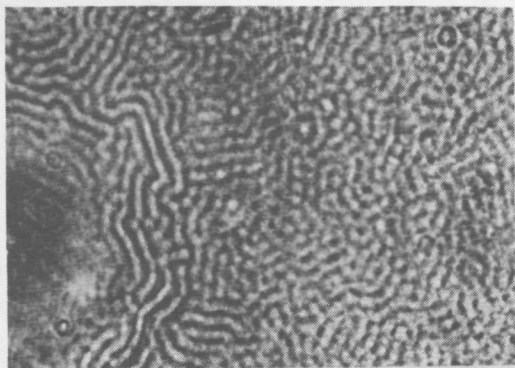


Fig. 6.15.a. Photograph obtained with the interference microscope of Fig. 6.14, the beam from Ob_2 being blocked.

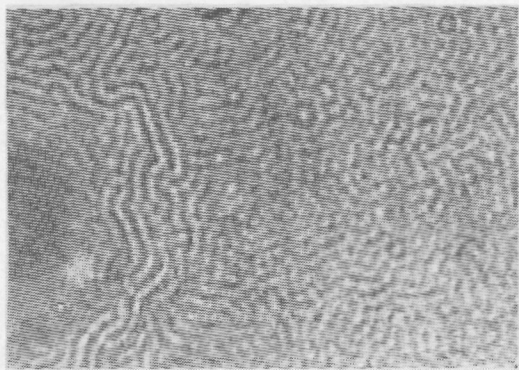


Fig. 6.15.b. Photograph obtained with the interference microscope of Fig. 6.14, the beams from Ob_1 and Ob_2 produce parallel interference fringes.

VI.3.2. Moiré pattern

To enable us to interpret the Moiré pattern, we first consider two patterns, each consisting of straight parallel lines, spaced equidistantly. Let the lines of the first pattern be parallel to the y axis, see Fig. 6.16.a (x and y are two-dimensional Cartesian coordinates in the pattern's plane).

The lines of this pattern can be described by

$$x = L_1 + \mathcal{l}_1 s_1, \quad (6.4)$$

where $\mathcal{l}_1 = \dots, -1, 0, 1, 2, \dots$ is the index number of the lines, starting

from an arbitrarily chosen line, L_1 is a constant such that $x = L_1$ has an index number $l_1 = 0$; s_1 is the line spacing. This pattern describes the interference fringes obtained from our interference microscope, so that we denote already the spacing by s_1 , the same symbol as used in Eq. (6.3).

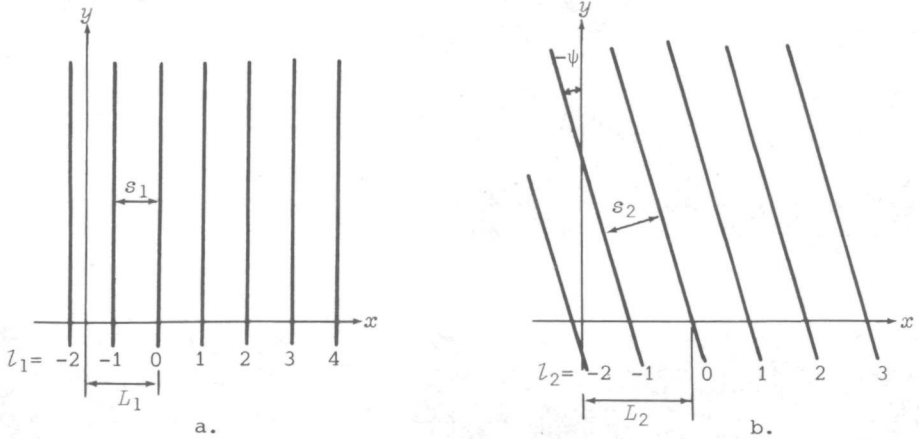


Fig. 6.16.a. A pattern consisting of parallel lines parallel to the y axis, b. A pattern consisting of parallel lines making an angle $-\psi$ with the y axis.

Let the lines of the second pattern make an angle $-\psi$ with the y axis (ψ is a positive number), see Fig. 6.16.b, so that they can be represented by

$$y = -[(x - L_2) \cos \psi - l_2 s_2] / \sin \psi \quad , \quad (6.5)$$

in which $l_2 = \dots, -1, 0, 1, 2, \dots$ is the index number of the lines in this second pattern, L_2 a constant and s_2 the distance between two adjacent lines.

We superimpose these two patterns, with the Cartesian coordinates coinciding. In Fig. 6.17.a the line spacings have been drawn closer to clarify the appearance of the Moiré pattern. The bright lines of the Moiré pattern appear to be the locus of the intersection points between the original lines, see Fig. 6.17.b. In these points we define

$$l_1 - l_2 = l_M \quad , \quad l_M = \dots, -1, 0, 1, 2, \dots \quad , \quad (6.6)$$

l_M being the index number of the resulting Moiré lines.

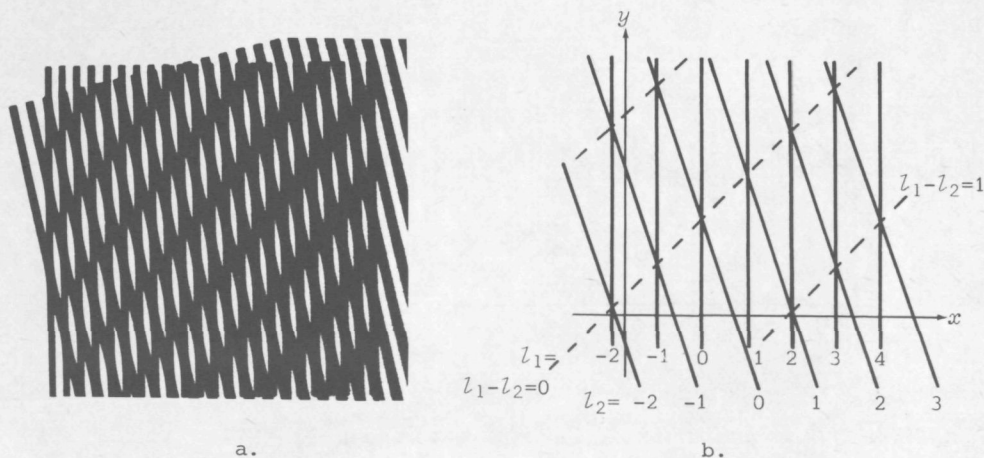


Fig. 6.17. The patterns from Fig. 6.16 are superimposed. a. The line spacings are drawn closer to clarify the appearance of the Moiré pattern; b. On the mathematical description of the Moiré pattern.

From Eq. (6.4), the index number of the first pattern can be written as

$$l_1 = (x - L_1)/s_1 \quad (6.7)$$

and from Eq. (6.5), for the second pattern we have

$$l_2 = [(x - L_2)\cos\psi + y\sin\psi]/s_2 \quad (6.8)$$

so that Eq. (6.6) becomes

$$l_M = (x - L_1)/s_1 - [(x - L_2)\cos\psi + y\sin\psi]/s_2 \quad (6.9)$$

From the latter equation, the equation for the Moiré lines follows as

$$y = [x(\frac{s_2}{s_1} - \cos\psi) - L_1\frac{s_2}{s_1} + L_2\cos\psi - L_M s_2]/\sin\psi \quad (6.10)$$

which represents a set of straight parallel lines, having a slope equal to (cf. Fig. 6.18):

$$\psi_1 = \arctan[(\frac{s_2}{s_1} - \cos\psi)/\sin\psi] \quad (6.11)$$

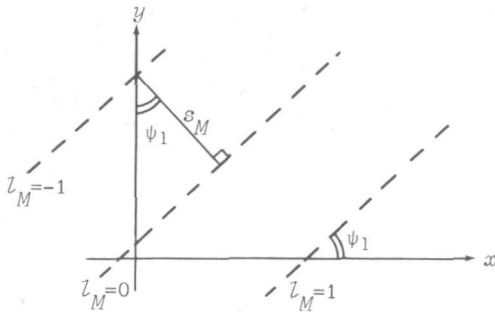


Fig. 6.18. On the derivation of the line spacing s_M .

From Eq. (6.10), the distance between two successive intersections with the y axis is given by

$$y_{l_{M-1}} - y_{l_M} = s_2 / \sin \psi \quad , \quad (6.12)$$

so that inspecting Fig. 6.18 and using Eqs. (6.11) and (6.12), the spacing s_M of the Moiré lines is equal to

$$\begin{aligned} s_M &= (y_{l_{M-1}} - y_{l_M}) \cos \psi_1 = (s_2 / \sin \psi) \times \sin \psi / \left[\left(\frac{s_2}{s_1} - \cos \psi \right) + \sin^2 \psi \right]^{1/2} = \\ &= s_1 s_2 / (s_1^2 + s_2^2 - 2 s_1 s_2 \cos \psi)^{1/2} \quad . \end{aligned} \quad (6.13)$$

The change of s_M due to a deviation in s_1 (this deviation is assumed to be small) can be calculated as

$$\delta s_M = \frac{\partial s_M}{\partial s_1} \delta s_1 = \frac{s_2^2 (s_2 - s_1 \cos \psi)}{(s_1^2 + s_2^2 - 2 s_1 s_2 \cos \psi)^{3/2}} \delta s_1 \quad , \quad (6.14)$$

so that the relative change, with Eq. (6.13), is equal to

$$\frac{\delta s_M}{s_M} = \frac{s_2 (s_2 - s_1 \cos \psi)}{s_1^2 + s_2^2 - 2 s_1 s_2 \cos \psi} \frac{\delta s_1}{s_1} \stackrel{\text{def}}{=} \Gamma \frac{\delta s_1}{s_1} \quad . \quad (6.15)$$

Here, Γ is the proportionality factor with which the relative deviation, Eq. (6.3), is changed and observed as the relative change $\delta s_M/s_M$ of the line spacing in the resulting Moiré pattern.

For the case $s_1 = s_2$, we obtain for Eq. (6.15)

$$\Gamma_{s_1=s_2} = \frac{1}{2} \quad \text{if} \quad \psi \neq 0 \quad . \quad (6.16)$$

This value of Γ of less than unity seems to result in a reduction that might not facilitate the measurements. However, for the case $s_1 = s_2$, Eq. (6.13) reduces to

$$s_M = s_1 / (2 - 2 \cos \psi)^{\frac{1}{2}} \quad , \quad (6.17)$$

which describes a great magnification of s_1 if the angle ψ is kept small. Hence, we can measure the relative deviation $\delta s_M/s_M$ in the Moiré pattern quite easily, and with Eqs. (6.16), (6.15), and (6.3), the amplitude of frost deformation can be determined.

For the case $s_1 \neq s_2$ it is better, in order to eliminate an additional variable, to keep $\psi = 0$, so that we obtain from Eq. (6.15)

$$\Gamma_{s_1 \neq s_2, \psi=0} = \frac{s_2}{s_2 - s_1} \quad . \quad (6.18)$$

We remark that for $s_1 > s_2$, Γ acquires a negative sign. It means that for $s_1 > s_2$, an increase in s_1 leads to a decrease in s_M .

VI.3.3. Measurement results

We have taken several (micro-)photographs like those in Fig. 6.15 of various parts of the frosted area of the film. We have always chosen the parts which contain somewhat inhomogeneities in the frost size (see Fig. 6.15) so that various spatial wavelengths and deformation amplitudes are available. In recording the photographs, the position of the frost inhomogeneities in the recording frame of the camera is always changed. This is in order to reduce the errors due to imperfections of the optical components which might vary spatially over the recording frame.

We have made a recording of the interference fringes in the absence of the photothermoplastic film, too. This recording is then enregistered on a transparent photographic material¹⁴⁰ with the same magnification factor as used

for printing the aforementioned photographs. This transparent photograph is used as the second pattern (see Sec. V.3.2) to be overlaid upon those photographs containing interference fringes, such that the Moiré pattern can be observed (for the case $s_1 = s_2$).

The advantage of using the transparent photograph is the considerable suppression of the errors from components' imperfections, because those imperfections are present in both superposed photographs. The remaining effect of e.g. dust and scratches on the photothermoplastic film is reduced by recording various parts of the frosted area (see our previous remarks).

We also have used a commercially available pattern¹⁴¹ as the alternative second pattern. It consists of parallel lines on a transparent substrate with a slightly greater spacing than our interference fringes (hence, we have the case $s_1 \neq s_2$). Due to the better quality of this commercial pattern, the contrast of the Moiré lines is higher than with the use of the transparent photograph. However, we must consider more measurement points which have to be distributed quite equally over the photographs' area, since the components' imperfections are not inherently compensated here.

In Fig. 6.19, one can see examples of the Moiré pattern, obtained with the transparent photograph ($s_1 = s_2$), and with the commercial pattern ($s_1 \neq s_2$), respectively.

The line spacing as well as its deviations in the Moiré pattern are measured with a vernier ruler. Due to the unsharp boundaries of the lines, the error in measuring the deviations is $\pm 10\%$ if the transparent photograph is used and $\pm 5\%$ if the commercial pattern is involved. The accuracy in determining the line spacing is higher since we can measure over several lines and then divide the measured distance by the number of lines. The errors are $\pm 3\%$ with the transparent photograph and $\pm 2\%$ with the commercial pattern, respectively.

With the transparent photograph, the frost amplitude can be directly calculated using Eqs. (6.16), (6.15), and (6.3). The inaccuracies come from δs_M ($\pm 10\%$) and from s_M ($\pm 3\%$), yielding a total inaccuracy of $\pm 13\%$.

With the commercial pattern, the distances s_1 and s_2 need to be measured, see Eqs. (6.18) and (6.15). The line spacing of the second pattern is 0.391 mm (from the data provided by the manufacturer : 65 line pairs per inch) and 0.392 mm as measured by us using a measuring microscope (a 50 \times microscope having a scale division in its eyepiece). With the same microscope, we have measured the undeviated line spacing s_1 of the interference fringes on the photographs. This spacing turned out to vary slightly over the recording area, from (0.341 ± 0.002) mm to (0.358 ± 0.002) mm. Hence, in calculations,

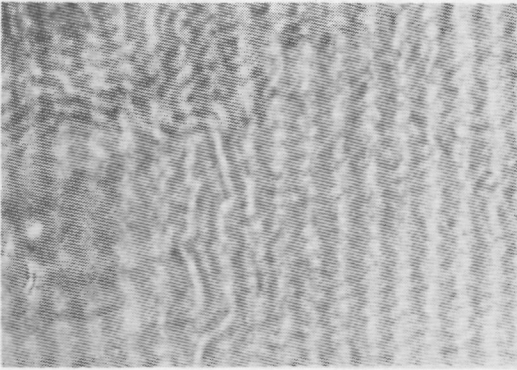


Fig. 6.19.a. The Moiré pattern over the part shown in Fig. 6.15, using the transparent photograph as the second pattern.

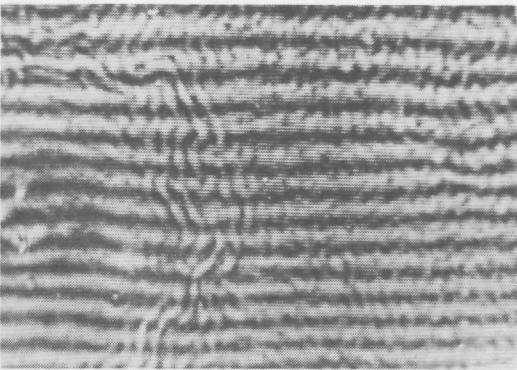


Fig. 6.19.b. The Moiré pattern over the part shown in Fig. 6.15, using the commercial pattern as the second pattern.

attention must be paid to use the *local* value of the line spacing. The value Γ in Eq. (6.18) is then $\Gamma_{s_1 \neq s_2, \psi=0} = (7.75 \pm 5.1\%)$ for $s_1 = 0.341$ mm, and $\Gamma_{s_1 \neq s_2, \psi=0} = (11.69 \pm 7.6\%)$ for $s_1 = 0.358$ mm. With Eqs. (6.15) and (6.3), the amplitude of the frost bubbles can be calculated. The inaccuracies are contributed by δs_M ($\pm 2\%$), s_M ($\pm 5\%$) and Γ (from $\pm 5.1\%$ to $\pm 7.6\%$), yielding a total of $\pm 12.1\%$ to $\pm 14.6\%$.

The spatial wavelengths of the frost deformation have also been measured with the aid of the measuring microscope. The results of those measurements and the subsequent calculations are depicted in Fig. 6.20. The crosses are obtained with a value of 1.6 for the refractive index n_1 , while a value $n_1 = 1.5$ has been used for the circles (the exact value of the refractive index is not known, but will be presumably between 1.5 and 1.6, see also Sec. III.5.1).

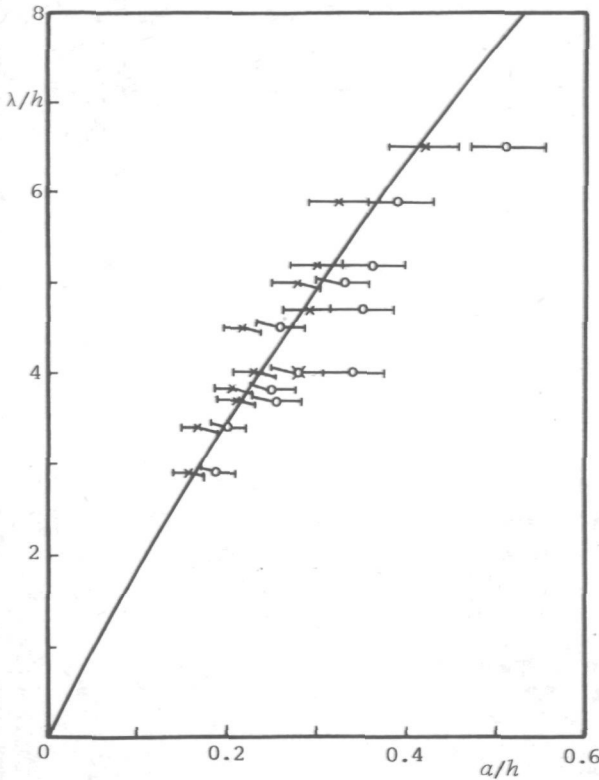


Fig. 6.20. The results of our measurements and calculations crosses (-x-) are for $n_1 = 1.6$ and circles (-o-) apply for $n_1 = 1.5$. The solid line represents the values predicted by the equipotential model of our theory.

The solid line is a transposition from the dashed curve in Fig. 4.6. We remark that when expressed in the thickness parameters valid in our present situation, the graph in Fig. 4.6 should be read as $\lambda/(h+d+s)$ as a function of $a/(h+d+s)$. Hence, if we want to obtain λ/h as a function of a/h for the present case, we must consider the small lower left part of the curve in Fig. 4.6, since $\lambda/h = [\lambda/(h+d+s)] \times [(h+d+s)/h] = 103 \lambda/(h+d+s)$ and similarly $a/h = 103 a/(h+d+s)$ if we insert the values $h = 0.5 \mu\text{m}$, $d = 1 \mu\text{m}$ and $s = 50 \mu\text{m}$.

In Fig. 6.20, the values $\lambda/h = 3.70$, 3.80 , and 4.00 are representative for most of the occurring frost bubbles on our film. Such values appear to result in a peak in the scattered intensity (see Fig. 6.12), which would have caused us to adopt it simply as originating from a unique predominant frost wavelength if the present measurements (and the curve transposition) had not been carried out. Now, we have seen that the frost wavelength depends on the amplitude of deformation such that a certain value of the amplitude corresponds to a certain frost wavelength (compare this to the dashed curve in Fig. 4.6, where a range of values of the amplitude correspond to approximately the same value of the wavelength of frost deformation).

Finally, comparing the measurement results and the dashed line in Fig. 6.20, we can conclude that a reasonable agreement is established between these results and the equipotential model of our theory. Together with the agreement of our model with the value of the predominant frost wavelength measured by other authors^{24, 84} (for films consisting of a substrate and a thermoplastic material with a conductive sheet in between), the results of this Section support the validity of our theory.

VI.4. On the band-pass response of the film

In Sec. II.2.4 and Sec. III.7 we have remarked that a photothermoplastic film has a spatial band-pass response. As more than a single process and more than a single layer are involved in the whole mechanism between the exposure and the readout of the recorded information, one might ask where the band-limiting effect is introduced. In this Section we shall study this from the reconstruction of holograms recorded in such a way that the effect of bandlimitation in the image can be observed.

In our considerations, we assume that the possible origin of the band-limitation lies in the photo-electric transfer and in the deformation process (hence, it does not lie e.g. in the charging stage) and that these processes occur separately from each other (no interaction occurs between them). We assume also that the bandlimiting effect and the linearity behaviour of the processes can be separately considered.

We use an object consisting of isolated bright points, viz., an illuminated diffuse glass plate covered by an opaque cardboard with small holes in it. These bright points are spatially distributed into two groups. One of the groups (we denote it by p_1) is placed in the recording set-up such, that it will be within the *effective* bandwidth of the film. (The bandwidth is defined as the difference between the spatial frequencies where the diffraction efficiency has dropped to 0.5 its optimal value; we use the term "effective" because it includes the frequency response of both the photo-electric transfer and the deformation process.)

The other group of points (p_2) is positioned such, that it is outside the effective bandwidth. Then, in the reconstruction of a linear recording, the point group p_2 will be hardly visible.

Now, let us assume that the photo-electric transfer in the photoconductor has a broad band characteristic such that both point groups p_1 and p_2 are registered in the photoconductor. If the exposure or the reference-to-object

beam ratio is deliberately chosen to make the photo-electric transfer considerably nonlinear (see Sec. III.5.4), the higher order terms of the absorbed intensity distribution will result in intermodulation between the recorded parts of the object (see also Sec. III.5.3). This leads to the formation of (latent) ghost images. Some of the ghost images will be situated in the spatial frequency domain such, that they are within the *effective* pass band of the film. Hence, they will be visible in the readout although the usual image of the points p_2 (outside the effective pass band) is very weak or invisible (see the cases 7 and 8 in Table VI.1, where the ghost images will appear independent of the linearity behaviour of the deformation process).

If, however, the photo-electric transfer is narrowly band-limited (the cases 5 and 6), the nonlinearity of this transfer will not produce ghost images because the point group p_2 has been recorded too weakly to yield a significant

Table VI.1. Probability of observing ghost images if one set of points is within the effective pass band and the other is outside that band

Photo-electric transfer	Spatial frequency characteristic of the photo-electric transfer	Spatial frequency characteristic of the deformation process (the process is linear)	Ghost images are visible: yes or no	Ghost images are visible: (when the deformation process is nonlinear)
linear	band-limited	1. band-limited	no	no
		2. broad band	no	no
	broad band	3. band-limited	no	no
		4. broad band*	no	yes
nonlinear	band-limited	5. band-limited	no	no
		6. broad band	no	no
	broad band	7. band-limited	yes	yes
		8. broad band*	yes	yes

* not occurring experimentally

contribution in the intermodulation.

Briefly, the possibility of observing ghost images is given in Table VI.1. The combination of a broad band photo-electric transfer and a broad band deformation process (see the cases 4 and 8) is only a theoretical one, since it has always been observed that a photothermoplastic film yields a narrow band-pass response. From Table VI.1 it is clear, when no ghost image is observable from a nonlinear recording, the bandlimiting effect must be located in the photo-electric transfer.

The inspection of ghost images should of course occur at the high as well as low frequency sides of the pass band. But first, to enable us to interpret the image unambiguously, we need to know the form of the ghost images. We have used a single point as p_1 (p_1 = the points group within the pass band) and three points, arranged in a triangle, as p_2 (outside the pass band). The distinction in the number of points is in order to facilitate the identification. In Fig. 6.21, the set-up for recording at the high spatial frequency side is sketched.

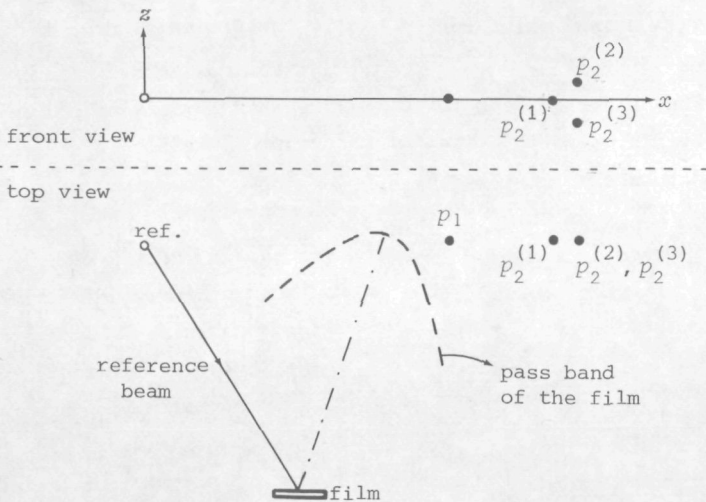


Fig. 6.21. Schematic view of the set-up.

The object points and the point source of the reference beam are located in the same plane, parallel to the film surface; we define x and z as the Cartesian coordinates within this plane. The wave U_0 from the object points interferes with the reference beam and produces interference fringes at the film plane. We denote the spatial frequency of the fringes, corresponding to

the object points, as v_{x_1} , $v_{x_2}^{(1)}$, $v_{x_2}^{(2)} \stackrel{\text{def}}{=} (v_{x_2} + v_z)$, and $v_{x_2}^{(3)} \stackrel{\text{def}}{=} (v_{x_2} - v_z)$, respectively.

If the recording is nonlinear, the transmission factor of the film can be written as a power series of the absorbed intensity distribution, see Sec. III.5.3. In the second-order term, we can find, apart from a factor, the expression $|U_o|^2 U_p^* U_o$, see Eq. (3.60). If the hologram is illuminated with the reconstruction beam U_p , that term yields $|U_p|^2 |U_o|^2 U_o$, which propagates identically to the object wave U_o . We now shall consider the spatial frequency content of $|U_p|^2 |U_o|^2 U_o$.

Remembering that $|U_o|^2 = U_o U_o^*$, where the complex conjugate U_o^* contains the spatial frequencies of U_o with reversed signs, the spatial frequencies contained in $|U_o|^2$ are: $\pm [v_{x_1} - v_{x_2}^{(1)}]$, $\pm [v_{x_1} - v_{x_2} - v_z]$, $\pm [v_{x_1} - v_{x_2} + v_z]$, $\pm [v_{x_2}^{(1)} - v_{x_2} - v_z]$, $\pm [v_{x_2}^{(1)} - v_{x_2} + v_z]$, and $\pm 2v_z$. To obtain the frequency content of $|U_o|^2 U_o$, we must add each of the frequencies in $|U_o|^2$, twelve in total, to each of that in U_o , four in total; this results in forty eight frequency combinations.

We are interested only in those frequencies that lead to ghost images, situated near the true image, and which can be easily identified. Three of them are the frequencies $v_{x_1} - [v_{x_2}^{(1)} - v_{x_1}]$, $v_{x_1} - [v_{x_2} + v_z - v_{x_1}]$, and $v_{x_1} - [v_{x_2} - v_z - v_{x_1}]$. They correspond to three image points in a triangle, which can be obtained by mirroring the original three-point object (p_2) with respect to p_1 , see the crosses (x) in Fig. 6.22.



Fig. 6.22. The appearance of some of the ghost images [the crosses (x)]. The nabla's (∇) are from $|U_o|^2$.

In Fig. 6.22, the nabla's (∇) are *not* the result of intermodulation between the waves from the object points due to nonlinearity, but they are simply generated from $|U_o|^2$, having the frequencies $[v_{x_2}^{(1)} - v_{x_1}]$, $[v_{x_2} + v_z - v_{x_1}]$, $[v_{x_2} - v_z - v_{x_1}]$, and further reconstructed by U_p to yield $|U_o|^2 U_p$. This remark is necessary because we shall encounter such a triangle that is not mirrored with respect to the point object p_1 .

To have a mainly linear recording, an intensity ratio between the

reference and the object beams of 8 : 1 has been chosen (cf. Fig. 3.27), while to obtain a nonlinear recording, the ratio was 1 : 8.

The results at the high frequency side of the film's pass band are shown in Fig. 23.a (the recording was linear) and Fig. 23.b (the recording was nonlinear). In reality, the triangle image at the right-hand side (the reconstruction of the object p_2 outside the pass band) is considerably weaker than the single point image of p_1 . The photographic film used to record the reconstruction has not faithfully reproduced the intensity proportion.

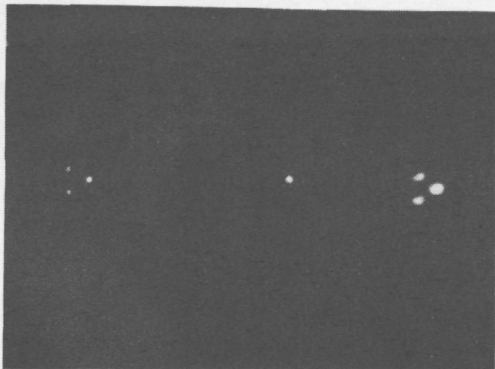


Fig. 6.23.a. Reconstruction from a linear recording at the high spatial frequency side of the film's pass band.

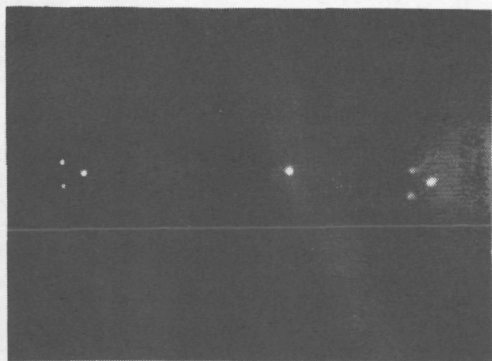
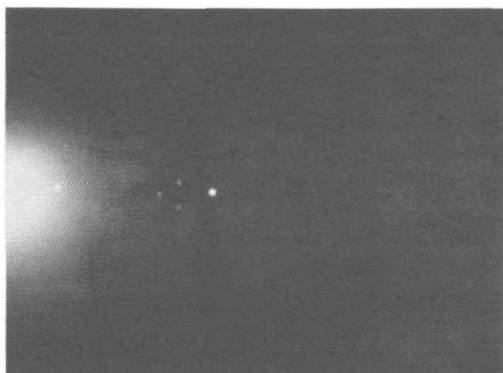


Fig. 6.23.b. Reconstruction from a nonlinear recording.

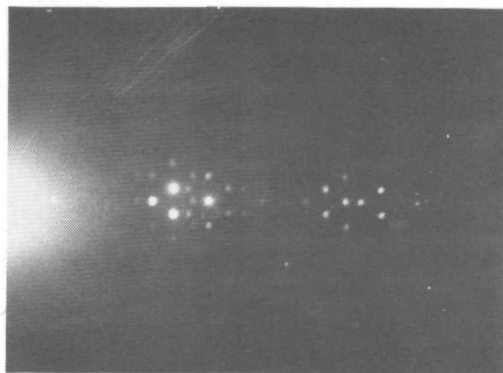
In the nonlinear recording, the mirrored triangle is not observed, too. This suggests that at the high spatial frequency side, the bandlimiting effect is introduced by the photo-electric process (see Table VI.1).

We remark that the ghost, mirrored triangle is invisible while the non-mirrored, also triangular, image from $|U_o|^2$ is observable at the left. This is because $|U_o|^2$ contains the interference between the waves coming from p_1 and p_2 , the difference in frequency of which is within the pass band of the film. The expected ghost image, on the contrary, originates from $|U_o|^2 \cdot U_r U_o$ (see our previous consideration). Hence, it contains the interference between the reference and object waves, which covers a broader spatial frequency.



the erratum

Fig. 6.24.a. Reconstruction from a linear recording at the low frequency side of the pass band. (Below the photograph: configuration of the object points and the reference source at the same scale.)



the erratum

Fig. 6.24.b. Reconstruction from a nonlinear recording.

The results for the low frequency side of the pass band are shown in Fig. 6.24.a (a linear recording) and in Fig. 6.24.b (a nonlinear recording).

The triangle (reconstruction of p_2) is weak and drowned in the light flare from the reconstruction beam. The ghost image (p_2 mirrored to p_1) is seen at the right-hand part of the nonlinear recording. The bright triangle near the image of p_1 originates from $|U_0|^2$. Due to the difference in the object-reference configuration, the direction of the $|U_0|^2$ triangle with respect to p_2 is also different from that in Figs. 6.23.a and 6.23.b (compare also Fig. 6.22 to the drawing under Fig. 6.24.a).

Comparing the reconstructions at the high and at the low frequency sides of the pass band, we can conclude that the spatial frequency response of the photoconductor has a low pass character. This is in agreement with our derivation of the electric potential distribution within the layers, see Sec. III.2.3. In particular, a proportionality factor C always appears in the expressions for the potentials and the electric fields. This factor [see Eq. (3.39)] is given by

$$C = \frac{\sinh k_x(d+s) - \sinh k_x s}{\sinh k_x(h+d+s) + \epsilon_1 \cosh k_x(h+d+s)} \approx \frac{1}{(1+\epsilon_1) \exp k_x h} \quad (6.19)$$

$$(\text{for } k_x s \gg 1, \quad k_x d \gg 1)$$

which can be readily seen to decrease if the spatial frequency, hence k_x , increases.

Finally, we can conclude that, at the low frequency side, the band-limiting effect is introduced by the deformation process. This confirms the remark of some authors¹⁰⁰, that the flow limitation restricts the deformation of the thermoplastic layer at low spatial frequencies.

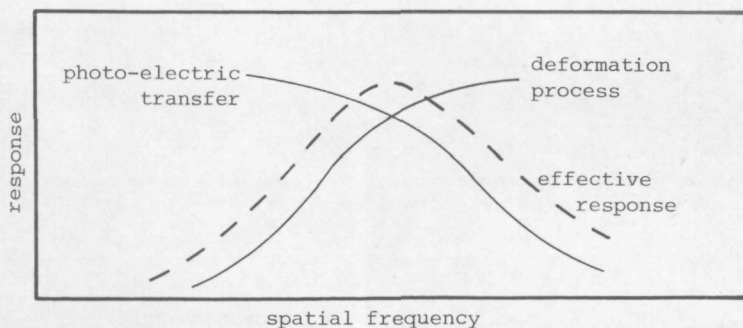


Fig. 6.25. Schematic representation of the spatial frequency characteristic of our film.

We therefore conclude that the band-pass characteristic of our film is obtained from the combination of both phenomena, as sketched in Fig. 6.25.

VI.5. Taking holograms from an extended object with the band-limited film

The spatial band-pass response of a photothermoplastic film would generally not permit its usage to record an object whose extent yields spatial frequencies exceeding the film bandwidth. If an object containing those frequencies is recorded, we shall see in the reconstruction a considerable fading at parts of the object whose spatial frequencies are far from the optimal frequency of the film's response. In this Section, we describe several techniques with which an extended object can still be recorded on the film.

Perhaps the most simple way is to place the object further away from the film, such that the viewing angle of the object (the extent of the object viewed from the film) is decreased until the spatial frequencies it produces fall within the film's bandwidth. However, the reduction of the image size might be objectionable. Moreover, the size of the table, upon which the set-up is mounted, might be limited so that we can not move the object arbitrarily.

If the reduction of the image size is allowable, the same effect of decreasing the viewing angle can be achieved without displacing the object, viz., by mounting a negative lens between object and film. Then, we obtain interference at the film plane between the reference beam and the refracted object beam, see Fig. 6.26.

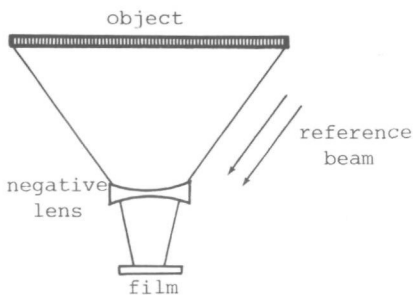


Fig. 6.26. Reducing the viewing angle of the object by utilizing a negative lens.

In our experiments, we used a long, rectangular glass plate with a scale division on it as the object. It was provided with numerals from 0 to 8 over its whole length. In Fig. 6.27 one can see a reconstruction if the recording was taken without lens. The object was placed parallel to the film plane with

the number 4 directly opposite to the film. The viewing angle was 60° and the reference beam made an angle of 35° with the normal to the film. Hence, the spatial frequency at the film plane ranged from 120 to 1700 lp/mm, see Eq. (6.20) (the film bandwidth extends from approximately 500 to 1100 lp/mm, see Fig. 3.30).



Fig. 6.27. Reconstruction from a hologram which was recorded without the negative lens.

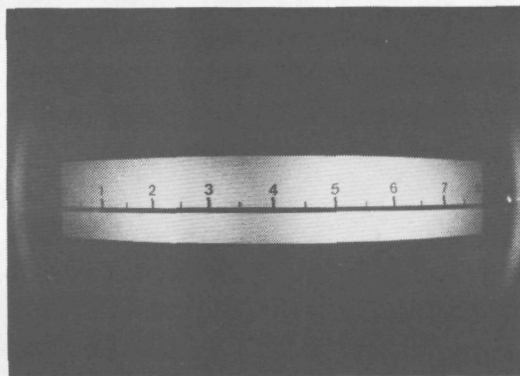


Fig. 6.28. Reconstruction from a hologram which was recorded using a negative lens, see Fig. 6.26.

The result of a recording using a negative lens is shown in Fig. 6.28. A distortion caused by the lens is observable. Apart from a slight fading at both ends of the image, however, the whole extent of the object is clearly reproduced.

Another technique to record the extended object is placing it obliquely with respect to the film plane, see Fig. 6.29. In such a position, with the

reference beam incident from the same side with respect to the film normal, the produced spatial frequencies will be less broad than when the object is parallel to the film plane. This is because the spatial frequency in the x direction (parallel to the film surface) is given by [cf. Eq. (3.10)]:

$$v_x = (\sin \theta'_o + \sin \theta'_r) / \lambda_0 \quad (6.20)$$

The angle θ'_r between the reference beam and the film normal was -10° (negative because the reference beam comes from the same side as the object beam). In this experiment the viewing angle of the object was 50° , viz., the object extended between $\theta'_o = 25^\circ$ and $\theta'_o = 75^\circ$. Hence, it produced spatial frequencies from 390 to 1250 lp/mm. For comparison we remark that, if the object is parallel to the film plane with $\theta'_r = 30^\circ$, the same viewing angle of 50° will contain spatial frequencies from 120 to 1460 lp/mm.

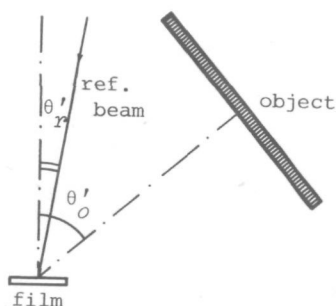


Fig. 6.29. Reducing the range of the produced spatial frequency by placing to object oblique to the film plane.

The reconstruction of a recording is shown in Fig. 6.30. We found that this method is rather clumsy because it is difficult to observe the image at a small angle with respect to the film plane. Moreover, part of the object corresponding to a large θ'_o must be illuminated more intensely, since some loss is introduced by the reflection at the thermoplastic surface. In the reconstruction we have observed a set of faint dark lines over the image: presumably they were caused by interference due to multiple reflections between the conductive layer and the thermoplastic surface.

Still another method is depicted in Fig. 6.31. Two reference beams are employed; we denote their wave functions as U_{r1} and U_{r2} , respectively. We consider two adjoining parts of the object (in our case: the left and the right parts) and denote the waves coming from these parts as U_{o1} and U_{o2} , respectively. The reference beams are arranged such that the interference

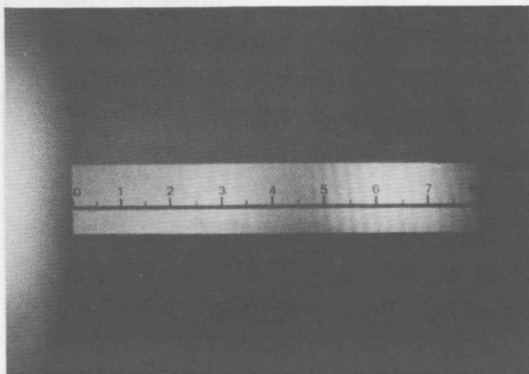


Fig. 6.30. Reconstruction of a hologram recorded with the configuration shown in Fig. 6.29.

between U_{r1} and U_{o1} produces spatial frequencies which are within the film bandwidth, as does also the interference between U_{r2} and U_{o2} . Additionally, we let the angle between the reference beams such large that the frequency of the fringes they produce together is outside the film's pass band. Then, we can record those adjoining parts of the object simultaneously without interaction between the reference beams.

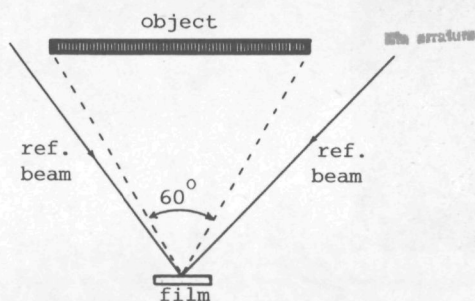


Fig. 6.31. Recording the whole object by employing two reference beams.

The reconstruction of a recording is shown in Fig. 6.32. The viewing angle was 60° (the same as in Fig. 6.27). Note that the reference beams were not both propagating in the horizontal plane through the center-line (scale line) of the object; the propagation direction of the left reference beam made an angle of about 30° with the horizontal plane. This is because each reconstruction beam will make the -1^{st} order image (recorded by the other reference beam) visible. If the reference beams were symmetrically arranged in such a horizontal plane, the -1^{st} order images would be superimposed on the $(+1^{\text{st}}$ order) image of the object, degrading its signal-to-noise ratio seriously. In Fig. 6.32, we can see the -1^{st} order image at the upper part of the photograph.

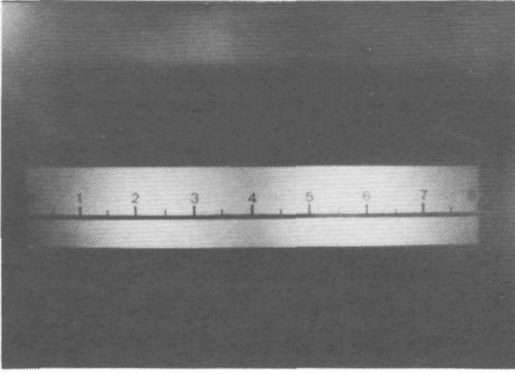


Fig. 6.32. Reconstruction of a hologram, recorded with the configuration shown in Fig. 6.31.

To know which part of the object was recorded by each reference beam, in Figs. 6.33.a and 6.33.b we show the reconstructions, with each time only one of the reconstruction beams illuminating the film.

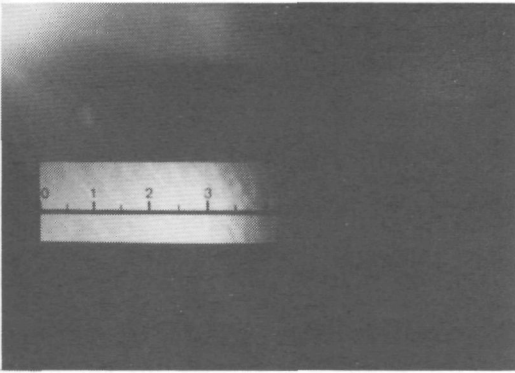


Fig. 6.33.a. Reconstruction of the same hologram as in Fig. 6.32; only the left reconstruction beam is illuminating the film.

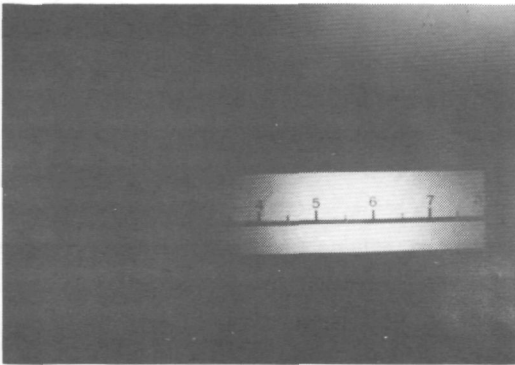


Fig. 6.33.b. Only the right reconstruction beam is illuminating the film.

We finally remark that this method is specially suitable for an elongated object. For e.g. a large square, more than two reference beams will be needed to cover the whole object. However, it will be difficult to arrange the beams, such that no -1^{st} order image is superimposed on the desired image.

APPENDIX A: CONCISE DERIVATION OF THE POTENTIAL DISTRIBUTION IN THE FILM AFTER THE EXPOSURE

Solutions of Laplace's equation, Eq. (3.33), within the layers and in air are given by

$$\phi_{air} = A_0 + A_1 y + [A_2 \exp(-k_x y) + A_3 \exp k_x y] \cos k_x x \quad , \quad (A-1)$$

$$\phi_{tp} = B_0 + B_1 y + (B_2 \sinh k_x y + B_3 \cosh k_x y) \cos k_x x \quad , \quad (A-2)$$

$$\phi_{pc} = C_0 + C_1 y + (C_2 \sinh k_x y + C_3 \cosh k_x y) \cos k_x x \quad , \quad (A-3)$$

$$\phi_{su} = D_0 + D_1 y + (D_2 \sinh k_x y + D_3 \cosh k_x y) \cos k_x x \quad , \quad (A-4)$$

where ϕ_{air} , ϕ_{tp} , ϕ_{pc} , and ϕ_{su} are the potential in air, thermoplastic layer, photoconductor, and substrate, respectively; A_l , B_l , C_l , and D_l are constants, $l = 0, 1, 2, 3$.

In the following account we consider the relations which are obtained by substituting Eqs. (A-1) - (A-4) into the boundary conditions expressed by Eqs. (3.34.a) - (3.34.h).

$$\text{From Eq. (3.34.a):} \quad D_0 = D_1 (h + d + s) \quad , \quad (A-5)$$

$$D_3 = D_2 \tanh k_x (h + d + s) \quad , \quad (A-6)$$

$$\text{from Eq. (3.34.b):} \quad C_0 - C_1 (h + d) = D_1 s \quad , \quad (A-7)$$

$$-C_2 \sinh k_x (h + d) + C_3 \cosh k_x (h + d) = D_2 \frac{\sinh k_x s}{\cosh k_x (h + d + s)} \quad , \quad (A-8)$$

$$\text{from Eq. (3.34.c):} \quad B_0 - B_1 h = C_0 - C_1 h \quad , \quad (A-9)$$

$$-B_2 \sinh k_x h + B_3 \cosh k_x h = -C_2 \sinh k_x h + C_3 \cosh k_x h \quad , \quad (A-10)$$

$$\text{from Eq. (3.34.e):} \quad A_1 = A_3 = 0 \quad , \quad (A-11)$$

from Eq. (3.34.d) and using Eq. (A-11):

$$A_0 = B_0 \quad , \quad (A-12)$$

$$A_2 = B_3 \quad , \quad (A-13)$$

from Eq. (3.34.f): $B_1 = \sigma/\epsilon_1 \quad , \quad (A-14)$

$$B_3 = -\epsilon_1 B_2 \quad , \quad (A-15)$$

from Eq. (3.34.g), using Eqs. (A-14), (A-10), and (A-15):

$$C_1 = (\sigma - \sigma_t)/\epsilon_1 \quad , \quad (A-16)$$

$$C_3 = -[\sigma_t m_\sigma / (\epsilon_1 k_x)] \sinh k_x h - \epsilon_1 B_2 \quad , \quad (A-17)$$

from Eq. (3.34.h), using Eqs. (A-16), (A-8), (A-10), and (A-17):

$$D_1 = \sigma/\epsilon_1 \quad , \quad (A-18)$$

$$B_2 = \sigma_t m_\sigma C / (\epsilon_1 k_x) \quad , \quad (A-19)$$

where C is a factor given by Eq. (3.39).

Insertion of Eq. (A-19) into Eq. (A-17) yields:

$$C_3 = -\frac{\sigma_t m_\sigma}{\epsilon_1 k_x} \frac{(\sinh k_x h + \epsilon_1 \cosh k_x h) \sinh k_x (h+d+s) - \epsilon_1 \sinh k_x s}{\sinh k_x (h+d+s) + \epsilon_1 \cosh k_x (h+d+s)} \quad , \quad (A-20)$$

so that together with Eqs. (A-10), (A-15), and (A-19) we obtain:

$$C_2 = -\frac{\sigma_t m_\sigma}{\epsilon_1 k_x} \frac{(\sinh k_x h + \epsilon_1 \cosh k_x h) \cosh k_x (h+d+s) + \sinh k_x s}{\sinh k_x (h+d+s) + \epsilon_1 \cosh k_x (h+d+s)} \quad . \quad (A-21)$$

Combination of Eqs. (A-7), (A-16), and (A-18) yields:

$$C_0 = (\sigma/\epsilon_1)(h+d+s) - (\sigma_t/\epsilon_1)(h+d) \quad , \quad (A-22)$$

which with Eqs. (A-9), (A-14), and (A-16) results in:

$$B_0 = (\sigma/\epsilon_1)(h+d+s) - (\sigma_t/\epsilon_1)d \quad . \quad (\text{A-23})$$

Hence, all constants of Eqs. (A-2) and (A-3) are known, so that we obtain Eqs. (3.35) and (3.36).

We assume that the exposure energy is such low that the potential difference across the photoconductor, Eq. (3.32), can be written as:

$$\Delta\phi_{pc} \approx \Delta\phi_{pci} [1 - c \Delta\phi_{pci} E_0 (1 + m_I \cos k_x x)] \quad , \quad (\text{A-24})$$

where $\Delta\phi_{pci} = (\sigma/\epsilon_1)d$, see also Eq. (3.4). The potential difference $\Delta\phi_{pc}$ can be calculated using Eq. (3.35), through the relation:

$$\Delta\phi_{pc} = \phi_{pc, y=-h} - \phi_{pc, y=-(h+d)} \quad . \quad (\text{A-25})$$

Equating Eq. (A-25) to Eq. (A-24), we can finally obtain Eqs. (3.37), (3.38), (3.40), and (3.41).

APPENDIX B: DETERMINATION OF THE NUMBER OF SUBAREAS M IN THE DERIVATION OF THE POTENTIAL DISTRIBUTION

From Eq. (4.11), applying first boundary condition (4.13.a) and then boundary condition (4.13.c), the following relation is obtained:

$$A_{3m} \{ \sinh(k[h + a \cos kx_m]) + ak \cosh(k[h + a \cos kx_m]) \} \times \\ \times \cos kx_m = -A_{1m} \sinh kh \quad . \quad \text{the erratum} \quad (B-1)$$

In order to equalize the left- and right-hand sides within a certain accuracy, the number of subareas M within a half wavelength has to exceed a minimal value for which the left hand side can be considered to be constant. Then, x_m can be replaced by its value ξ_m at the edge of the subarea (see Fig. 4.5).

If F_m denotes the factor between the brackets $\{ \}$ in Eq. (B-1), and $\Delta x_m = \frac{1}{2}\lambda/M$ is the width of each subarea, we can define the variation ΔF_m across the m th subarea as $(\partial F_m / \partial x_m) \Delta x_m$. As an example, we consider the case that an accuracy of 5% is required. Then, we must impose

$$|\Delta F_m / F_m| \leq 0.05 \quad . \quad (B-2)$$

Choosing, e.g., $a/h = 0.8$ and $\lambda/h > 0.2\pi$, the minimal value of M equals 486.

REFERENCES

1. Di Chen, J.D. Zook, *Proc. IEEE* 63, 1207 (1975).
2. G.W. Stroke, *Opt. Acta* 16, 401 (1969).
3. A. Vander Lugt, *IEEE Trans. Inform. Theory* 10, 139 (1964).
4. S.H. Lee, *Opt. Eng.* 13, 196 (1974).
5. R.K. Erf, *Holographic Nondestructive Testing* (Academic Press, New York, 1974).
6. G.W. Stroke, *IEEE Spectrum* 9, 24 (1972).
7. K. Biedermann, *Opt. Acta* 22, 103 (1975).
8. J. Bordogna, S.A. Keneman, and J.J. Amodei, *RCA Rev.* 33, 227 (1972).
9. R.A. Bartolini, *Proc. Soc. Photo-Opt. Instrum. Eng.* 123, 2 (1977).
10. W.E. Glenn, *J. Appl. Phys.* 30, 1870 (1959).
11. A. Handojo, *J. Appl. Phys.* 50, 886 (1979).
12. R. Moraw, *Feinwerktech. & Messtech.* 84, 50 (1976).
13. T.L. Credelle and F.W. Spong, *RCA Rev.* 33, 206 (1972).
14. R.A. Gange, E.M. Nagle, and C.C. Steinmetz, U.S. Patent 3 851 948 (1974).
15. W.S. Stewart, R.S. Mezrich, L.S. Cosentino, E.M. Nagle, F.S. Wendt, and R.D. Lohman, *RCA Rev.* 34, 3 (1973).
16. T.C. Lee, N.I. Marzwell, F.M. Schmit, and O.N. Tufte, *Appl. Opt.* 17, 2802 (1978).
17. Available from Rottenkolber Holo-System GmbH, Obing-Allertsham 4, West Germany; see also Ref. 12 above.
18. A.A. Friesem and K. Stadler, *Sci. Electr.* 22, 72 (1976).
19. T.C. Lee, *Appl. Phys. Lett.* 29, 190 (1976).
20. S. Nakadate, N. Magome, T. Honda, and J. Tsujiuchi, in *Optica Hoy y Mañana*, Proc. 11th Congress of the ICO, Madrid 1978, pp. 687-689.
21. D.S. Lo, L.H. Johnson, and R.W. Honebrink, *Proc. Soc. Photo-Opt. Instrum. Eng.* 92, 107 (1976).
22. L.H. Lin and H.L. Beauchamp, *Appl. Opt.* 9, 2088 (1970).
23. J.C. Urbach, in *Holographic Recording Materials* (H.M. Smith, ed.), (Springer-Verlag, Berlin, 1977), pp. 161-207.
24. U. Killat, *J. Appl. Phys.* 46, 5169 (1975).
25. W.S. Colburn and B.J. Chang, *Opt. Eng.* 17, 334 (1978).
26. R.M. Schaffert, *IBM J. Res. Develop.* 15, 75 (1971).
27. W.D. Gill, *J. Appl. Phys.* 43, 5033 (1972).
28. R.F. Bergen, *Photogr. Sci. Eng.* 17, 473 (1973).
29. W.S. Colburn, L.M. Ralston, and J.C. Dwyer, *Appl. Phys. Lett.* 23, 145 (1973).

30. A.W. Birley and D.C.F. Couzens, in *Thermoplastics, Properties and Design* (R.M. Ogorkiewicz, ed.), (Wiley-Interscience, New York, 1974), p. 127.
31. Available from Hercules, Inc., Wilmington, Delaware, U.S.A. and The Hague, The Netherlands.
32. P.F. Gray and M.E. Barnett, *Opt. Commun.* 12, 275 (1974).
33. C.D. Butter and T.C. Lee, *IEEE Trans. Comput.* C-24, 402 (1975).
34. J.C. Bellamy, D.B. Ostrowsky, M. Poindron, and E. Spitz, *Appl. Opt.* 10, 1458 (1971).
35. W.S. Colburn and E.N. Tompkins, *Appl. Opt.* 13, 2934 (1974).
36. H.R. Anderson, Jr., E.A. Bartkus, and J.A. Reynolds, *IBM J. Res. Develop.* 15, 140 (1971).
37. S. Reich, Z. Rav-Noy, and A.A. Friesem, *Appl. Phys. Lett.* 31, 654 (1977).
38. T. Saito, T. Imamura, T. Honda, and J. Tsujiuchi, *J. Optics* 9, 325 (1978).
39. D.S. Lo, L.H. Johnson, and R.W. Honebrink, *Proc. Soc. Photo-Opt. Instrum. Eng.* 123, 32 (1977).
40. J.C. Urbach, *Proc. Soc. Photo-Opt. Instrum. Eng.* 25, 17 (1971).
41. H.F. Budd, *J. Appl. Phys.* 36, 1613 (1965).
42. K.H. Herrmann and D. Krahl, *Optic* 45, 231 (1976).
43. R.J. Doyle and W.E. Glenn, *IEEE Trans. Electron Devices* ED-18, 739 (1971).
44. R.J. Doyle and W.E. Glenn, *Appl. Opt.* 11, 1261 (1972).
45. I. Cindrich, G. Currie, and C. Leonard, *Proc. of the Technical Program, Electro-Optical System Design Conf. 1975*, pp. 301-309.
46. G.D. Currie, I. Cindrich, and C.D. Leonard, *Proc. Soc. Photo-Opt. Instrum. Eng.* 83, 8 (1977).
47. D. Casasent, *Proc. Soc. Photo-Opt. Instrum. Eng.* 128, 56 (1977).
48. G.D. Currie, F.G. Gebhardt, and G.C. Orbits, *Proc. Soc. Photo-Opt. Instrum. Eng.* 128, 217 (1977).
49. J. Gaynor and S. Aftergut, *Photogr. Sci. Eng.* 7, 209 (1963).
50. D.R. Terrell, *Photogr. Sci. Eng.* 21, 66 (1977).
51. R.F. Kopczewski and H.S. Cole, *Appl. Opt. Suppl.* 3 (*Electrophotography*), 156 (1969).
52. S. Aftergut, J.J. Bartfai, and B.C. Wagner, *Appl. Opt. Suppl.* 3 (*Electrophotography*), 161 (1969).
53. A.W. Birley, in *Thermoplastics, Properties and Design* (R.M. Ogorkiewicz, ed.), (Wiley-Interscience, New York, 1974), p. 24.
54. J. Ost and R. Moraw, *Optik* 37, 357 (1973).
55. S. Aftergut, R.F. Kopczewski, and J.F. Burgess, *Photogr. Sci. Eng.* 15, 495 (1971).
56. T.C. Lee, *Appl. Opt.* 13, 888 (1974).
57. T.C. Lee, J.W. Lin, and O.N. Tufte, *Proc. Soc. Photo-Opt. Instrum. Eng.* 123, 74 (1977).
58. U. Killat and D.R. Terrell, *J. Photogr. Sci.* 26, 183 (1978).
59. T. Saito, S. Oshima, T. Honda, and J. Tsujiuchi, *Opt. Commun.* 16, 90 (1976).

60. D.S. Lo, L.H. Johnson, and R.W. Honebrink, *Appl. Opt.* 14, 820 (1975).
61. P.J. Cressman, *J. Appl. Phys.* 34, 2327 (1963).
62. D.L. Matthies, W.C. Johnson, and M.A. Lampert, *J. Appl. Phys.* 46, 2956 (1975).
63. J.T. Bickmore and C.J. Claus, *Photogr. Sci. Eng.* 9, 283 (1965).
64. R.M. Schaffert, *Electrophotography*, rev. ed., (Focal Press, London, 1975), pp. 445-446.
65. N.F. D'Antonio, *Appl. Opt. Suppl.* 3 (*Electrophotography*), 142 (1969).
66. C.F. Gallo, J.E. Germanos, and J.E. Courtney, *Appl. Opt. Suppl.* 3 (*Electrophotography*), 111 (1969).
67. *Guide to Plastics, Property and Specification Charts* (by the ed. of Modern Plastic Encyclopaedia) Mc.Graw-Hill, New York, 1975, p. 241.
68. M. Born and E. Wolf, *Principles of Optics* (Pergamon Press, Oxford, 1970), pp. 615-620.
69. See e.g. F.W. Schmidlin, in *Photoconductivity and Related Phenomena* (J. Mort and D.M. Pai, eds.), (Elsevier, Amsterdam, 1976), pp. 421-478.
70. M. Born and E. Wolf, *Principles of Optics* (Pergamon Press, Oxford, 1970), pp. 7-10.
71. E. Storck and U. Wolff, *Siemens Forsch. - u. Entwickl. - Ber.* 6, 63 (1977).
72. L.H. Johnson, D.S. Lo, and R.W. Honebrink, *Opt. Eng.* 17, 252 (1978).
73. D.A. Seanor, in *Electrical Conduction Properties of Polymers* (A. Rembaum and R.F. Landel, eds.), *J. Polym. Sci. part C* no. 17, 1967, pp. 195-212.
74. O.A. Pickett, Jr., in *Polymer Handbook* (J. Brandrup and E.H. Immergut, eds.), (John Wiley & Sons, New York, 1966), p. VI.80.
75. L.S. Chang, *Photogr. Sci. Eng.* 12, 238 (1968).
76. M.S. Toy, *J. Appl. Polym. Sci.* 9, 1593 (1965).
77. S. Wu, *J. Macromol. Sci. - Revs. Macromol. Chem.* C-10, 1 (1974)
78. D.W. van Krevelen, *Properties of Polymers*, Elsevier, Amsterdam, 1976, pp. 341-345.
79. W.T. Maloney and R.L. Gravel, *Appl. Opt.* 13, 2471 (1974).
80. R. Magnusson and T.K. Gaylord, *J. Opt. Soc. Am.* 68, 806 and 809 (1978).
81. L. Bohn, in *Polymer Handbook* (J. Brandrup and E.H. Immergut, eds.), 2nd ed. (John Wiley & Sons, New York), pp. III.241-III.244; V.A. Matonis, in *Polymer Handbook*, *op.cit.*, pp. VIII.1-VIII.9.
82. C.J. Claus and R.W. Gundlach, in *Xerography and Related Processes* (J.H. Dessauer and H.E. Clark, eds.), (Focal Press, London, 1965), pp. 375-389.
83. D.L. Matthies, W.C. Johnson, and M.A. Lampert, Technical Report no. 25, Dept. of Electrical Engineering, Princeton University, 1973, as cited in Ref. 23.
84. U. Killat and D.R. Terrell, *Opt. Acta* 24, 441 (1977).
85. J.C. Urbach and R.W. Meier, *Appl. Opt.* 8, 2269 (1969).
86. W.T. Cathey, *Optical Information Processing and Holography* (John Wiley & Sons, New York, 1974), pp. 134-140.

87. J. Upatnieks and C.D. Leonard, *Appl. Opt.* 10, 2365 (1971).
88. J.W. Goodman, *Introduction to Fourier Optics* (McGraw-Hill Book, New York, 1968), pp. 58-61.
89. G. Goldmann, *Opt. and Quantum Electron.* 8, 355 (1976).
90. K. Firth, *Marconi Rev.* 41, 61 (1978).
91. L.M. Ralston, M.W. Shareck, and R.G. Zech, *Proc. Soc. Photo-Opt. Instrum. Eng.* 123, 10 (1977).
92. T.C. Lee, *Digest of Technical Papers of Topical Meeting on Optical Storage of Digital Data* (1973), pp. WB4.1-WB4.6.
93. D.S. Lo, L.H. Johnson, and R.W. Honebrink, *J. Opt. Soc. Am.* 66, 1084 (1976).
94. Vu Ngoc Tinh and Shun-ichi Tanaka, *Japan J. Appl. Phys.* 12, 1954 (1973).
95. J.B. DuBow and W.S. Colburn, *J. Opt. Soc. Am.* 63, 1301 (1973).
96. W.S. Colburn and J.B. Dubow, Technical Report AFAL-TR-73-255, Air Force Systems Command (1973), as cited in Ref. 23.
97. R.J. Parker, *Opt. Acta* 25, 787 (1978).
98. R. Moraw, *Laser 75 Opto-Electronics, Conference Proceedings* (IPC Science and Technology Press, Guildford, 1976), pp. 179-180; see also Ref. 12.
99. A. Handojo, Internal Report 4397, Institute of Applied Physics TNO-TH Delft, 1977 (in Dutch).
100. G.G. Goetz, R.K. Mueller, and D.M. Shupe, *IEEE Trans. Electron Devices* ED-20, 1020 (1973).
101. T. Saito, T. Honda, and J. Tsujiuchi, *Opt. Commun.* 23, 44 (1977).
102. J.C. Urbach and R.W. Meier, *Appl. Opt.* 5, 666 (1966).
103. Yu.M. Barabash *et al.*, *Polym. Mech.* 11, 958 (1975).
104. R.W. Gundlach and C.J. Claus, *Photogr. Sci. Eng.* 7, 14 (1963).
105. J.C. Urbach, *Photogr. Sci. Eng.* 10, 287 (1966)
106. See e.g. L.D. Landau and E.M. Lifshitz, *Fluid Mechanics* (Pergamon, London, 1959), pp. 230-237.
107. G.M. Schmid, R.M. Hurd, and E. Snavely Jr., *J. Electrochem. Soc.* 109, 852 (1962).
108. C.F. Hayes, *J. Phys. Chem.* 79, 1689 (1975).
109. N.A. Adam, *The Physics and Chemistry of Surfaces*, 2nd ed. (Oxford Univ. Press, 1938), pp. 343-344.
110. A. Münster, *Classical Thermodynamics* (Wiley-Interscience, New York, 1970), p. 81.
111. P.R. Couchman and W.A. Jesser, *Surf. Sci.* 34, 212 (1973).
112. F. Garcia-Moliner, in *Surface Science, Lectures Presented at an International Course* (IAEA, Vienna, 1975), Vol. I, pp. 3-76.
113. See e.g. H. Scott and W.S. Kaghan, *J. Appl. Phys.* 36, 3399 (1965), see also Ref. 117 below.
114. R. Becker, *Theorie der Elektrizität* (Neubearbeitung des Werkes von M. Abraham), (Teubner Verlag & Druck, Leipzig Berlin, 1933), Band I, pp. 97-101.

115. J.A. Stratton, *Elektromagnetic Theory* (McGraw-Hill, New York, 1941), pp. 147-153.
116. E. Durand, *Elektrostatique et Magnetostatique* (Masson, Paris, 1953), pp. 190-195.
117. S.S. Hakim and J.B. Higham, *Proc. Phys. Soc. London* 80, 190 (1962).
118. Z.A. Weinberg, D.L. Matthies, W.C. Johnson, and M.A. Lampert, *Rev. Sci. Instrum.* 46, 201 (1975).
119. C.F. Eyring, S.S. Mackeown, and R.W. Millikan, *Phys. Rev.* 31, 900 (1928).
120. L.B. Loeb, *Electrical Coronas* (Univ. of Calif. Press, Berkeley, 1965), pp. 10-13.
121. R.W. Klopfenstein and R.K. Wehner, *RCA Rev.* 34, 630 (1973).
122. E. Weber, *Electromagnetic Fields Theory and Applications: Mapping of Fields* (John Wiley & Sons, New York, 1950), pp. 277-413.
123. H.C. Yeh, *J. Appl. Phys.* 46, 4431 (1975).
124. A. Münster, *Classical Thermodynamics* (Wiley-Interscience, New York, 1970), pp. 61-62.
125. R.L. Gravel, *Appl. Opt.* 14, 2054 (1975).
126. J.W. Cahn, *J. Chem. Phys.* 42, 93 (1965).
127. G.W. Anderson and F.U. Luehrs, *J. Appl. Phys.* 39, 1634 (1968).
128. R.C. de Vekay and A.J. Majumdar, *Nature* 225, 172 (1970).
129. J.E. Flannery *et al.*, *Am. Ceram. Soc. Bull.* 54, 1066 (1975).
130. W.G. Schmidt and R.J. Charles, *J. Appl. Phys.* 35, 2552 (1964).
131. L.P. McMaster, in *Copolymers, Polyblends, and Composites* (N.A.J. Platzer, ed.), (Am. Chem. Soc., Washington D.C., 1975), pp. 43-65.
132. J.J. van Aartsen, *Europ. Polymer J.* 6, 919 (1970).
133. *Electrical Safety Guides for Research*, Safety and Fire Protection Bulletin 13, United States Atomic Energy Commission, 1967, p. 43.
134. M. Lodewijk, Interim Report, Institute of Applied Physics TNO-TH Delft, under contract 1978-0-5 (TPD 805.102) of the National Defense Organization, 1978 (in Dutch).
135. E.R.G. Eckert and R.M. Drake, Jr., *Analysis of Heat and Mass Transfer* (McGraw-Hill Kogakusha, Tokyo, 1972), pp. 194-195, and 783.
136. J. Blok and D.G. LeGrand, *J. Appl. Phys.* 40, 288 (1969).
137. L.V. Gregor and L.H. Kaplan, *Thin Solid Films* 2, 95 (1968).
138. G. Oster, *The Science of Moiré Patterns*, (Edmund Scientific, Barrington, N.J., 1969).
139. G. Oster, M. Wasserman, and C. Zwerling, *J. Opt. Soc. Am.* 54, 169 (1964).
140. Agfa-Gevaert 081p graphic film.
141. Available from Edmund Scientific Co., Barrington, N.J., U.S.A.

CONCISE LIST OF SYMBOLS

Latin symbols

A	a considered area at the thermoplastic surface
a	amplitude of the frost deformation
a_r	amplitude of the surface corrugation on a recording
C	factor in the expressions for the potential and the electric field after the exposure
c	factor in the relation between the absorbed intensity and the potential difference across the photoconductor
c_T	temperature coefficient of electric resistor
d	thickness of the photoconductive layer
E_{abs}	exposure energy absorbed by the photoconductive layer
E_x, E_y	electric field in the x and the y direction, respectively
h	thickness of the thermoplastic layer
I_{abs}	intensity absorbed by the photoconductive layer
i	corona charging current; leakage current through the film
J_p	photo-induced current in the photoconductive layer
k	$2\pi/\lambda$
k_x, k_y	$2\pi/\lambda_x, 2\pi/\lambda_y$
l_1, l_2	index number of the lines in the patterns to be overlaid
l_M	index number of the lines in the Moiré pattern
m_I	modulation in the absorbed intensity
m_σ	modulation in the charge density σ_t at the thermoplastic-photoconductive interface
n_1	refractive index of the thermoplastic material
p	pressure in the thermoplastic material
p_1, p_2	point groups, used as the object in the study of the pass band

Q	charge at the thermoplastic surface
R	electric resistor
S/N	signal-to-noise ratio in the readout of a recording
s	thickness of the substrate
s_1, s_2	line spacing in the patterns to be overlaid
s_M	line spacing in the Moiré pattern
t	time
t_d	development time
t_p	preheating time in the method with two heating stages
U_o, U_r	wave function of the object and the reference wave, respectively
U_{th}	threshold voltage for the frost deformation
u	surface corrugation of the thermoplastic layer
V	electric voltage
x, y, z	Cartesian coordinates

Greek symbols

α	absorption coefficient of the photoconductive layer
Γ	ratio between the relative change of the Moiré line spacing and the relative deviation of the line spacing in one of the original patterns
γ	surface tension of the thermoplastic material
ϵ_0	permittivity of vacuum
ϵ_1	permittivity of materials composing the film
ϵ_{r1}	relative permittivity ($=\epsilon_1/\epsilon_0$)
η	diffraction efficiency
θ	Celsius temperature
θ_d	development temperature
θ_g	glass transition temperature of the thermoplastic material
θ'_o, θ'_r	angle between the film normal and the propagation direction in air of the object and the reference wave, respectively

θ_o, θ_r	angle between the film normal and the propagation direction within the film of the object and the reference wave, respectively
θ_s	scattering angle
κ	$2\pi/\Lambda_1$
λ	spatial wavelength of the frost deformation
λ_x, λ_y	spatial wavelength of the light and the potential distributions in a recording, in the x and y direction, respectively
Λ_0	light wavelength in vacuum
Λ_1	light wavelength in the photoconductive layer
σ	surface charge density at the thermoplastic surface
σ_t	surface charge density at the thermoplastic-photoconductive interface
ϕ	electric potential
ϕ_e	voltage at the corona electrodes
ϕ_s	potential at the surface of the thermoplastic layer
$\Delta\phi_{pc}$	potential difference across the photoconductive layer
ϕ_o, ϕ_r	phase of the object and the reference wave, respectively
ψ	angle between the lines of the patterns to be overlaid

SUMMARY

Photothermoplastic film is one of the new optical recording materials with which in situ development and readout can be realized within a short time. First, an electric field must be produced within the film by a charging stage. At exposure, the intensity distribution to be recorded modifies the electric field. During the development, a thermoplastic layer in the film is softened such that the field can deform this layer.

The thickness variations thus produced cause phase variations in the light beam that propagates through the film during readout. In holography, this phase modulation leads to a higher diffraction efficiency than an amplitude modulation.

The performance of this film is dependent of various factors, such as the thickness of the thermoplastic layer, the configuration of the corona charging device and the high voltage applied to it, and the softening temperature of the thermoplastic material.

Based upon the results of various other authors and upon our own theoretical and experimental considerations, we have have studied those influential factors. On the experimental side, we have measured among others the diffraction efficiency, the signal-to-noise ratio and the linearity of our film response as a function of the recording parameters.

We have considered the photo-electric transfer within the photoconductive layer and proposed a model based upon an electric lumped circuit. From this model we can conclude that the photo-electric transfer is only linear if the exposure energy is very low, which has been confirmed experimentally.

Using that model, we have derived the electric potential distribution within the film. From this distribution it appears that a film having a thick substrate between the photoconductive and the conductive layer (like our film) is not suitable for the recording methods in which during or after the exposure the thermoplastic surface must be equipotential. These methods (e.g. the sequential and the simultaneous methods) would produce a high diffraction efficiency using other film types.

Another parameter that influences the film performance is the thickness of the thermoplastic layer. In registrating light distributions, a photothermoplastic film has a bandpass characteristic in the spatial frequency domain. The spatial wavelength corresponding to the optimal frequency is proportional to

the thickness of the thermoplastic layer.

As part of the efforts to explain this wavelength-thickness relation, we have suggested a quasi-static theory which appears to approach the experimental results better than the dynamic theories from other authors do. All these theories are formulated for the special case of frost deformation and may not be directly applied to calculate the characteristics of a thermoplastic recording. Apart from explaining the frost phenomenon, the theories should be regarded as a base that can be developed further to form a comprehensive theory of the thermoplastic film.

To enable us to work with the available film, we have built a special camera system. This system consists of a camera (comprising among others the mechanism for the film transport and the "heat plate" upon which the film sticks during the recording process), a shutter, a high-voltage supply and an electronic control unit. In the electronic control, apart from various parts for directing the recording process, we have built a temperature control for regulating the development temperature.

This temperature control is based upon the change in the electrical resistance of the conductive layer coated on the heat plate. To this end, we had to measure the resistance-temperature relation of several kinds of layers (In_2O_3 and Au) first.

The temperature control turned out to work satisfactorily; after the adjustment to obtain the optimal development temperature, about 25 holograms can be recorded with the same adjusted value without showing a significant quality change.

One of the series of experiments, performed with the camera system, concerns the development of a recording method with two heating stages; the first is a preheating before the charging stage, the second is the usual development stage. This method leads to a higher diffraction efficiency than the charge-expose-develop method.

To measure the deformation amplitude and the spatial wavelength of the frost bubbles, obtained on our film, we have used an interference-microscope set-up. The frost sizes on the obtained photographs have been measured with a technique based upon Moiré patterns. The measurement results are in a reasonable agreement with the prediction from the equipotential model in our frost theory.

We have studied the bandpass characteristic of our film on the basis of the appearance of ghost images from a nonlinear recording.

Finally, several techniques have been proposed to record an object, which is such that the produced spatial frequencies exceed the pass band of the film. The experimental results suggest the practical usefulness of these techniques.

SAMENVATTING

Fotothermoplastische film is een van de nieuwe optische registratiematerialen waarmee na de opname, ter plaatse en binnen een korte tijd ontwikkeling en weergave kunnen worden gerealiseerd. Bij opname wordt de sterkte van een aangebracht elektrisch veld binnen het materiaal gekoppeld aan de intensiteit van de vast te leggen lichtverdeling; tijdens het ontwikkelen wordt een thermoplastische laag in de film week gemaakt, zodat het genoemde veld deze laag kan deformeren.

De hierdoor ontstane dikte-variatie veroorzaakt bij weergave fase veranderingen in de er door vallende licht-bundel. Deze fase beïnvloeding levert bij holografie een hoger lichtrendement op dan een amplitude beïnvloeding zou doen.

De werking van deze film wordt beïnvloed door verschillende factoren, zoals de dikte van de thermoplastische laag, de configuratie van het corona apparaat en de oplaadspanning waarmee een elektrisch veld binnen de film wordt aangebracht, en de temperatuur voor het verweken van het thermoplastische materiaal.

Wij hebben deze factoren bestudeerd op grond van resultaten van verschillende auteurs en op grond van onze theoretische en experimentele beschouwingen. Aan de experimentele zijde zijn onder andere het buigingsrendement, de signaal-ruis verhouding en de lineairiteit van onze film als functie van de opname parameters gemeten.

Wij hebben de foto-elektrische overdracht binnen de fotogeleidende laag bestudeerd en hiervoor een model, gebaseerd op een elektrische schakeling, voorgesteld. Uit dit model kunnen wij concluderen dat het foto-elektrische proces slechts lineair is voor een zeer lage belichtingsenergie, hetgeen experimenteel bevestigd is.

Gebruik makend van dit model hebben wij de elektrische potentiaal verdeling binnen de film afgeleid. Het blijkt uit deze potentiaal verdeling dat een film met een dikke drager tussen de fotogeleider en de geleidende laag, zoals het geval is bij onze film, niet geschikt is voor opname methoden waarbij tijdens of na de belichting het thermoplastische oppervlak equipotentiaal moet zijn. Deze methoden (bijvoorbeeld de "sequential" en de "simultaneous" methoden) zouden voor andere soorten van films een hoog buigingsrendement kunnen opleveren.

Een andere parameter die van invloed is op de filmwerking is de dikte van de thermoplastische laag. Bij het vastleggen van lichtverdelingen, heeft de film een handdoorlatend karakter ten aanzien van de ruimtelijke frequenties. De ruimtelijke golflengte behorende bij de optimale frequentie is evenredig met de thermoplastische laagdikte.

In het kader van de pogingen om deze golflengte-dikte betrekking te verklaren, hebben wij een quasi-statische theorie voorgesteld, die de experimentele resultaten beter blijkt weer te geven dan de dynamische theorieën van andere auteurs. Al deze theorieën zijn geformuleerd voor het speciale geval van "frost" deformatie en mogen niet zonder meer worden gebruikt om het karakteristiek van een thermoplastische opname te berekenen. Naast het verklaren van het "frost" verschijnsel, dienen ze als een basis die verder ontwikkeld kan worden tot een algemene theorie over de werking van een thermoplastische film.

Om te kunnen werken met de ons beschikbare film, is een camera systeem opgebouwd. Dit systeem bestaat uit een camera (met onder andere het mechanisme voor het film transport en de "warmte plaat" waarop de film tijdens het opname proces vastplakt), een sluitser, een hoogspanningsvoeding en stuuerelektronica. In de stuuerelektronica hebben wij, naast verschillende secties voor het regelen van het opname proces, een temperatuurregeling aangebracht voor het beheersen van de ontwikkeltemperatuur.

Deze temperatuurregeling werkt op grond van de veranderingen in de elektrische weerstand van de geleidende laag op de warmteplaat. Hiervoor moesten wij eerst de weerstand-temperatuur relatie van verschillende soorten van lagen (In_2O_3 en Au) meten.

De temperatuurregeling bleek bevredigend te werken; na het optimale instellen van de ontwikkeltemperatuur, kunnen ongeveer 25 hologrammen worden opgenomen met dezelfde instelling, zonder dat een significante kwaliteitsverandering valt te bespeuren.

Een van de reeksen van experimenten, uitgevoerd met het camera systeem, behelst het ontwikkelen van een opname methode met opwarming in twee stappen; de eerste is een voorverwarming vóór de oplaadstap, de tweede die van het gewone ontwikkel proces. Deze methode levert een hoger buigingsrendement op dan de oplaad-belichting-ontwikkel methode.

Voor het meten van de amplitude en de golflengte van de "frost" bobbels, verkregen op onze film, hebben wij een interferentie-microscoop opstelling gebruikt. De "frost" afmetingen op de hieruit verkregen foto's zijn gemeten met een techniek gebaseerd op Moiré patronen. De meetresultaten zijn in redelijke overeenkomst met de voorspellingen uit het equipotentiaal-model in

onze "frost" theorie.

Wij hebben de banddoorlatende karakteristiek van onze film bestudeerd aan de hand van het optreden van spookbeelden bij een niet-lineaire opname.

Tenslotte zijn enkele technieken voorgesteld voor het opnemen van een object, dat zodanig is dat de geproduceerde ruimtelijke frequenties de doorlaat-band van de film overschrijden. Experimentele resultaten wijzen op de praktische bruikbaarheid ervan.

LEVENSBERICHT

De samensteller van dit proefschrift werd op 5 september 1946 te Malang, Indonesië, geboren.

De studie in de Technische Natuurkunde (Fisika Teknik) ving hij in augustus 1964 aan het Institut Teknologi Bandung aan. In oktober 1970 behaalde hij aldaar het ingenieursdiploma in de afstudeerrichting instrumentatie.

Door tussenkomst van onder andere het Bandoengse Hogeschool Fonds kreeg hij kans om meer kennis en ervaring te verwerven in Nederland voor zijn toekomstige baan als docent aan het Institut Teknologi. Vlak na zijn aankomst in Nederland begon hij in januari 1972 te studeren aan de afdeling der Technische Natuurkunde te Delft.

Zijn studie werd in 1973 zes maanden onderbroken door een ernstige ziekte.

Gedurende en na een herstel en controle periode kon hij zijn kandidaats en afstudeerwerk verrichten in de vakgroep Optica onder leiding van Prof. H.J. Frankena. Het ingenieurexamen legde hij in mei 1975 af met het afstudeeronderwerp: het interferometrisch testen van sferische en asferische oppervlakken en lenzen door middel van computerhologrammen.

Tussen 1 april 1976 en 1 oktober 1976 en tussen 15 juni 1977 en 15 december 1977 werkte hij bij de Technisch Fysische Dienst te Delft in de hoofd-afdeling Optiek onder leiding van dr.ir. W. Werner en ir. H.J. Raterink. Fotothermoplastisch registratie materiaal was het onderwerp van het onderzoek in die periode dat tevens de belangrijke basis vormde voor dit proefschrift.

Vanaf 15 december 1977 ontving hij van het Nederlandse Ministerie van Onderwijs en Wetenschappen een studiebeurs die beschikbaar was in het kader van het cultureel verdrag tussen Nederland en Indonesië. Met deze beurs zette hij het onderzoek voort in de vakgroep Optica van de Technische Hogeschool, waar het werk in augustus 1979 afgerond werd met het samenstellen van dit proefschrift.

DANKBETUIGING

De schrijver wil zijn erkenning betuigen aan de directie van de Technisch Physische Dienst TNO-TH Delft voor de gelegenheid die hij heeft gekregen om een belangrijk gedeelte van dit onderzoek te verrichten.

Voor de financiële steun van het Ministerie van Onderwijs en Wetenschappen (Centrale Directie Internationale Betrekkingen), die het voortzetten van het onderzoek en het uiteindelijke samenstellen van dit proefschrift mogelijk heeft gemaakt, is de schrijver zeer dankbaar.

Penulis menyampaikan terima kasih kepada Bagian Pendidikan dan Kebudayaan, KBRI Den Haag atas bantuan yang diberikan dalam mendapatkan beasiswa, dan kepada staf Fisika Teknik serta pimpinan Institut Teknologi Bandung atas keleluasaan untuk menyelesaikan penelitian ini.

Ten slotte wil de schrijver gaarne zijn dank uitspreken aan alle anderen die hebben bijgedragen aan het tot stand komen van dit proefschrift.

STELLINGEN

behorende bij het proefschrift van

A. Handojo

12 december 1979

-1-

De ladingsverdeling in het vlak tussen de thermoplastische en de fotogeleidende lagen, die als gevolg van de belichting van een homogeen opgeladen fotothermo-plastische film door een sinusvormige intensiteitsverdeling is ontstaan, is slechts sinusvormig indien de ladingsdichtheid op het thermoplastische oppervlak of de belichtingsenergie een zeer lage waarde heeft.

Dit proefschrift, vergelijkingen (3.38) en (3.40).

-2-

"Frost" theorieën mogen niet zonder meer worden gebruikt om de karakteristieken van een opname op fotothermoplastische film te berekenen.

Dit proefschrift, paragraaf III.7.

W.C. Stewart *et al.*, *RCA Rev.* 34, 3 (1973).

P.F. Gray en M.E. Barnett, *Opt. Commun.* 12, 275 (1974).

-3-

Indien het verschijnsel fasescheiding in een thermoplastische film optreedt, dient het gezien te worden als één van de oorzaken, in plaats van als het enige mechanisme, van de "frost" deformatie.

Dit proefschrift, paragraaf IV.5.

S. Reich *et al.*, *Appl. Phys. Lett.* 31, 654 (1977).

A.A. Friesem, correspondentie.

-4-

De ruimtelijke golflengte van de "frost" deformatie, berekend op grond van de groei-neigingen van de beginnende oppervlakte-uitwijkingen, behoeft niet gelijk te zijn aan de waarde aan het einde van het deformatie proces.

A. Handojo, *J. Appl. Phys.* 50, 886 (1979).

H.F. Budd, *J. Appl. Phys.* 36, 1613 (1965).

U. Killat, *J. Appl. Phys.* 46, 5169 (1975).

-5-

Het afleiden van de relatie tussen enerzijds de ladingsverdeling op het grensvlak van de thermoplastische en de fotogeleidende lagen, en anderzijds de intensiteit van de op de film invallende lichtverdeling, zonder dat men rekening houdt met de absorptie van de fotogeleider, is van twijfelachtige waarde.

T.C. Lee, *Appl. Phys. Lett.* 29, 190 (1976).

-6-

Technologie is niet uitsluitend een zaak van technische vakkennis. Bij technologisch gerichte ontwikkelingssamenwerkings programma's worden doorgaans personen uitgewisseld om kennis over te dragen of te verwerven. Het verdient aanbeveling om bij het opstellen van zulke programma's rekening te houden met de richtlijn, dat men pas na een verblijfsperiode van ongeveer twee jaar verschillende aspecten van de plaatselijke samenleving in voldoende mate begint te begrijpen.

-7-

De veelvuldige berichten in de nederlandse pers over de ellende in de landen van de derde wereld zoals armoede, corruptie, wanbeheer en dergelijke, hoe waar zij ook mogen zijn, leveren slechts een geringe bijdrage tot het vormen van een volledig beeld over de werkelijke levensatmosfeer in die landen.

-8-

"Weerstations", die uitgevoerd zijn als een vitrine aan de buitenmuur van bepaalde winkels (en waarin vaak tevens reclame objecten te vinden zijn), kunnen een betere benadering van de luchttemperatuur weergeven als deze stations voldoende afgeschermd worden van de directe zonne straling.

-9-

Het typen van een manuscript met veel formules zou aanzienlijk versneld kunnen worden indien de typemachine voorzien is van een schrijfbol-magazijn met een mechanisme waarmee de te gebruiken bol direct (bijvoorbeeld door het instellen van een knop) verwisseld kan worden.

-10-

De storende "sneeuw" bij een (zeer) slechte televisie ontvangst kan goeddeels onzichtbaar worden gemaakt door te kijken met half toegeknepen oogleden.

-11-

Het aanduiden van bepaalde afbeeldingen in optische systemen als "spook-beelden" kan worden beschouwd als een bijdrage van de mystieke wereld tot de exacte wetenschappen.